



Department of Mathematics and Physics
XXXIII Cycle of the Doctoral School in Physics

**Low energy ion collisions as a tool for unveiling
the HOPG anion intercalation mechanism**

Stefania De Rosa

Supervisors
Dott. P. Branchini
Dott. L. Tortora

PhD Course Coordinator
Prof. G. Degrassi

Contents

Abstract	v
Introduction	vii
1 Anion intercalation in HOPG: theory and applications	3
1 Carbon and graphite materials	3
1.1 Highly Oriented Pyrolytic Graphite (HOPG)	5
2 Graphite Intercalation Compounds	8
3 HOPG intercalation in aqueous acid solutions	8
3.1 Theoretical models	9
2 Low energy ion beam analysis	13
1 Secondary Ion Mass Spectrometry: general principles	13
2 Ion-solid interaction	15
2.1 Scattering cross section	16
2.2 Processes in target	18
2.3 Emission phenomena	23
2.4 Secondary ion formation	30
3 Secondary ions detection and analysis	32
3.1 Time-of-flight (ToF) mass analysis	33
4 Analysis beams of ToF-SIMS	37
4.1 Liquid metal ion sources (LMIS)	37
4.2 Surface ionisation sources	39
4.3 Other ion sources	39
5 Instrumental setup	40
5.1 Analyser	41
5.2 Primary ion beam column	42
5.3 Dual-source column	43
5.4 Electron flood gun	45
6 ToF-SIMS analysis modes	45
6.1 Static SIMS	46
6.2 Dynamic SIMS: depth profiling	49
3 Exploring the effects of different projectiles with different energies	55
1 Comparison of Cesium (Cs^+) and Argon cluster (Ar_n^+) ion beams for HOPG sputtering	56
1.1 Experimental setup	56
1.2 Topography modifications induced by ion bombardment	56
1.3 Sputter yield dependence on projectile properties	58

4	Anion intercalation in HOPG: surface phenomena	61
1	Sample preparation	61
2	Surface analysis techniques	63
3	Results and discussion	64
3.1	HOPG intercalation with perchloric and sulfuric acids	64
3.2	High-resolution XPS results	65
3.3	Static ToF-SIMS results	67
5	Anion intercalation inside the HOPG buried layers	73
1	Samples preparation	73
2	ToF-SIMS/in-situ AFM setup	74
2.1	Craters depth evaluation	74
3	Results and discussion	74
3.1	General remarks of the intercalation process	74
3.2	Chemical and morphological analysis of the “surface” and buried graphite layers	75
3.3	The problem of the graphite crystal defects	81
6	Low energy ion beam analysis applied to other low dimensional materials	85
1	Cysteine-modified self-assembling peptides on gold	85
1.1	Results	88
2	Reactive dissolution of organic nanocrystals: porphyrin thin films deposited on HOPG	94
2.1	Results	96
	Conclusions	101
	Acknowledgments	103
	Publication list	105
	Bibliography	107

Abstract

Graphitic electrodes in ion batteries and graphite electrochemical exfoliation for graphene production are two examples of technological applications of the anion intercalation in stratified crystal structures upon immersion in acid solutions. To the detriment of the graphite parent-crystal, the production of unexpected graphite intercalation compounds (GICs) is a side effect related to the anion intercalation mechanism.

In this thesis, Highly Oriented Pyrolytic Graphite (HOPG) samples treated with electrolyte solutions of 2 M HClO_4 and 1 M H_2SO_4 are studied in order to identify elemental and molecular species involved in the intercalation processes. Results from Time-of-Flight Secondary Ion Mass Spectrometry (ToF-SIMS) are described and discussed. In both HOPG samples, the surface distribution of perchlorate and hydrogen sulfate anions gives direct evidence that the anion intercalation happens via surface defects among HOPG crystallites. These results pave the way for a complex intercalation process where more than one molecular species could be responsible for carbon detriment. By combining ToF-SIMS and in-situ SPM, a picture of the chemical species involved in the intercalation reaction within the buried graphite layers is provided. The depth concentration profiles of the ion signals along the electrode crystal show a two-step diffusion process: after a first stage, where solvated anions are mostly located within the first tens of nanometers of graphite, anions diffuse inside the bulk according to the molecular steric hindrance.

Introduction

Ion batteries development and electrochemical exfoliation for thin film materials production are two meaningful examples of technological fields of study where anion intercalation into stratified crystal structures plays a fundamental role. Electrochemistry has been linked to graphite since the early days of its research application because of its good electrical and thermal conductivity, corrosion resistance, low thermal expansion, low elasticity, and high purity. The more traditional form of graphite implemented as electrode is Highly Oriented Pyrolytic Graphite (HOPG), the stratified crystal prototype. Nowadays, HOPG has also focused an additional interest due to its layered structure, which can be thought in terms of honeycomb graphene sheets stacked parallel to each other. The materials research community is currently involved in research focusing on the characterization and real-world applications of ultra-thin carbon films, the thinnest of which is graphene. 2D electronics requires flat, flexible, and resistant devices and graphene has proved to be the proper material for these applications. In this respect, a huge amount of high-quality graphene foils are required for the commercialisation of graphene-based electronic devices. In view of efficient industrial implementation, we are obliged to combine a quantity and quality enhancement of graphene production with a reduction in the cost of production. Graphite exfoliation into one-atom-thin sheets can be achieved by different chemical routes in the liquid phase. The more controllable and tunable approach takes advantage of electrochemistry. Applying proper electrochemical (EC) potentials, graphite is delaminated by ion intercalation within its stacked structure. Historically, perchloric (HClO_4) and sulfuric (H_2SO_4) acids represent suitable electrolytes in mild aqueous solutions for graphitic electrodes treatment. Solvated ClO_4^- and SO_4H^- anions percolate between the HOPG layers. Consequently, the layer-layer Van der Waals interaction is reduced and a gentle sonication can dissolve part of the original HOPG crystal inside a liquid suspension of graphene sheets. Despite the good results reported in the literature, the graphene flakes radii sizes are widely dispersed over a range from tens of nanometers up to 1 micrometer. In addition, structural damages, defects, water, and electrolyte contaminations on exfoliation products are frequently reported. Most of the works follow a trial-and-error method but there is still an unjustified lack of knowledge regarding the molecular mechanisms involved in anion intercalation of HOPG parent-crystal. A clarification of the HOPG delamination steps can help in further optimization of the production protocol. Among all the side effects of anion percolation, the HOPG evolution in the so-called Graphite Intercalation Compound (GIC) is the more interesting. GIC shows different chemical and physical properties with respect to the pristine sample and is considered a new crystal having intercalated ions between ordered arrays of one or more graphite layers. The most relevant morphological change on the crystal surface after the graphite intercalation is the formation of blisters, generally interpreted as a consequence of the evolution of gaseous molecular species during the first stages of the EC process. The morphological changes occurring on HOPG basal plane have been extensively studied through microscopic techniques, like electrochemical-atomic force

microscopy (EC-AFM) or Raman spectroscopy. More recently, it has been possible to monitor the blistering appearance by combining Electrochemical-Scanning Tunneling Microscopy (EC-STM) and Cyclic Voltammetry (CV). All results from these works demonstrate an interdependence between the HOPG surface swelling and the reaching of the oxygen evolution potential. Nevertheless, highly sensitive analysis of the chemical species involved in the intercalation process together with an investigation of their penetration length inside the HOPG crystal is still missing.

This PhD thesis aims to fill this knowledge gap. To this purpose, low energy ion beam bombardment, combined with other surface-sensitive techniques, is exploited. Results from Time-of-Flight Secondary Ion Mass Spectrometry (ToF-SIMS) offer an excellent combination of extremely high surface sensitivity and lateral resolution allowing imaging during the identification of elemental and molecular species on the sample surface. In addition, the in-depth chemical and molecular composition is provided with resolution in the nanometer range. The HOPG samples, treated with electrolyte solutions of HClO_4 and H_2SO_4 are studied in order to identify elemental and molecular species involved in the intercalation processes and, at the same time, find local surface defects through which solvated ions easily reach the HOPG bulk. The chemical and structural products of the anion intercalation are investigated also in the sub-surface regions of the HOPG crystals with dual beam ToF-SIMS depth profiling experiments at very low energy.

The thesis structure is organised as follows. In **Chapter 1**, the structure of HOPG crystal and its chemical and physical properties are described. The major technological applications of the anion intercalation in graphite crystals are then outlined. The principal theoretical models at the base of GICs formation during the HOPG ion intercalation are also summarised. In **Chapter 2**, low energy ion beam analysis technique is described in detail, starting from the theoretical principles at the base of secondary ion formation through ion collisions to the experimental setup used in this work. A preliminary approach in applying low energy ion beam analysis to HOPG samples is presented in **Chapter 3**. Here, the effects of cesium Cs^+ and argon cluster Ar_n^+ ion projectiles at different energies on HOPG target are compared. The study of the two different acid-treated HOPG samples is then divided into two parts, first with an analysis of the sample surface phenomena in **Chapter 4**, and then investigating the EC treatment effects in sub-surface regions in **Chapter 5**. Finally, in **Chapter 6**, two further works carried out during my PhD are briefly shown as examples of the high versatility of ToF-SIMS analysis approach.

Chapter 1

Anion intercalation in HOPG: theory and applications

Carbon-based electrodes have been, and continue to be, used largely in electrochemistry, for a wide range of applications. Development of the ion batteries, in particular, the improvement of the transport properties of their constituent materials, and graphene industrial production, are two of the most significant examples of technological areas where electrochemical ion intercalation into stratified electrode structures plays a crucial role. The stratified crystals prototype, namely Highly Oriented Pyrolytic Graphite (HOPG), consists of honeycomb graphene layers stacked parallel to each other. HOPG is a material that has been studied intermittently for several decades, but which is of enduring interest, particularly as a comparison to other types of carbon electrodes.

1 Carbon and graphite materials

Carbon stands, in its elementary form, in a wide range of possible structures and morphology, from well-defined three-dimensional (3D) ordered graphite and its amorphous configuration, to its low-dimensional allotropes, such as carbon nanotubes and graphene. The properties of carbon-based material, i.e. electrical and thermal conductivity, mechanical stability, chemical robustness, low density, and structural diversity have long been well known, however, at the moment, it seems that carbon has not yet finished surprising the scientific community. In addition, the attractive properties of carbon can be easily manipulated by several chemical and physical procedures, making it extremely versatile too. Carbon-based materials, either by themselves or as a support to other active non-carbon materials, are being employed for various energy storage and catalytic conversion applications (e.g. lithium-ion batteries, fuel cells, and supercapacitors [1,2]).

Among the different bulk forms of carbon material, the most common is graphite. It has been used as active electrode in many works for a wide variety of applications, ranging from its use as anode in electrochemical energy storage devices [3], as model system for metal nucleation growth [4], or its employment for the creation of nanoscale interfaces, exploited in sensing and biological fields [5].

Graphite crystallizes in a layer-structured lattice, in which the carbon atoms form regular sheets of linked hexagons, which are displaced relative to one another. The carbon planes of graphite can be stacked along the *c*-axis¹ in an ABA (hexagonal, more diffuse in nature) or ABC (rhombohedral, unstable and less common) arrangement, as shown

¹A vertically oriented crystal axis, usually the principal axis; the unique symmetry axis in tetragonal and hexagonal crystals.

in Figure 1.1(a,b). The lateral shift, from layer A to layer B is 0.25 nm [6].

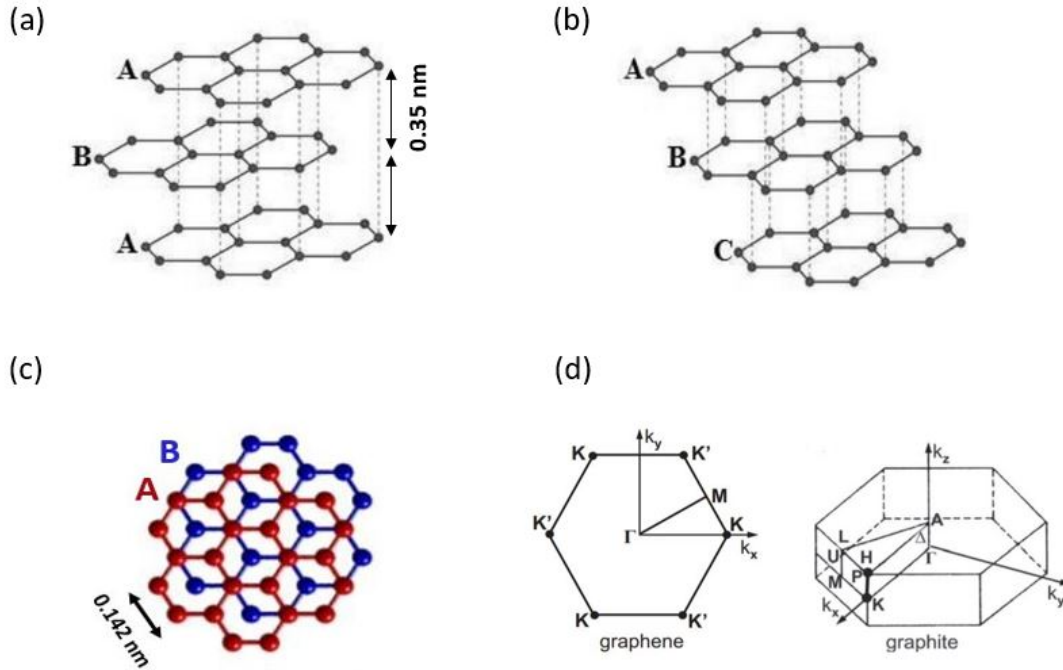


Figure 1.1: Lateral view of (a) hexagonal and (b) rhombohedral graphite crystal, with the ABA and ABC stacking, respectively. A, B and C are hexagonal single (graphene) planes. (c) Top view and (d) unit cell in the reciprocal space (Brillouin zone) of the hexagonal graphite and graphene crystal structure: A and B are in plane carbon atoms. The high-symmetry points of the Brillouin zone are shown.

In 2004, a single monoatomic layer of graphite, called graphene, was isolated for the first time [7]. Graphene is a one-atom-thick planar sheet of sp^2 -bonded carbon atoms, arranged in a two-dimensional (2D) hexagonal crystal lattice, with two crystallographically equivalent atoms in the unit cell (A and B in Figure 1.1c). In the graphene sheet plane, each carbon atom, placed on a vertex of the hexagon, is bonded to its three first-neighbors by a strong in-plane covalent σ -bond from sp^2 -hybridized orbitals. At the equilibrium, the C-C σ -bond (distance) is 0.142 nm [8]. This bond results in the stable planar structure and the exceptional mechanical and thermal properties of the *free-standing* graphene. The fourth valence electron of carbon, in the $2p_z$ orbital orthogonal to the graphene plane, does not participate in the σ -bond, but forms a weak (Van der Waals) π -bond, by overlapping with other $2p_z$ orbitals. Such a π -type electronic band is half full. This means that graphene is a zero-gap *semimetal* because bonding (π) and anti-bonding (π^*) bands intersect at K and K' points (often called Dirac points), which are the vertices of the hexagon and two of the high-symmetry points of the Brillouin zone (unit cell of the crystal in the reciprocal space), shown in Figure 1.1(d). The linear dispersion of the graphene π -bands in the proximity of the K and K' points, i.e. the presence of low-energy and zero mass electronic excitations (Dirac fermions), is responsible for the peculiar electronic properties of graphene [9]. The extraordinary physical properties of graphene [10] and its ease (on small scale, at least) of fabrication through graphite exfoliation techniques [11], immediately and hugely attracted the interest of the scientific community. Ergo, starting from the Nobel Prize in Physics assignment to A. Geim and K. Novoselov in 2010, it has become conventional to consider graphite as a "natural" set of graphene sheets, stacked to form the bulk crystal.

For graphene production, graphite can be exfoliated in liquid environments, exploiting ultrasounds to extract individual layers. The liquid-phase exfoliation process generally involves three steps: 1) dispersion of graphite in a solvent; 2) exfoliation; 3) “purification”. This latter step is necessary to separate exfoliated from non-exfoliated flakes and is usually carried out via ultracentrifugation. Liquid-phase exfoliation is cheap and easily scalable and does not require expensive growth substrates. Furthermore, it is an ideal means to produce inks, thin films, and composites. The resulting material can be deposited on different substrates (rigid and flexible) [11].

The layered graphite structure produces a significant anisotropy in its physical and chemical properties. For example, there is a substantial difference in strengths between planes and within the plane. Similarly, the conductivity, at room temperature, can vary enormously along and perpendicular to the plane [12]. Furthermore, the type of stacking has important implications for graphite electronic structure [13], albeit the stacking distance between two consecutive graphene layers is 0.335 nm [6], in both ABA and ABC dispositions.

1.1 Highly Oriented Pyrolytic Graphite (HOPG)

Graphite is available in nature, but it can be artificially produced by a variety of methods [14]. Pyrolytic graphite, an example of artificial graphite, is produced by thermal decomposition of carbonaceous gases in petroleum coke, usually methane, at temperatures above 1200°C. To benefit the most from the properties of the hexagonal layered structure, the Highly Oriented Pyrolytic Graphite (HOPG) is exploited for scientific and industrial purposes. HOPG originates from the pyrolytic carbon, when it is heated at high temperatures and, at the same time, under high pressure [15]. The result is a polycrystalline material, with multiple graphene sheets stacked on top of each other, and held together by weak attractive intermolecular forces, to make a 3D structure. As a layered polycrystal, HOPG is composed of graphene monocrystals and graphite grains (or flakes) of different sizes [16]. The preferred crystallographic orientation of the c-axes (perpendicular to graphene layers) can differ from a monocrystal to another one. The degree of reciprocal misorientation of stacked graphene layers, obtained by X-ray crystallography [17], is quantified by the *mosaic spread* parameter, i.e. an angular value that comes from the possible broadening of the (002) diffraction peak with Cu-K α radiation [17]. The lower the mosaic spread, the higher the quality of HOPG. According to this, HOPG quality is classified with a grade terminology that depends on the supplier: the highest quality is denominated ZYA, with a mosaic spread of $0.4 \pm 0.1^\circ$. HOPG grades of lower quality are ZYB, ZYD, and ZYH, with mosaic spreads of $0.8 \pm 0.2^\circ$, $1.2 \pm 0.2^\circ$ and $3.5 \pm 1.5^\circ$, respectively [18]. HOPG crystallite dimensions are usually determined by X-ray diffraction and Raman spectroscopy [19], from which the crystallite dimensions in-plane and perpendicular to the graphene planes can be defined. Polycrystalline graphite can have crystallites up to 100 nm, with HOPG exhibiting the largest values, beyond 1 μm . The layered structure of HOPG, regardless of the crystal grade, presents a significant mechanical anisotropy, which results in a simple exfoliation of its basal planes [20]. As a consequence, HOPG is particularly suitable for providing wide areas of atomically flat surfaces by simple exfoliation. The use of scotch tape to peel off the top crystal HOPG layers, achieving a fresh and atomically flat surface, is the most common procedure [21], but alternative mechanical cleavage procedures are also available [22, 23]. The out-of-plane π -type orbitals weakly interact with the environment, maintaining the graphite surface almost clean for several minutes after its delamination. For this reason, and also for its simple prepa-

ration, HOPG is suitable for atomic-resolution scanning probe microscopy techniques. HOPG surfaces have been widely characterised at the atomic level with Scanning Tunneling Microscopy (STM) [24] and Atomic Force Microscopy (AFM) [25]. Indeed, HOPG and its monoatomic steps are used as standard material to calibrate such equipment [26].

Atomic resolution images of the HOPG basal plane often highlight technique-dependent properties that provide precise information on the graphite local structure. As to mention an example, in STM imaging, basal plane surfaces show a triangular lattice instead of the honeycomb structure that might be expected for the hexagonal crystal lattice of graphite (Figure 1.1). This is because STM images creation is based on the local density of electronic states (LDOS) at the Fermi level, rather than in the atomic arrangement. With AB stacking, the A atoms in the top layer are stacked above B atoms in the second layer, while B atoms in the top layer are above the hollow sites of the carbon hexagons of the second layer. This asymmetry in the interlayer coupling leads to a strong asymmetry in the LDOS at the Fermi level and in the STM image B atoms on the graphite surface appear more prominent than the A atoms [27]. This behavior is also observed in multi-layer graphene flakes, while for monolayer graphene, symmetrical honeycomb structure is seen in the STM image [27] (see Figure 1.2).

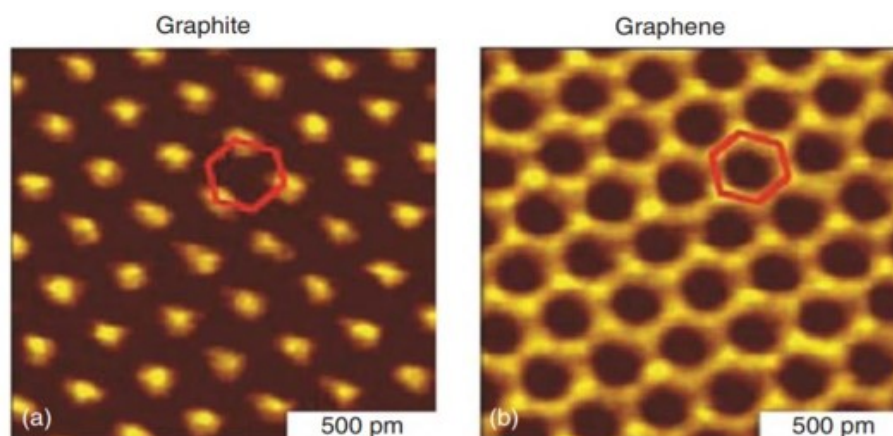


Figure 1.2: Atomic resolution STM images of the (a) graphite surface and (b) graphene [27].

With AFM, which can provide images of true topography also on a larger scale, it is possible to distinguish step edges ranging from single atomic step to several atomic layers on HOPG surface [28]. The number of step edges per unit area depends on the HOPG sample quality.

The mechanical, thermal, and chemical stability of graphite makes HOPG of great interest as electrode in traditional electrochemical cells [29] and, in this framework, the mosaic spread angle and crystallite size are crucial factors of which to take into account when considering HOPG electrochemistry. In Figure 1.3, typical tapping-mode AFM images of the surface topography for two different grades (ZYA and ZYH) of scotch tape cleaved HOPG are presented [28]. These images clearly show that both basal and edge-plane sites can be found on HOPG surfaces, with a wide range of step-edge densities, evident across the different samples. In general, the surface structure has been considered to play a key role in HOPG electroactivity. Consequently, deep and precise characterization of the HOPG surface structure and properties is essential to establish unequivocal structure-function correlations. This is particularly relevant in studies of the electrochemical activity of HOPG, where the majority of the early works has suggested that HOPG electroactivity is dominated, or controlled entirely, by edge planes, with the basal plane providing little or no contribution [12, 29–31].

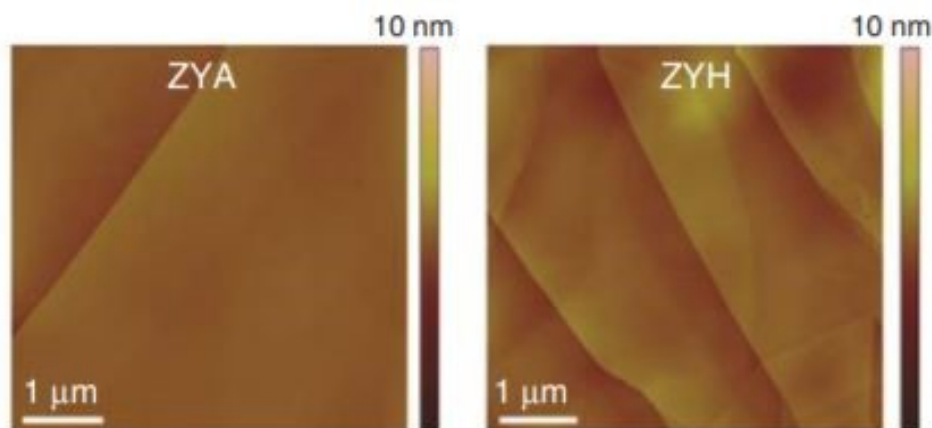


Figure 1.3: AFM images of freshly cleaved HOPG surfaces of ZYA and ZYH grade [28].

Cleaved HOPG has microstructures that may influence particular electrochemical reactions. Understanding the impact of these structures on electrochemistry requires that measurements must be made in small sample regions. This necessitates the use of microscale/nanoscale techniques on known areas of the surface. With complementarity, macroscopic characterisation may be valuable, but need to be carried out under conditions where the measurement timescale is varied over a wide dynamic range to probe sites with potentially different reactivity. Therefore, if the activity is structure-dependent, and the reaction involves a diffusional component, the activity can vary spatially in a nontrivial way that will be difficult to model, even with electrode schemes that adopt rather idealized views of heterogeneous activity [32]. A further issue is that the electrochemistry should be viewed as dynamic (time-dependent), following HOPG cleavage. This originates from several reasons. First, planar sp^2 carbon (graphene, graphite, etc.) tends to the adventitious adsorption of atmospheric contaminants, which have an impact on various properties, from wetting [33] to electrochemistry [28]. Second, after cleavage, the exposed surface layers undergo other chemical changes, such as oxidation at reactive dangling bonds and delamination or detachment of some flakes [27, 28]. These factors mean that electrochemical measurements of HOPG should be made immediately after cleavage, and also that the time evolution of treated HOPG activity is of great interest to truly understand these systems [34].

The study of the basal plane and surface defect electroactivity is essential to evaluate the applicability of HOPG in commercial devices and protocols (e.g. ion transfer batteries, graphene production in liquid phase). The redox processes², occurring on the HOPG-electrolyte³ interface, can be followed by different techniques (potentiostatic, polarographic, diffractive, optical, etc.) and under different solutions. Significant features of HOPG-electrolyte systems have been discovered by combining traditional STM and AFM techniques with other ones, closely related to electrochemistry and, in particular, with the so-called cyclic voltammetry (CV) [35, 36]. The latter is a potentiodynamic measurement, where the sample potential is linearly ramped versus time and the flowing current is plotted versus the applied voltage.

²An oxidation-reduction (redox) reaction is a type of chemical reaction that involves a transfer of electrons between two species (molecule, atom, or ion). Reduction and oxidation are two contemporaneous semi-reactions: the chemical species giving electrons is oxidized, while the chemical species accepting the electrons is reduced.

³An electrolyte is a substance that produces an electrically conducting solution when dissolved in a polar solvent, such as water. The dissolved electrolyte separates into cations and anions, which disperse uniformly through the solvent.

2 Graphite Intercalation Compounds

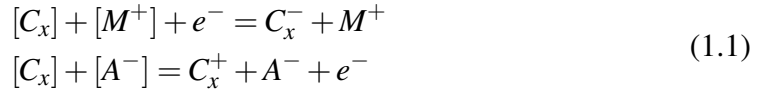
The intercalation process may be defined as the insertion of guest ions, atoms, or molecules into the interplanar voids of a stacked structure without destruction of the host layered bonding network [37]. The result of any intercalation process that occurs on graphite is called Graphite Intercalation Compounds (GIC). Intercalation of atoms or molecules with different masses gives rise to a wide variety of electrical, thermal, and magnetic properties [38]. GICs have potential as highly conductive materials [38]. With metal chloride or pentafluoride intercalants, such as antimony pentafluoride (SbF_5) and arsenic pentafluoride (AsF_5), GICs received much interest since the 1970s [38]. For example, AsF_5 -GIC has slightly higher σ ($6.3 \times 10^5 \text{ Scm}^{-1}$), than bulk Cu ($5.9 \times 10^5 \text{ Scm}^{-1}$), while the graphite in-plane σ is $\sim 4.5 \times 10^4 \text{ Scm}^{-1}$ [11]. The σ increase is assigned to injection of carriers from the intercalate layer, with low mobility, to the graphite layers, with high mobility [38]. GICs can be superconducting [39], with transition T up to 11.5 K for CaC_6 GICs, at ambient pressure [40]. GICs are also promising for hydrogen storage, due to a larger interlayer spacing [41]. GICs are commercialized in batteries, in particular in Li-ion batteries, since the 1970s. GICs have also been used as negative electrodes (anode during discharge) in Li-ion batteries, with the introduction of solid electrolytes [42]. A certain number of approaches have been developed over the years for GIC production, starting from solid, liquid, or gaseous reagents [11]. A common GIC production strategy is the two-zone vapor transport [38], exploiting temperature differences between graphite and intercalants. GICs can be produced in single (for binary or ternary GICs) or multiple steps, the latter when direct intercalation is not possible. Hundreds of GICs with donor (alkali, alkali earth metals, lanthanides, metal alloys or ternary compounds, etc.) or acceptor intercalants (i.e., halogens, halogen mixtures, metal chlorides, acidic oxides, etc.) have been reported [38].

3 HOPG intercalation in aqueous acid solutions

Some solvated electrolytes are able to intercalate inside a stratified crystal structure, screening the interlayer interaction and promoting the crystal delamination in aqueous solutions. This phenomenon has been extensively exploited by the industrial field of flat flexible electronics, where graphene is principally used. The significant results present in the literature [43,44], encouraged to extend electrochemical exfoliation strategies to a wider class of layered crystals, such as MnO_2 , MoS_2 , etc. [45], even if some problems have been encountered, especially related to the difficulty in finding the proper electrolyte. In graphene production applications, traditionally used electrolytes are sulfuric (H_2SO_4), perchloric (HClO_4), and nitric (HNO_3) acids. These solutions have strong oxidation effects, which could generate deformities in exfoliated graphene sheets. In order to downsize this problem, other electrolytes (alkaline solutions, sulfonate salts, and phosphate buffer solution) are to date adopted as intercalating agents [44,46]. After intercalation, a gentle sonication is used to obtain the HOPG delamination in graphene foils, which are dispersed in a solution and sold for many purposes. In liquid phase, graphene is found oxidized (GO) and shows typical lateral dimensions of hundreds of nanometers. A crucial point for effective application in electronics is the structural quality of the produced sheets. For this reason, many studies have been focused mainly on the characterization of the exfoliated graphene flakes [47, 48], with respect to on HOPG parent-crystal.

3.1 Theoretical models

The fundamental principles of the acid electrochemical intercalation process in graphite have been largely studied in the past [49–52]. Ions from acids penetrate at precise electrochemical (EC) potentials into the Van der Waals gaps between the carbon layers and enlarge the interlayer graphite distance. Charges are accepted into the carbon host lattice, according to the equations 1.1 [50], for both the cathodic and the anodic process.



where M^+ and A^- are the cation and the anion, respectively. C_x represents the stoichiometric amount of graphite carbon atoms involved in the charge-transfer with the electrolyte solution. The GICs structure is theoretically described by a model that suggests the formation of a statistically regular array of occupied/unoccupied layers, also called stage formation [50, 53]. In a GIC of stage n , the graphene interlayer containing intercalated ions is separated by $(n-1)$ uncontaminated interlayers. The scheme in Figure 1.4 depicts four consecutive stages.

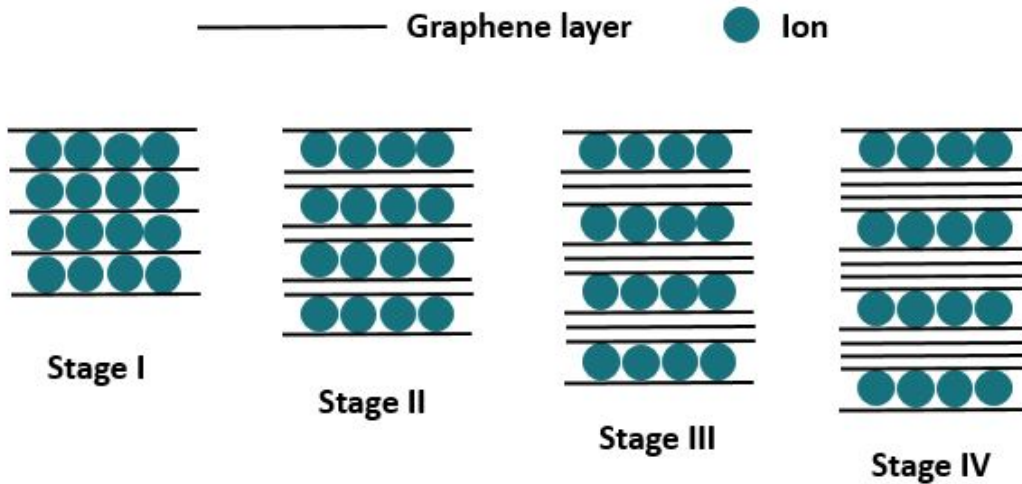
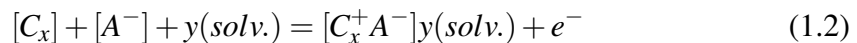


Figure 1.4: Schematic representation of the intercalation stage in four different GIC configurations. Solid black lines represent the carbon layers and balls represent the intercalated ions.

The above-mentioned model for GICs needs refinement if the electrolyte is a water-based solution and the solvent can intercalate into the graphite lattice. In this case, ternary phases $[C_x^+A^-]y(solv.)$ are also produced according to Equation 1.2, where A^- is an anion (a similar equation describes solvated-cations intercalation):



The degree of solvation (i.e the ratio between acid ions and solvent molecules) is expressed by y in Equation 1.2, it defines different possible molecular configuration. These are collected into 2D and 3D solvated phases as main groups, as represented in Figure 1.5 [53]. In the 2D solvates, the distance between the carbon layers is determined either by the size of the solvent molecule or by the size of the ion [54].

In HOPG intercalation, by applying a suitable EC potential to the graphite sample immersed in an aqueous acid solution, the ions are forced to intercalate within the graphite layers [46]. The main advantage of this method consists in the possibility of choosing

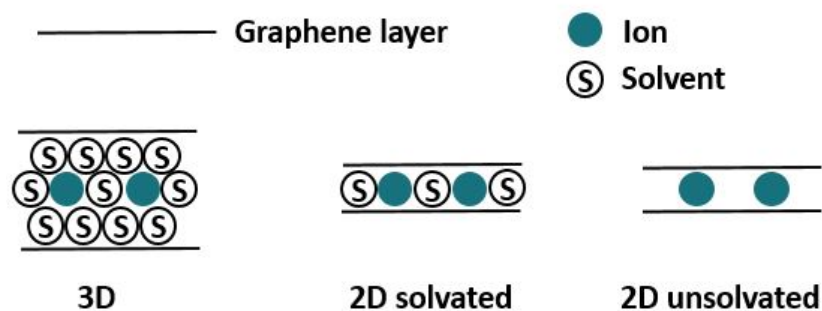


Figure 1.5: Schematic representation of 3D and 2D solvated intercalated ions in graphite. S is for solvent, solid balls represent the ions, solid black lines are for carbon layers. The basic 2D unsolvated model is reported for comparison [53].

the starting time and the kinetics of the process. Low-index GIC stages are easily obtained during HOPG oxidation in a liquid solution. In this case, HOPG is positively biased, with respect to a standard hydrogen electrode (SHE), at quite high (order of volts) EC potentials. The HOPG anodic behavior varies with the specifically used electrolytes. There are two main acid classes [49]: the phosphoric acid group (e.g. H_3PO_4 , HCl , etc.) and the sulfuric acid group (i.e. H_2SO_4 , HClO_4 , etc.). When graphite is immersed in an electrolyte of the phosphoric group and a high EC potential is applied, the basal plane is attacked by the oxidation processes and carbon dissolution is probable. The same phenomena are expected also for electrolytes belong to the second class, but in addition swellings of the HOPG surface and damage of the internal graphite structure have been observed [46, 52, 55–58].

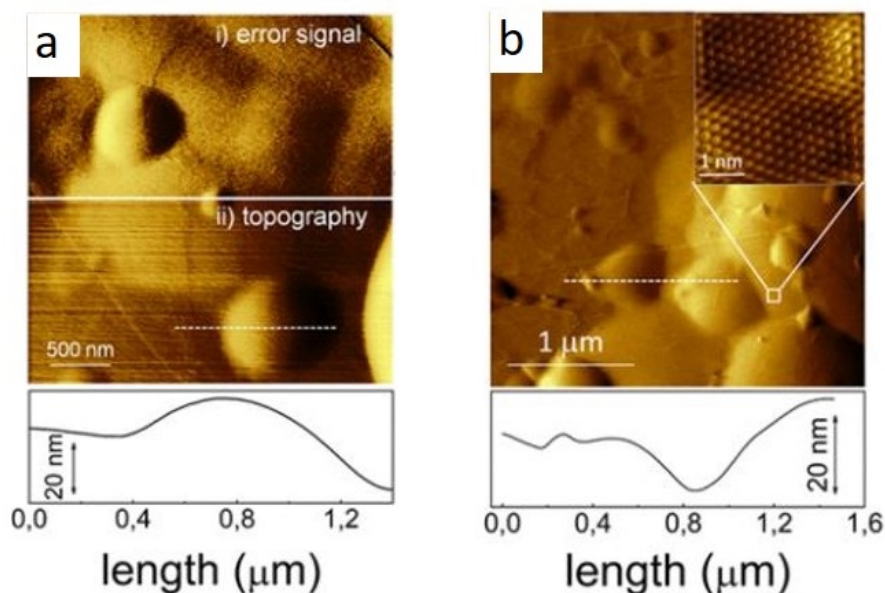


Figure 1.6: AFM images of graphite surface immersed in (a) 2 M HClO_4 solution and (b) 1 M H_2SO_4 , after anion intercalation and blister formation. (Inset) Atomic resolution STM image. Adapted from [59].

The crystal evolution is even more complicated when traditionally diluted acids, i.e. 2 M^4 or less, are used as electrolytes, as pointed out in the work of Alsmeyer and

⁴Molar concentration (M) is a solute concentration expressed in the number of moles of solute per liter of solu-

McCreer [60]. The authors highlighted the development of side reactions, such as oxidation, in correspondence with the intercalation process and proposed that graphite oxides (GO) follow the first stages of GIC formation. Furthermore, they observed that surface bubbles (called blisters) grown on the HOPG surface after anion intercalation. These findings have also been confirmed, more recently, by a combined AFM/STM investigation [59], of which some results are reported in Figure 1.6. Such outcomes shed light on the first stages of the graphite intercalation process, when HClO_4 or H_2SO_4 diluted solutions are used, and also on their peculiar effects with respect to other electrolytes, which do not cause blisters growth.

From an interpretative point of view, Royce W. Murray and co-workers succeeded in summarizing the experimental result, obtained up to that moment, in an original interpretative model of intercalated HOPG in diluted electrolytic solutions [56]. In this work, GIC phases and blister evolution are reported. In Figure 1.7, different steps of the HOPG anion intercalation are summarised, according to Murray's model:

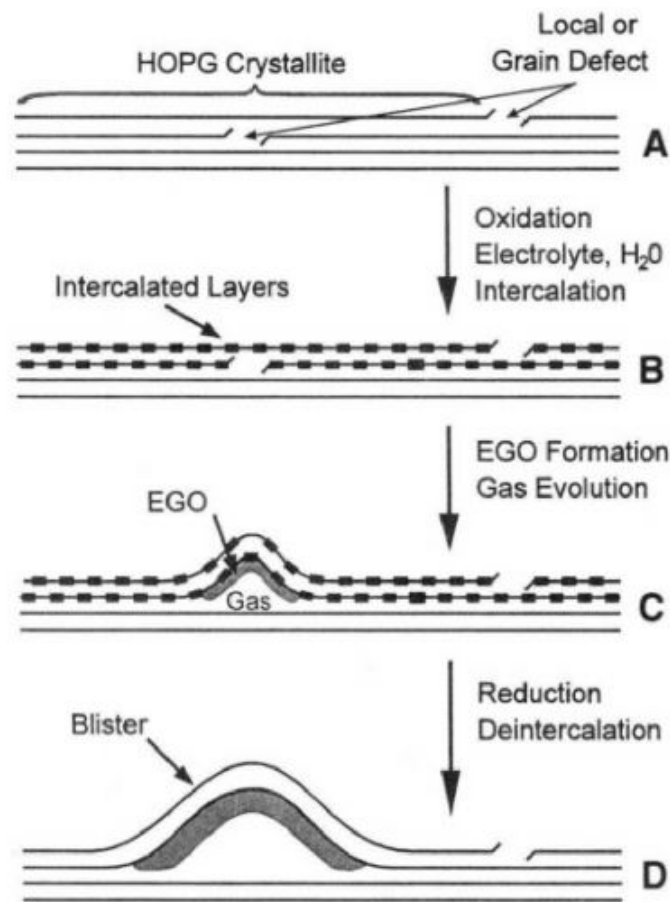


Figure 1.7: Model of blister formation and growth: A - cross section of the basal HOPG plane before the oxidation. Lines correspond to HOPG layers (graphene). Surface and bulk defect sites (e.g. crystalline grain boundaries, step edges, etc.) are also depicted. B - when HOPG is positively biased, carbon oxidation takes place. Dashed lines indicate areas where solvated anion intercalation occurred. C - initial blister growth. The grey shaded area represents graphite oxide. D - final and stable blister structure [56].

- A) HOPG crystal defects (steps, grain borders, holes, kinks, adatoms, valleys) are direct access to solvated anions, that insert through the interlayer spacing.

- B) As soon as EC potentials are applied to the graphite electrode, solvated anions oxidize carbon, i.e. electrochemical GO (EGO) formation starts.
- C) The HOPG oxidation produces specific gases (CO, CO₂, O₂) that start to swell the graphite surface, resulting in the blister formation.
- D) The blister size is contained by the graphite layer (graphene) strain, which stabilizes the surface morphology.

Murray model becomes insufficient when chemical and physical intercalation mechanisms, acting on pristine graphite from the molecular to the nano-scale, are investigated, opening new fascinating questions. For example, it might be interesting to give an experimental proof of the concrete access of solvated anions through the HOPG surface defects. Another purpose is linking the morphological and structural changes occurring on pristine HOPG after the first stage of EC anion intercalation, originally studied in pioneering works by Alliata et al. [61, 62], to the chemical alteration due to the side reactions of the EC strategy. Tracing the evolution and the spatial arrangement of the molecular species (acid ions and gases), involved in the EC intercalation from the HOPG surface to the crystal bulk, is another appealing target. Finally, it might also be very useful to determine the chemical and structural differences between GIC and pristine HOPG and to follow the occurrence of these kinds of changes.

Concerning the just mentioned fact-finding purposes, some new experimental efforts successfully found the time scale of blistering evolution employing EC-Scanning Tunneling microscopy (EC-STM), Cyclic Voltammetry (CV), and Normal-Pulse Voltammetry (NPV) [34, 57, 59]. These results, and the detailed analysis of the electrolyte characteristics (e.g., solution, pH, or temperature), show that the graphite basal plane swells as soon as the oxygen evolution potential (OEP) is reached [63–65], thus suggesting a first refinement of the theoretical interpretative model. However, microscopic techniques are not suitable when a more "chemical" analysis is required. For this target, the authors exploited Raman spectroscopy to analyze the HOPG surface evolution, in situ, during the intercalation CV [57, 58]. Raman can give a mean characterization on the sub-millimetric length scale (excitation spot size). As a consequence of light penetration length, HOPG structural changes on both the surface and the first graphite layers underneath are observed.

To date, highly sensitive analysis of the chemical species involved in the intercalation process, together with an investigation of their penetration length inside the crystal is still missing.

The main object of my thesis work is to give a complete picture of the HOPG surface chemical and physical makeup, after the first stages of EC anion intercalation. This was achieved by low energy ion beam analysis application to different model systems and in combination with other surface-sensitive techniques. The general principles of the Secondary Ion Mass Spectrometry (SIMS) technique, based on the use of low energy ion beams as probes and, more in particular, of the Time of Flight-SIMS (ToF-SIMS) instrumentation, will be described in detail in the next chapter.

Chapter 2

Low energy ion beam analysis

High energy probes-based techniques are regarded as a specialist interest, pursued in large laboratories able to afford expensive facilities. Despite this, the pretty recent growth in applications of low energy ion beam techniques, such as secondary ion mass spectrometry, has increased the general interest of the scientific community, in particular of the material science community, on the properties of ion beams and their usefulness as probes for condensed matter targets. The main reason for the recent development of these analysis techniques is that it has been possible to implement the low energy ion beams in laboratory-sized instrumentation. Ion beam techniques fall naturally into two categories:

- High energy techniques, with more than 100 keV and usually more than 500 keV incident ions.
- Low energy techniques, with less than 50 keV and usually less than 10 keV incident ions.

Among the high-energy techniques, high energy ion scattering (RBS) is the simplest technique to apply and had become a routine tool, together with channeling (RBS-C), for many applications, including the characterisation of semiconductors and other thin film and crystalline materials. Ion induced X-rays (PIXE), often overshadowed by X-ray fluorescence and other related techniques, had experienced a growth since 1970 because of their great sensitivity. Another example is the Prompt Nuclear Reaction analysis (NRA), a very complex technique offering different capabilities in surface and depth analysis. The development of low-energy ion analysis approaches, such as Secondary Ion Mass Spectrometry (SIMS), low energy ion scattering (LEIS), and other related methods have become rapidly prominent since the early 1970s, with the availability of commercial instruments. Low-energy ion beam techniques have, as a peculiar feature, a great surface sensitivity. The quantitative interpretation of experimental results is nowadays an area of active physics interest.

1 Secondary Ion Mass Spectrometry: general principles

Secondary ion mass spectrometry is a powerful and versatile surface analysis technique. The basic principle of SIMS is the detection of charged atoms and molecular fragments, ejected from the surface of a condensed phase sample under heavy particle bombardment. The energy range of the projectile particles (ions or neutrals) is in general of some keV. During the bombardment, surface particles could be sputtered, while the bombarding species, called primary species, are back-scattered or implanted into

the condensed phase of the target. The surface particles sputtering is one of the many phenomena happening during the surface bombardment. Generally, the ion-collision-induced emission events can include also photon and electron emission, as depicted in Figure 2.1.

The crucial goal of any surface analytical technique is to obtain information about the structural and compositional state of the sample surface. Such kind of details, in SIMS, comes from the emission of secondary ions that are mass (energy) separated by different combinations of instrumental setup and analyser.

In order to properly interpret the secondary ion mass spectra, it is fundamental to be aware of the processes leading to the emission (sputtering) of the charged particles from an ion-bombarded solid. The impact of a primary particle on a target causes an energy and momentum transfer at the impact point and to a limited area around it. The results are a change of the lattice structure of the analysed sample and a loss of surface material. All the modifications introduced by the ion bombardment to the original state of the target must be taken into account to get as much complete information as possible from the analysis of the results of a SIMS experiment.

The description of the sputtering phenomenon is still the object of many research efforts. SIMS deals with the analysis of secondary ions, and the ionisation occurs from the material surface, close to the emission point. This means that, for example, the yield of the secondary ions is strongly influenced by the electronic state of the analysed material.

The basic SIMS equation for the secondary ion current of a chemical species m is

$$I_m = I_p y_m \alpha \theta_m \mu \quad (2.1)$$

where I_m is the secondary ion current of the species m , I_p is the primary particle flux, y_m is the sputter yield, α is the ionisation probability, θ_m is the fractional concentration of the species m in the surface region of the target and μ is a parameter that includes the transmission yield of the analysis system.

Several theoretical models, based also on molecular dynamics simulations, are aiming to the accurate estimation of some of the just mentioned fundamental parameters, in particular the sputter yield (y_m).

The sputter yield is defined as the number of emitted target atoms per primary ion and its variability strongly influences the intensity of the detected ionized species from an ion-bombarded material. It increases linearly with the primary ions flux, but not linearly with primary particle mass, charge, and energy. The crystallinity and the topography of the bombarded sample, in combination with the incident angle relative to the surface normal, also affect the sputter yield. Generally, the larger the mass of the bombarding particle, the closer to the surface the energy will be deposited, and the greater will be the y_m value. The most accepted theory for the quantitative interpretation of the sputtering features is the *collision cascade model* [66]. This model, developed in the 1960s, assumes that sputtering occurs by incident particle bombardment at small current and fluence¹ values. It describes the energy and momentum transfer of the primary particles to the target through the concept of *cascades* of energetic binary collisions. The sputtering of atoms is a consequence of collisions cascades intersecting the surface and, in a binary collision, transferring to a surface particle energy and momentum large enough to overcome the binding force of the analysed solid. These collisions occur also between recoil and stationary target particles. Such a theory explains the energy distribution of the ejected particles, as well as the sputter yield dependence on primary

¹In SIMS analysis expressed in ions/cm²

energy, angle of incidence, mass, and atomic number of the target species.

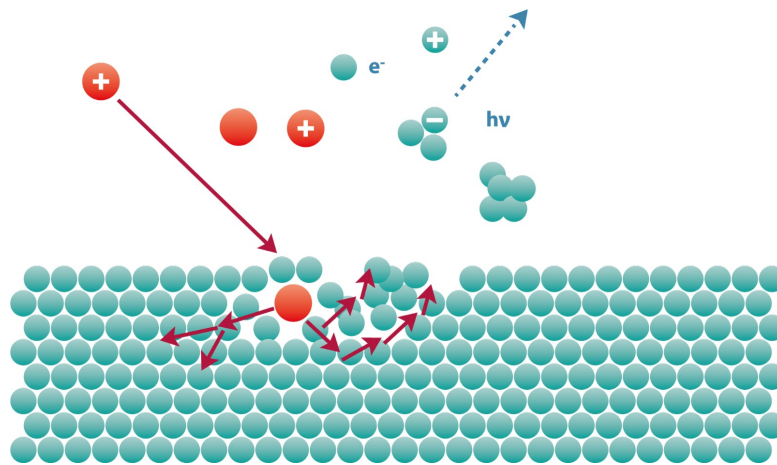


Figure 2.1: Primary ion bombardment in SIMS. The primary ions are backscattered or implanted in the target surface. In this case, it gives rise to collision cascades and the ejection of neutral and ionised fragments.

The charge state (i.e. the ionisation mechanism) of the sputtered species is not explained by this theory, and how the impact of a keV projectile finally leads to the detected ions is still not yet entirely clear. Starting from these pioneering results [66], cascade theory has been improved by including low-energy projectile ions case, or, for example, the study of non-elemental targets. Nowadays, the quality of collision cascade model predictions has been extensively redefined and improved.

In some approaches to the study of the SIMS technique, there is a strong tendency to focus on the physics of the primary ion-lattice interaction; oppositely, chemists concentrate on the detected ions and the deductive information obtained by the collected signals. As a general remark, it is essential to link the experimental evidence and also the theoretical concepts of the ion formation to the type of instrument you have chosen to use. This because a mass spectrometer samples only a specific fraction of the initial ion population that is generated by the primary beam bombardment, and the selection of this fraction is often instrument-dependent.

2 Ion-solid interaction

Ions, impinging on a surface, transfer their energy to the target atoms through several collisions. After one or more collisions, a fraction of the ions can be back-scattered or forward scattered, but the majority comes to a stop within the bombarded sample. The collision cascade is relevant for defining the number of recoils set in motion in the target by the ions probe. This determines the damage distribution in the target, the atomic transfer, and, hence, mixing in non-elemental targets and surface-topographical changes. These latter extend from the atomic scale (i.e. surface vacancies) to the larger-scale surface structures, like the formation of craters. The number of energetic recoils, generated close to the surface affect the sputtering of the target. The last fundamental process is at the basis of the SIMS operation. However, many other processes, which will be mentioned below, participate to modify the target during the irradiation and, hence, also need to be known.

2.1 Scattering cross section

In first approximation, it is possible to consider the target to be composed of free atoms that are at rest. This remains true as long as the energy of the primary particles is much larger than the binding and kinetic energy of the bombarded sample atoms. The atom-ion (in the case of ionic primary particles) pairs interact so closely during the collision, that the mutual interaction with the other atoms of the target, placed at relatively greater distances, can be neglected. Therefore, in SIMS the target-probe collisions may be considered as binary processes between two particles and, in the energy range usually encountered (up to 30 keV), they can be described by classical mechanics. In a close collision of heavy particles, there is, in general, a strong coupling between the translational² and the electronic energy transfer. Therefore, *nuclear* collisions are, strictly speaking, not elastic, because a collision between heavy particles can be considered an *elastic* process as long as the energy transferred to the electronic states is neglected. However, electronic and nuclear interactions may be treated as independent processes in first approximation, as their energy scales are different. The collision cascade model starts from the just-mentioned assessment [66]. A target atom hit by an incoming particle (e.g., ion) is set into motion (recoil atom) with a given speed, depending on the energy of the ion and the closeness of the collision. A part of the target atom energy is then transferred to other target atoms in binary collisions. The trajectories of the impinging particle and the target atom, with masses M_1 and M_2 respectively, are schematically shown in Figure 2.2, in the laboratory coordinate system.

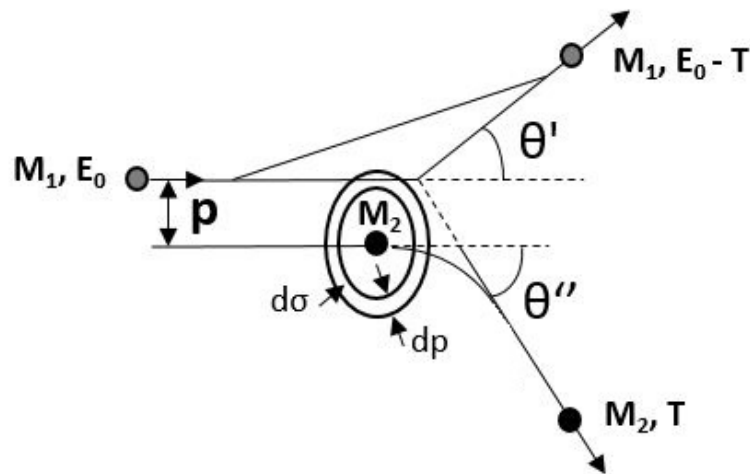


Figure 2.2: Trajectories of an ion (M_1) and atom (M_2) in a binary collision in the laboratory coordinate system. θ' and θ'' are the deflection and recoil angles, respectively, of ion and atom; p is the impact parameter and $d\sigma$ is the differential collision cross section.

A particle M_1 , arriving with an impact parameter p , undergoes a deflection angle θ' , which can be calculated knowing the repelling potential between the particles. The particle M_2 is at rest, in the laboratory coordinate system. The number of particles in a beam, with an impact parameter in the interval dp , is proportional to the differential cross section for scattering, defined as $d\sigma = 2\pi p dp$. Moving to the center of mass system, the absolute velocities of the projectile and recoil atoms are unchanged

²Energy relates to the displacement of atoms or molecules in the space.

by collisions and the two particles are scattered, in this case, through a common (polar) scattering angle ϕ , related to the deflection angles θ' and θ'' in Figure 2.2. The expression of the differential cross section in terms of the angle ϕ is:

$$d\sigma = -2\pi p(\phi) \frac{dp(\phi)}{d\phi} d\phi \quad (2.2)$$

Here, the negative sign indicates that an increase in p gives a decrease in ϕ . For one scattering center, the probability that a certain type of collision occurs is given by the differential cross section through the $d\sigma$ element around the direction ϕ . In the center of mass system it becomes:

$$d\sigma_{cms}[cm^2] = -2 \frac{p(\phi)}{\sin\phi} \frac{dp}{d\phi} d\phi d\Omega \quad (2.3)$$

where $d\Omega$ is the solid angle element.

In the collision process description we are not mainly interested in the details of the particle trajectories, but rather in the statistics of the energy transfer.

If a particle of energy E moves a distance ΔR in a random medium of atomic number density N , consisting of particles at rest, the probability dP of undergoing a collision, with energy transfer between T and $T+dT$ is

$$dP = N\Delta R\sigma(E, T)dT \quad (2.4)$$

The cross section, $\sigma(E, T)$, can be calculated from the interaction potential of the two colliding particles. In solids, the particle interaction is of many-body³ nature and it depends on the local atomic environment of the two interacting species. Many processes, classified as low-energy processes, are strongly influenced by the environment-dependence of the particle interaction in a solid. Such phenomena are described through molecular-dynamics approaches in many works present in literature [67–72]. Nevertheless, for higher-energy processes, the simplest pair-potential description, for two electrical point charges, is usually a reasonable approximation. Two close (enough) atoms, with atomic charge Z_1 and Z_2 , feel the effect of a repulsive force. When the atomic nuclei are so close that their Coulomb interaction is not shielded, even by the innermost core electrons, their potential energy is $V(r)=Z_1Z_2e^2/r$, where e is the elementary charge and r the distance of the two nuclei. From the inter-atomic potential $V(r)$ it is possible to find the scattering angle ϕ in the center of mass system:

$$\phi = \pi - 2p \int_{r_{\min}}^{\infty} \frac{dr/r^2}{[1 - V(r)/E_r - p^2/r^2]^{1/2}} \quad (2.5)$$

where E_r is the energy in the center of mass system and p is the impact parameter in Figure 2.2. By integration of the Equation (2.5), it is possible to obtain $p(\phi)$, hence the $dp/d\phi$ expression, to replace in the differential cross section in Equation (2.3). However, in the interaction processes of SIMS, the particle energy scales are relatively small and the nuclei interaction is partially screened by the electron cloud. The interaction potential may be approximated by a shielding function $\chi(r)$ as

$$V(r) = \frac{Z_1Z_2e^2}{r} \chi(r/a) \quad (2.6)$$

³Many-body problem is a general name attributed to the study of the properties of a vast category of physical microscopic systems made of many interacting particles, often on the order of the Avogadro number. Microscopic implies that quantum mechanics has to be used to provide an accurate description of the system. While the underlying physical laws that govern the motion of each particle may (or may not) be simple, the study of the collection of particles can be extremely complex.

where the screening length a depends on the atomic charges, coming from considerations similar to those of the Thomas-Fermi theory of the atom. Starting from the potential approximation in Equation 2.6, it can be convenient to scale energies to the Coulomb energy at the distance a . Thus, Lindhard's reduced energy expression:

$$\varepsilon = \frac{aE_{\text{rel}}}{Z_1 Z_2 e^2} \quad (2.7)$$

usually gives the relative energy $E_{\text{rel}} = M_2 E / (M_1 + M_2)$, between a hitting atom of mass M_1 and energy E and an atom at rest of mass M_2 .

For qualitative thoughts, it may be useful to approximate the potential by a power-law expression:

$$V(r) = Kr^{-1/m} \quad (2.8)$$

with $0 \leq m \leq 1$. For high energies ($\varepsilon \gg 1$), m is equal to 1; for $0.1 \lesssim \varepsilon \lesssim 2$, $m = 1/2$ is considered a plausible value and for $\varepsilon \lesssim 10^{-3}$, $0 \leq m \lesssim 1/4$ is the standard m range.

Going back to the Equation 2.4 of the collision probability, the cross section can be estimated from the just mentioned power law potential [73, 74],

$$\sigma(E, T)dT = C_m E^{-2m} g(T/E) \frac{dT}{E} \quad (2.9)$$

where C_m is a constant value, related to the mass and the atomic charge of the colliding atoms, and g is a dimensionless function. The $g(y) = y^{-1-m}$ approximation [73] leads to the cross section expression:

$$\sigma(E, T)dT = C_m E^{-m} T^{-1-m} dT \quad (2.10)$$

Finally, the cross section constant is given by:

$$C_m = \frac{\pi}{2} \lambda_m a^2 \left(\frac{M_1}{M_2} \right)^m \left(\frac{2Z_1 Z_2 e^2}{a} \right)^{2m} \quad (2.11)$$

Here, the dimensionless number λ_m is tabulated for different values of the exponent m [66]. The low-energy value of the cross section constant C_0 has also been estimated [75].

2.2 Processes in target

Up to now, we have discussed the basic theory of the scattering of a projectile at one scattering center. However, scattering phenomena in a target take place at many scattering centers, successively. Furthermore, some fraction of the projectile energy would be dissipated to electrons. Such considerations led to the concept of total stopping power. It is also worth mentioning that some important quantities are involved in ion bombardment of a target, including the mean penetration depth, the mean projected range, the implantation profile, and the density distribution of the recoil atoms. Some fundamental equations, related to these parameters, will be briefly discussed in this section.

2.2.1 Nuclear stopping power

From the probability expression in Equation 2.4, the average energy loss of a particle of energy E , when travelling a path length ΔR is

$$\Delta E = \int T dP = N \Delta R \int T \sigma(E, T) dT \quad (2.12)$$

For an infinitesimal path length, $\Delta R \rightarrow dR$, the nuclear stopping power (energy loss per unit length) is defined as [76]

$$\frac{dE}{dR} [\text{eV/cm}] = -NS_n(E) \quad (2.13)$$

where $S_n(E) = Td\sigma$ [$\text{eV} \cdot \text{cm}^2$] is the nuclear stopping cross section. The expression of $S_n(E)$, in the case of a power law cross section (Equation 2.10) and for $M_1 = M_2$, is:

$$S_n(E) = \frac{1}{1-m} C_m E^{1-2m} \quad (2.14)$$

For $m = 0$ (hard interaction), the nuclear stopping power increases linearly with E , whereas around the maximum value of m (e.g. $m = 1/2$) it is constant.

2.2.2 Electronic stopping power

As mentioned in section 2.1, the theoretical treatment of elastic and inelastic collisions, between two heavy particles, can be separated. In analogy, it is possible to define, as previously done for the nuclear collisions, an electronic stopping cross section S_e and an inelastic energy loss as

$$\left(\frac{dE}{dR} \right)_e = -NS_e(E) \quad (2.15)$$

The electronic stopping cross section is far more difficult to determine than the nuclear cross section. The exact nature of such a dissipation process is still under experimental and theoretical investigations. A possible quantitative approximation [77] of the electronic stopping power value is given by:

$$\left(\frac{dE}{dR} \right)_e = -KE^{1/2} \quad (2.16)$$

Different values for K , depending on the mass and the charge of the impacting particles, are tabulated for a wide range of projectile-target combinations. The electronic energy loss becomes considerable for low Z -projectiles, but for many applications in SIMS, its contribution can be neglected. Finally, it is possible to define the total stopping power as:

$$\left(\frac{dE}{dR} \right) = -N[S_n(E) + S_e(E)] \quad (2.17)$$

2.2.3 Ion ranges

Talking about the ion penetration into solid targets, different types of range can be defined, schematically displayed in Figure 2.3. The ion enters the target at the point O , with the angle ψ , with respect to the surface normal, and describes a certain trajectory up to its rest at the point z . The range along the path R in Figure 2.3 is not of great practical interest. The transverse range R_\perp is defined as the normal distance of the endpoint z of an ion trajectory from the incident direction. The chord range R_c is less often used. The projected range R_p (or the penetration depth x) is a fairly simple quantity to calculate and, experimentally, it corresponds to an implantation profile taken at low projectile fluence. From equation 2.17, one can obtain an estimation for the average range \bar{R} , in the case of perpendicular incidence:

$$\bar{R}(E_0) = \int_0^{E_0} \frac{dE}{N(S_n(E) + S_e(E))} \quad (2.18)$$

where E_0 is the initial energy of the impinging ion on the target.

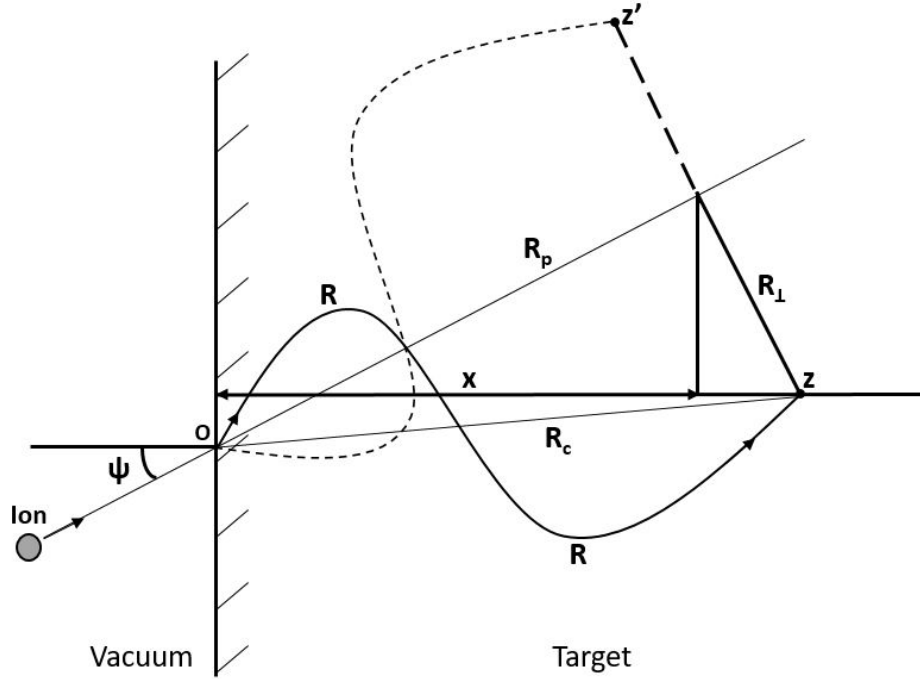


Figure 2.3: Definition of the different types of ion range. z is the endpoint of the trajectories. R : range along the path (pathlength); R_p : projected range, the projection of the range along the path on the initial direction of the ion; R_{\perp} : transverse range; R_c : chord range and $x = R_p \cos \psi$: penetration depth, the projection of R_p on the surface normal [76].

In first approximation, $\bar{R}(E_0)$ can be considered the average path length of the projectile, measured along its zig-zag way in the solid. Starting from such approximation, the mean projected range \bar{R}_p can be calculated. It is shorter than $\bar{R}(E_0)$ by a factor $f < 1$. For dominant nuclear stopping, i.e. neglecting the $S_e(E)$ contribution, and considering the power-law cross sections (eq. 2.10), \bar{R}_p scales with energy:

$$\bar{R}_p \propto \frac{E_0^{2m}}{NC_m} \quad (2.19)$$

Finally, the so-called projected range distribution is defined as $R(z)dz$; it gives the probability that the projectile is stopped at a depth between z and $z+dz$ inside the target. A wide series of theoretical calculation, including the evaluation of the range distribution (with the related errors), or of other quantities of interest, namely the sputter yield, mixing phenomena rate, clustering parameters, diffusion effects, and so on, are nowadays mainly achieved by Monte Carlo (MC) or Binary Collision Approximation (BCA) simulation methods. For not too high bombarding energies, Molecular Dynamics (MD) routines are also frequently used. Two examples of such kind of theoretical works are shown in Figure 2.4.

2.2.4 Recoil atoms spectrum and damage

As already mentioned in this chapter, the energy directly transferred by a projectile species to a target atom (primary recoil atom) can be sufficient, for this primary recoil,

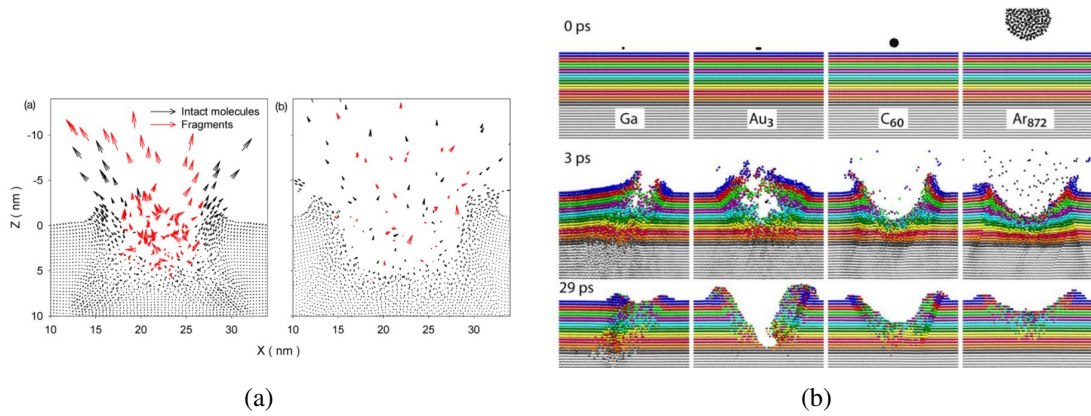


Figure 2.4: Two examples of simulation methods for (a) the study of the emission of benzene molecules and fragments upon C_{60} impact, by Molecular Dynamics computer simulations [78] and (b) the study of the differences between small cluster (Au_3), medium cluster (C_{60}), large cluster (Ar_{872}), and atomic (Ga) bombardment dynamic on Ag sample, by Monte Carlo approach [79]

to describe a trajectory of a certain length in the target. Ergo, the primary recoils can generate secondary recoils and so on. The number of recoil generations depends on the energy of the primary particle (e.g., ion) and the ion-target combination. The binary collisions model, at the base of the so-called *linear* collision cascade, could be no longer valid if the velocity of the recoil atoms is so small that they can not come very close to another lattice atom, even though they may interact with many lattice atoms simultaneously. In this case, the recoil energy is transferred to the lattice vibrations. The lattice interaction implies that a part of the kinetic energy, transferred to the target, comes directly from the impinging particle, and a part comes from the recoils of various generation number. This latter transferred energy is defined as the energy deposited during the atomic motion and its distribution plays a crucial role in the target damage evaluation caused by the ion bombardment.

If a collision cascade starts with an ion (or recoil) initial energy E_0 , the average number of recoil atoms set in motion with energy in the interval $(E, E + dE)$ is found to be:

$$F(E_0, E) = \Gamma_m \frac{E_0}{E^2} \quad (2.20)$$

Here, the parameter $\Gamma_m \cong 0.6$, slightly depends on the potential exponent m of Equation 2.10. The analytical expression in Equation 2.20 is in good agreement with the recoil density values calculated by molecular dynamics simulations [80]. From Equation 2.20, it follows that slow recoils are most abundant and in many cases will not move far away from their place of formation. In the case of heavy projectiles on lighter targets, however, the ranges of the faster (lighter) recoils may even be longer than the range of the projectiles. This led to a loss of symmetry in the damage and ionization distributions. Atomic-vs-polyatomic projectiles topic, including the computational prediction and comparison of sputter yields, diffusion, mixing and damage effects for SIMS experiments, has become of great interest in MC and MD simulations field (an example in Figure 2.4b).

The most common types of lattice imperfections are [76]:

- *Frenkel defects*. When an atom is displaced from its lattice site to an interstitial

position. The new site and its corresponding unoccupied position is called Frenkel pair.

- *Schottky defects.* When the displaced atom mentioned above is located at the crystal surface.
- *Dislocations.* A part of the lattice is displaced along a line with respect to the neighboring part, forming a line dislocation. If a part of the lattice is rotated with respect to the neighboring part, it forming a screw dislocation. Dislocations can form loops, reach the surface, or form networks through the crystal.
- *Disorder* Short-range or long-range disorder can disturb the ordered lattice structure.
- *Cluster formation* Defects may also form clusters of various structures.
- *Impurities* Also impurities can disturb the lattice or form clusters. If the impurities are gaseous, blistering may occur.
- *Amorphization* The most serious form of lattice distortion.

All these types of defects may be produced or annihilated by ion bombardment. In serious cases, these disturbances are accompanied by macroscopically measurable deformations. Surface roughness, induced by the above-mentioned defects, may have undesirable influence, especially on in-depth analyses in SIMS.

The number of defects generated by a collision cascade can be calculated from Equation 2.20, with the introduction of the displacement energy E_d .

The displacement energy of an atom is defined as the threshold energy needed to displace an atom, so that each recoil created with energy above E_d leads to a stable Frenkel pair, while recoils generated with energies below E_d return to their initial lattice position. Then the number of Frenkel pairs or vacancies is given by [81]:

$$N_{\text{defects}} = 0.4 \frac{E_0}{E} \quad (2.21)$$

A saturated state of damage is reached for a certain fluence of impinging ions. For ion energy in the keV region, fluence values in the $10^{11} - 10^{15}$ ions/cm² range are grouped in the low-fluence region [76]. Such a fluence will not change the crystallinity of a large set of materials, in which only individual defects, small clusters, and planar faults are observed. The actual number of defects found after a single ion impact may also lead to sample amorphisation. Fluence values higher than those of the low-fluence region led to critical changes of the surface starting morphology.

For SIMS analysis, it is important to know the amount of damage formed close to the surface or the near-surface interfaces. Surface defects at nanometric scale can be directly observed through microscopic techniques as Scanning Tunneling Microscopy (STM) [82].

As will be explained in the next sections of this thesis, the interpretation of the collected data from a SIMS experiment depends on the sputtering features, which, in turn, are direct or indirect consequences of each ion impact on the target.

It is worth mentioning that the binding energy of the lattice atoms (particularly at the surface) plays a crucial role in the damage mechanism due to the ion bombardment. The binding energy of a solid is comparable to its cohesion or sublimation energy, but an exact definition of the cohesion energy, in an ion beam experiment, is difficult because it is necessary to take into account the type and the number of bonds broken during the single collision process.

2.2.5 Recoil mixing

In the case of a not elemental target, consisting of different elements, each having its concentration depth profile along the sample, the movement of the recoils causes intermixing (ion-induced mixing) of the components and introduces a limit on the depth resolution of SIMS. It is possible to distinguish the primary recoil mixing, i.e. the displacement of target atoms in direct projectile-target collisions, and the cascade mixing, i.e. the displacement of target atoms by recoil-target atoms collisions in the cascade process. The sputtering from a compound sample is a fluence-dependent process that can lead to falsified concentration gradients in the target. This is the principal source of error in the ion-based surface-analysis techniques.

From a quantitative point of view, starting from the expression of the Frenkel pairs (Equation 2.21), it is possible to consider the average number of atoms $\Delta N(z \rightarrow z+\zeta)$ relocated by a single ion from the atomic layer at a depth z to a $z+\zeta$ depth. Then the total relocation out of the layer z is given by

$$N_{\text{reloc}} = \sum_{\zeta} \Delta N(z \rightarrow z + \zeta) \quad (2.22)$$

here, the sum is on all distances $|\zeta| > \zeta_{\text{min}}$, where ζ_{min} is a cut-off value.

2.3 Emission phenomena

When a target sample is bombarded by particle or ion beams, the following phenomena can be observed:

1. A portion of the impinging ions may be scattered directly from the surface or after having partially penetrated the target. If the target is a thin film, a fraction of the ions may also be transmitted.
2. Electrons may be emitted, at low ion energies, by Auger processes at the surface (potential emission of electrons) or by energy transfer from the incident ions (kinetic emission of electrons), if the kinetic energy of the ion is high enough to cause inner-shell ionisation of an atom in the solid.
3. Electromagnetic radiation may be emitted either by particles in the target or by particles leaving the target in excited states. The spectrum may be a single line, a band, or a continuous spectrum from the infrared to the X-ray regions.
4. Recoil atoms, which have received enough energy in collisions, may be ejected from the target. When the ejection of secondary particles occurs at the bombarded surface, it is called sputtering. The sputtered particles may be elemental atoms, molecules, clusters of atoms, or single or multiply charged ions. They may be in the ground or an excited state,

This latter phenomenon and, in particular, the sputtering process involving the secondary ions emission, is the basis of SIMS analysis. The physical mechanisms of sputtering, induced by impinging particles with energies in the eV - MeV range, are today mostly understood. Generally, in the 100 eV - keV range, sputtering is caused by atomic collisions between the incoming particles and the atoms in the surface layers of the target, i.e. the incident particles initiate a collision cascade between the lattice atoms in the solid. In the case of ion beams with energies in the MeV range, the energy exchange with electrons plays a major role in the surface erosion. As previously mentioned, a target atom is sputtered if it receives an energy component normal to the

surface larger than the surface binding energy. This energy is generally approximated by the heat of sublimation, which is smaller than the displacement energy necessary for creating a stable displacement (radiation damage in the bulk of a solid) [83]. This is the *physical sputtering*. It takes place for any target-particle probe combinations if the incident particles have energy above a threshold value in the 10 to few hundred eV range. Sputtering may be also enhanced or reduced if the incident particles form a chemical binding with the atoms of the bombarded material. This process is named *chemical sputtering*. Depending on the energy of the incident particles and the collision cross section between the incident particles and the atoms of the solid, several collision regimes can be identified in physical sputtering [66, 83]:

- The single knock-on regime, when the recoil atoms from the incident particles-target collisions receive sufficient energy to be sputtered, but not enough energy to generate a recoil cascade.
- The linear cascade regime, when the recoil atoms from the incident particle-target collisions receive sufficiently high energy to generate recoil cascades. Furthermore, the density of recoil atoms is low enough for knock-on collisions with atoms of the solid at rest to dominate and for collisions between moving atoms to be not frequent.
- The spike regime, in the case of heavy incidence particles, having a large collision cross-section, and for molecules or atom clusters as bombarding species. Here the density of recoil atoms is high enough for the majority of atoms in a certain volume (the spike volume) to set in motion.

For bombarding energies in the MeV range, additional processes, such as electronic sputtering, contribute to the surface erosion.

In crystalline targets, sputtering is largely influenced by the lattice structure.

The charged species generation (secondary ions generation) is at the base of the SIMS analysis working principle. For any sputtered surface species it is crucial to find out its secondary ion yield, determined by the sputter yield of the specific secondary particle and its ionisation probability. The separation of the sputtering and ionisation process is not strictly correct because they take place quasi-simultaneously and finally result in the emission of the respective secondary ion species. However, dealing with neutral particle generation and ionisation processes separately is quite common and helpful for the development of a common empirical model [76]. As already mentioned, the sputtering phenomenon is well-described by the linear cascade theory [66, 83]. By this theory, the sputter yield of different target-probe combination, and its dependence on primary ion energy, angle of incidence and masses, can be quantitatively predicted. In first approximation, such sputter yield is considered as the yield of atomic surface species, but any prediction on their charge state is not possible. A general assumption is that the ionisation probability of sputtered atoms depends on their ionisation energy, in the case of positive ion generation, and on their electron affinity, for secondary anions formation.

2.3.1 Sputter yields

In the following sputter yield description, the linear cascade regime scenario will be the general assumption. In any sputtering experiment, the most influential parameter is the sputter yield Y , which measures the sample erosion amount. In an elemental target, it is defined as:

$$Y = \frac{\text{Average number of atoms removed}}{\text{Incident particle}} \quad (2.23)$$

In the Y definition, the incident particles may be energetic ions or neutral atoms, molecules or atom clusters, but also neutrons, electrons or energetic photons [84]. For bombardment with monoatomic molecular ions, each incident atom is generally counted separately. In counting the removed atoms, only those from the solid are included, while incident particles, which are implanted and later emitted, are not taken into account. Analytically, a general integral transport equations is used [66, 83, 85, 86] to approximate the potential expression in Equation 2.8, with $0 \leq m < 0.5$, for the atom-atom collisions, neglecting the energy loss to electrons [66, 83]. The parameters to take into account in such analytical calculation are quite numerous, e.g. atomic mass of the projectiles, target chemistry, bombarding energy, surface binding energy, and so on. Nevertheless, a first order asymptotic solution achieved taking parameters in particular ranges, is [66, 83]:

$$Y(E_0, \theta_0) = \Lambda F_D(E_0, \theta_0, z = 0) \quad (2.24)$$

where E_0 and θ_0 are the energy and the angle of incidence, respectively. $F_D(E_0, \theta_0, z = 0)$ is the nuclear energy deposition function at depth $z = 0$, considering an infinite medium. It is proportional to the nuclear stopping power $S_n(E_0)$ (from Equation 2.14) of the incident ion in the solid.

Λ is a factor depending on the material, approximately given by

$$\Lambda = \frac{\Gamma_m}{8(1 - 2m)NC_m U_s^{1-2m}} \quad (2.25)$$

with Γ_m , the factor previously seen in Equation 2.20, and C_m , the cross section constant in Equation 2.11. The Λ factor can be further approximated by $\Lambda = 0.4/NU_s$, where U_s is the surface binding energy. Sputtering stops when the energy of the projectiles decreases below a certain threshold value. The threshold energy depends on the surface binding energy, the angle of incidence, and the mass ratio between target atoms and projectiles. At near-threshold energies, the collision cascade is not yet fully established (i.e., the regime is of the single knock-on).

In a sputter experiment, the particles are ejected with a broad distribution in energy, in all polar exit angles, relative to the surface normal. When an energetic projectile produces a recoil cascade in an infinite medium (i.e. without a surface), high-generation recoils forget the initial direction of the projectile, and the cascade becomes isotopic. Therefore, the particle flux, through an imaginary surface, is cosine-distributed. Despite this, for $E_0 \geq 10$ keV, there is an excess of measured sputtered particles in the direction perpendicular to the surface [87]. This may be explained in terms of target surface influence: since the surface acts as a drain on recoils, near to the surface they move preferentially towards the surface, rather than into the target. This establishes a cascade anisotropy. The angular distribution is also affected by the surface roughness and topography and by the target crystallinity.

The ejected particles are emitted predominantly as neutral atoms in the ground state with energies of few eVs; some are in excited energy state, but generally less than 5% are ions at different charge states, q . In the latter case, Y_q is the total sputter yield for atoms in state q , with $Y = \sum Y_q$.

The differential sputter yield defines the distributions of the sputtered particles. In SIMS, only emitted ions within a given energy and charge state, sputtered into a certain

angular range (sputter flux) are measured, therefore the differential sputter yield will be [88]:

$$\frac{\partial^3 Y_q \Delta E \Delta \Omega}{\partial E \partial^2 \Omega} = Y(E_0, 0) \frac{2}{\pi} (1 - 3m + 2m^2) \frac{U_s^{1-2m} E}{(E + U_s)^{3-2m}} |\cos \theta| \Delta E \Delta \Omega \quad (2.26)$$

The SIMS collected signal is generally proportional to the sputtering yield of the target species, and the charge state q of the secondary ions depends on the target composition and the bombardment conditions [76]. Therefore, numerous evaluations for SIMS signals calibration are indispensable. For example, in polycrystalline materials like HOPG, studied in this thesis work, the emission distribution is a superposition of each emission distribution from crystallites differently oriented in the bombarded area. At normal probe incidence, the angular distributions for amorphous and polycrystalline materials may be described, in first approximation, by a cosine distribution. For heavy ions and low bombarding energies, close to the threshold, more atoms are emitted at large angles, while for light ions and higher energies, more atoms leave the surface in the normal direction. At oblique probe incidence, the maximum of the emission distribution is shifted away from the incoming ion beam. In sputtering of compounds, the different constituents may be sputtered with slightly different angular distributions [76]. For $m = 0$ (i.e. hard interaction), the Equation 2.26 follows an E^{-2} law and has a maximum at half the surface binding energy, while for $m \cong 0$, it well describes measured energy distribution of sputtered atoms. Also at high emerging energies ($E \gg U_s$), the number of sputtered particles decreases proportionally to E^{-2} .

Many experimental and theoretical works have been made for systematically sputter yield evaluation of polycrystalline and single crystal target, bombarding with different impinging particles at different energies and angles of incidence.

Conversely, the sputter yield of a multicomponent system shows a less predictable trend. Several requirements have to be satisfied to get reliable and reproducible results [89]:

- The beam of incident particles (ions or neutrals) should have well-defined energy with a small energy width, especially at low energies, and a small angular divergence. The emitted beam should be mass-analysed, in order to separate different species (e.g., molecular ions from atomic ions). The incident fluence should be measured accurately, this requires the knowledge of the impinging ion current.
- The impurity content in the target should be negligible.
Due to the dependence of the yield on the angle of incidence, the target should be also flat. An initially polished surface will, however, generally become rough during particle bombardment. Implantation of the bombarding species into the target could also modify the sputter yield. Therefore, measurement of the yield versus the incident fluence is valuable to show the difference between low-fluence and saturation cases. For a sputtering measurement at a thin film target on a substrate, the film should be thick enough, that the underlying substrate does not modify the collision cascade in the film.
- The vacuum conditions should be good enough that the adsorption of residual gas species on the target during bombardment can be considered negligible.

The incident fluence on the target and the removed target material during SIMS experiments are parameters of crucial relevance, especially for depth profiling analysis.

The sputter yield, the beam fluence, and the removed material from the target (for in-depth analysis) are quantities strictly interrelated: knowing two of them, it is possible to extract, quite easily, the other two. The incident fluence is usually determined by the incident beam charge, while the removed material can be calculated by several methods [89], listed below.

- Mass change - The amount of material removed from an elemental target can be obtained through the measured mass change Δm . Then, the sputtering yield will be $Y = \frac{\Delta m}{M_2 n_1} N_0$, where M_2 is the target atomic mass, n_1 is the number of incident projectile ions (atoms), and N_0 is the Avogadro number. This formula is correct only if the implantation and trapping of bombarding projectiles into the target are negligible.
- Thickness change - The amount of material removed can be determined by the measurement of the thickness change of the sample, for example, with Rutherford back-scattering. The measured areal density before and after bombardment gives the yield. Other methods are X-ray analysis, nuclear reaction analysis, or methods using electrons such as an electron microprobe or Transmission Electron Microscopy (TEM). Mechanical methods, such as profilometer or Scanning Probe Microscopy (SPM) measurements, are exploited for sputtering crater determination, also in this thesis work.
- Spectroscopy method - A plasma column in front of the target may be used for exciting the sputtered neutrals, in this way specific emission lines are observed [90]. The method is fast and very sensitive.

Several efforts have been made to calculate sputtering yields in amorphous, polycrystalline, and single crystal targets [66, 83]. Besides the analytic approach, many sputter yield predictions have been made with models based on the binary collision approximation [91–93]. The calculated values are fitted with empirical formulas and then compared with experimental data. The reasoning for this procedure is that the experimental data often cover only a limited energy range, whereas missing values can be obtained by calculations. Another motive is that the possible systematic deviation between calculated and experimental data can show up more clearly. To cite some examples, generally in ion beam experiments, the target surface roughness, which may change even with ion fluence, is usually not known, while in theoretical calculations a nearly flat surface is assumed; due to the increase of the sputtering yield with an increasing angle of incidence, the experimental data at normal incidence generally give a higher value than the calculated one. However, simulations may suffer from insufficiently accurate interaction potentials or inelastic energy losses. Fitting parameters for sputter yield calculation, depending on energy and angle of incidence, for a wide range of impinging ion-target combination, can be found tabulated [89].

In Figure 2.5a, there is an example of a comparison between a fit of the energy-dependent sputter yield values and some experimental data points, measured by different authors for graphite bombarded with Xenon [89] at normal incidence. The angular-dependent fit of the sputter yield curve, for gold bombarded with Xenon at 10 keV, is shown in Figure 2.5b and it is compared to the yield measured in an experimental work [89].

The angular dependence of the measured sputtering yield is due to the roughness of the target. The yield at normal incidence is generally higher for a rough surface than for a flat one and the opposite is true for large angles of incidence. At about $\frac{\pi}{4}$ the values are approximately the same for flat and rough surfaces.

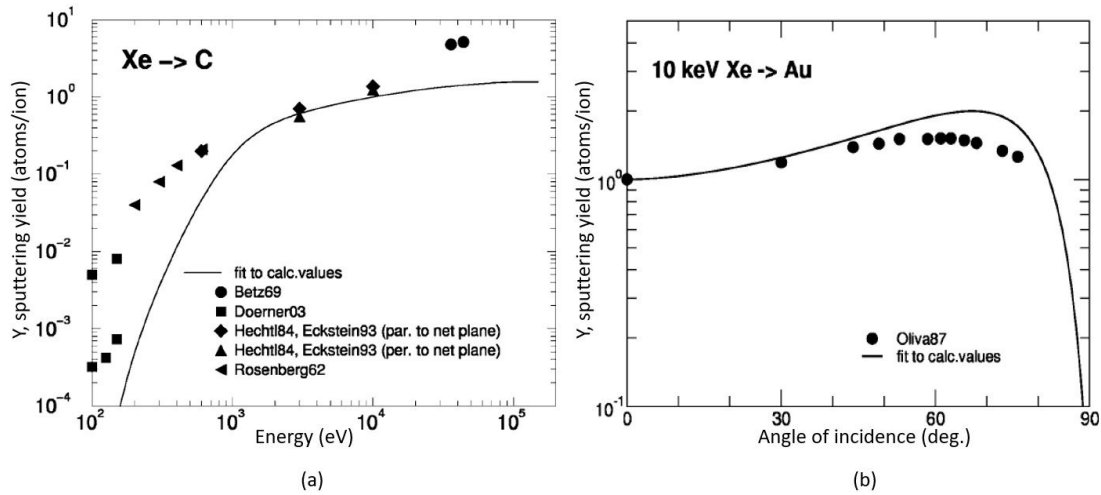


Figure 2.5: Energy dependence (a) of sputtering yield of graphite (C) bombarded at normal incidence with Xe and (b) comparison of measured and calculated angular dependence of sputtering yield for Au target bombarded with 10 keV Xe [89].

The depth resolution of the SIMS experiments is quantified by the depth from which sputtered atoms originate. For low-energy recoils, the Equation 2.25 gives the average depth of origin, defined as:

$$\Delta x = \frac{1}{NC_0} \quad (2.27)$$

The value of the low-energy stopping cross section C_0 originally resulted in 5 Å [94]. In more recent works, it was found that C_0 should be increased by a factor 2. The resulting origin depth of sputtered atoms is 2.5 Å [75], in reasonable agreement with experimental [95]. In analogy with the Equation 2.25, it is possible to obtain the dependence of Δx on energy E :

$$\Delta x = \frac{1}{1 - 2m} \frac{E^{2m}}{NC_m} \quad (2.28)$$

This means that higher-energy sputtered particles originate from greater depths. MD simulations typically show that all sputtered atoms come from the first target layer. With increasing energy, deeper-lying atoms also start to be emitted [96].

2.3.2 Preferential sputtering

Sputtering becomes a more complex phenomenon if the target consists of two or more different atomic species. Complications arise because the energy transfer from the projectiles to the various target species is not the same. The target composition often changes with its depth. In a multi-component sample the partial sputter yields Y_i , forming the total yield $\sum Y_i = Y_{\text{tot}}$, are defined, in the usual way, as the ratios of the sputtered atoms of component i per projectile. In compound targets, sputtering is fluence-dependent. Considering only collision processes, a distinction can be made between the deposition and the erosion regime. If more atoms are implanted than sputtered, deposition dominates. The border between the two regimes depends also on the incident angle. In both regimes, the steady state is reached if the partial yields become constant with increasing fluence. In the erosion case, the final depth distribution of the different species will form at the steady state and sufficiently high fluence. Such a depth profile will not change anymore with increasing fluence, although the target thickness

will decrease. Steady state is generally reached for an incident particle fluence, f_{eq} , at which a layer corresponding to the range R of the implanted ions is removed by sputtering. If the atomic density of the sputtered layer ρ is known, the steady state fluence, f_{eq} , is given by [97]:

$$f_{eq} = \frac{\rho R}{Y_{tot}} \quad (2.29)$$

R and Y_{tot} values depend on the projectile energy and their angle of incidence. R increases monotonically with energy, whereas Y_{tot} has a maximum at a certain energy. Considering the simple example of a homogeneous compound, containing elements A and B in concentration c_A and c_B respectively, the partial sputter yield Y_A from the generalisation of the yield formula in Equation 2.26 is

$$Y_A = c_A \frac{1}{8} \frac{[\Gamma_m F_D(E_0, \theta_0, z=0)]_A [\Delta x]_A}{U_A} \quad (2.30)$$

Here, U_A is the surface binding energy of the compound element A and Δx is the depth out of which the A-recoils may be ejected. The dependence of $\Gamma_m F_D$ and Δx on the nature of the element A (or B) can be determined in detail [66]:

$$\frac{Y_A}{Y_B} = \frac{c_A}{c_B} \left(\frac{M_B}{M_A} \right)^{2m} \left(\frac{U_B}{U_A} \right)^{1-2m} \quad (2.31)$$

The above-mentioned relation brings to notice three remarkable things:

- Sputtering of a compound target is non-stoichiometric at low fluences because the sputter yield ratio Y_A/Y_B is not proportional to the ratio of the surface concentration (preferential sputtering occurs).
- If $m = 0$, surface binding is the only source of deviation of the partial sputter yields from their stoichiometric values.
- If $U_A = U_B$ and $m \neq 0$, the lighter component will be preferentially sputtered, whereas the elemental atomic number is of no concern to the relative sputter yields. Such mass effect dominates the sputtering of isotopic mixtures.

The sputtering of isotope mixtures is also non-stoichiometric at low fluence. The isotope effect is usually described by the following parameter [98]:

$$\delta = \frac{Y_A c_B}{Y_B c_A} - 1 \quad (2.32)$$

that, according to Equation 2.31, can be also expressed as:

$$\delta = \left(\frac{M_B}{M_A} \right)^{2m} - 1 \quad (2.33)$$

Because of the small value of the power potential parameter m , for similar masses, the value of δ is of the order of a few percent. Measurements and computer simulations have shown that, below the energy value of 5 keV, the preferential sputtering becomes considerably more noticeable.

2.3.3 Cluster emission

Quite usually, besides monoatomic particles, large clusters are found in the sputtered secondary ion flux. Defining Y_n as the yield of clusters containing n atoms, observed mass distribution follow a polynomial decay with cluster size

$$Y_n \propto n^{-\alpha} \quad (2.34)$$

The exponent α has been empirically found and molecular dynamic simulations are able to reproduce such a polynomial decay [99]. However, sputter theory has not come up with a quantitative argument to explain this experimental evidence. Dimers are the most abundant cluster species sputtered. Originally, it was thought that dimers form upon sputtering from an elemental target when two atoms are sputtered independently and combine to form a cluster in the vicinity of the surface. Such a model is actually not in good agreement with some experiments, that would prove that clusters do not originate from independent emission events [99]. From molecular-dynamics simulation, it has been found that the majority of sputtered clusters have been nearest-neighbours in the target before sputtering. Simulation may be used to solve the question of when the two atoms which are eventually sputtered as a dimer were initially bound in the target.

2.4 Secondary ion formation

Secondary ion formation is greatly influenced by electron (or cation) exchange processes between the emitted species from the bombarded target surface. Thus, as already mentioned, the electronic state of the surface plays a crucial role. The yield of elemental secondary ions can vary by several orders of magnitude across the chemical period table, as shown in Figure 2.6, and is also strongly dependent on the chemical state of the surface.

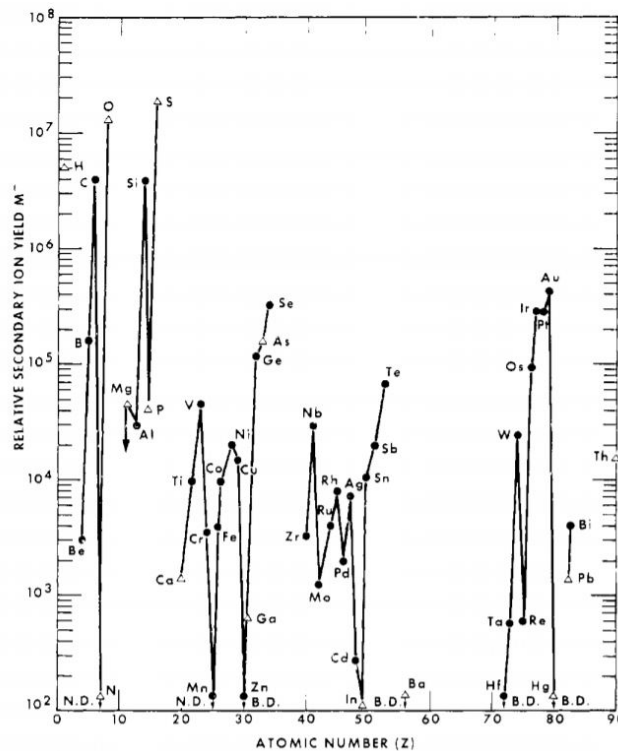


Figure 2.6: Variation of elemental negative secondary ion yield as a function of atomic number for bombardment by Cs^+ at 16.5 keV [100].

Generally speaking, the ion formation, at the base of SIMS working principle, is an extremely complex phenomenon. The ionisation process is less tractable than the sputtering process from a theoretical point of view. For this reason, the dynamic emission of atoms and multi-atomic clusters from a bombarded surface, and their ionisation mechanism are treated separately. In this section, a few of the main theoretical approaches to secondary ion formation are briefly outlined.

The fraction of sputtered particles that are in the ionised state is actually very small. In most cases, over 99 % of the sputtered species are neutral. Whether a sputtered particle escapes from the target surface as an ion depends on the relative probabilities of ionisation and de-excitation as it passes through the near-surface region. Consequently, the ion yield depends on the electronic properties of the matrix (the so-called matrix effect). In metals, the electronic transition is very rapid ($10^{14} - 10^{16} \text{ s}^{-1}$), hence the de-excitation is a high probability-event, during the 10^{-13} s required for a sputtered particle to traverse the near-surface region. The probability of escape as an ion from a metal can be approximated by

$$P \approx \frac{2}{\pi \hbar} \frac{e^{-\pi(\varepsilon_a - \varepsilon_F)}}{\gamma_N v} \quad (2.35)$$

where ε_a and ε_F are the energies of the ionised state and the Fermi level, respectively; v is the velocity of the emerging atom and $1/\gamma_N$ is the distance over which the level width decreases to $1/2.781$ of the bulk value.

However, it is necessary to take also in account the "molecular" covalent type of bonding for more complex samples. Moreover, the ionisation may take place at emission but also by subsequent fragmentation of vibrationally excited molecular units.

Bombardment of an inorganic solid with a low dose of keV primary ions generates singly-charged atomic ions, small cluster ions and a variety of so-called structural ions. The latter ones are of particular interest for molecular speciation in the mass spectra. Atomic ions are ionised elements, cluster ions are small polyatomic secondary ions that may originate from the recombination of atoms from non-adjacent positions in the sample. These ions are considered as being non-structural in nature. The term molecular ions only refers to ions that correspond to the intact molecule after removal of one electron. Adduct ions involve the attachment of an atomic ion or a stable cluster ion to one or several neutral molecules. Monomeric adducts include only one molecule, and polymeric adducts consist of several ones. Fragment ions are ions that are generated from molecular or adduct ions by structure-specific fragmentation mechanisms. Hence, fragments provide supporting information to direct speciation. In spite of numerous studies, it is still not yet entirely clear how the impact of a keV projectile finally leads to the detected ions. As previously described, the interaction of a primary ion with the solid introduces a wide range of complex processes, involving deposition of the projectile energy into the sample lattice, dissipation and recoil of that energy to the surface, sputtering and formation of ions. The experimental access to a single step in this sequence is difficult because the variation of one parameter tends to affect the other steps as well. As a result, different concepts on ion formation have been developed.

There are two qualitative models that are helpful in providing suggestive frameworks to describe the process of secondary ion generation from molecular species:

Nascent ion molecule model This model due to Gerhard and Plog [101], considered cluster ion formation primarily from oxide surfaces. It was suggested that the rapid electronic transition rates, which occur in the surface region, will neutralise any ions before they can escape. Secondary ions are a consequence of dissociation of sputtered

neutral molecular species at a certain distance from the surface. In the terminology of the model, ions are formed by the non-adiabatic dissociation of nascent ion molecules (neutral molecules). Only a few molecules have enough internal energy to dissociate into their constituents. The dissociation is considered to take place at a distance from the surface where the electronic influence of the surface will be much smaller. These ideas were further developed into the Valence Model. Empirically, this approach has had some success. However, it is highly unlikely that, even before sputtering, inorganic oxides can be regarded as purely ionic solids and, in addition, the charge can not be conserved when the bonds are broken during sputtering. A development of the Valence Model takes this into account and demonstrates that the static SIMS data suggested partial charges on the cations and anions which deviate from the pure ionic values. It is clear that, while the idea that the emission and fragmentation of nascent ion molecules is a major process, is straight-forward, and may deliver helpful results, nevertheless the details may be misleading.

Desorption ionisation model The desorption ionisation model due to Cooks and Busch [102] introduces the concept that vibrational excitation may be important in understanding the emission of cluster or molecular ions from organic materials. The final, not quite definitive, intuition is that a wide variety of ion emission processes are possible in not elemental targets.

3 Secondary ions detection and analysis

As widely described until now, SIMS is based on the information carried by atomic and molecular secondary ions, emitted from any surface under primary bombardment. Charge-to-mass ratios analysis of the secondary ions supplies direct information on the chemical composition of the uppermost monolayer of the bombarded surface area. So far we have seen that such information is conditioned by the total amount of the material available for the analysis and the efficiency of the ionisation process during the sputtering, but a crucial role is also played by the quality of the mass spectrometer used for the secondary ion analysis. The quality of the mass analyser is determined by the transmission, the mass resolution, the accessible mass range, and the mode of mass registration (sequential or parallel). Obviously, for progress in SIMS analytical applications, as well as in fundamental research, the continuous improvement of instrumentation has been an essential requirement. Today, SIMS is considered one of the most powerful techniques for surface and low-dimensional systems analysis. Features like the detection of all elements, including hydrogen, the isotope sensitivity, molecular information, and the low detection limit, are not also found to the same extent in other techniques for surface analysis (i.e., Photoelectron spectroscopy (XPS) and Auger electron spectroscopy (AES)). In the early years, the SIMS application was seriously limited by the performance of instrumentation. The experimental observation that low-dose SIMS could be used as a surface-sensitive technique was first made by Benninghoven [103,104]. Those results showed that many of the components present in the uppermost monolayer of the investigated samples were sputtered with useful yields, which were sufficiently high to generate useful spectra from such a layer. The low-current density analysis mode is called static SIMS and it is considered non-destructive as long as the primary ion fluence does not exceed the static limit of 10^{12} ions/cm², since the probability of the same target atom being bombarded twice is extremely low. In the static limit, the primary ion beam dose must stay below the above-mentioned value in order to achieve SIMS

characterisation of a true, undamaged surface.

3.1 Time-of-flight (ToF) mass analysis

The ideal detection system for SIMS should allow to fully utilize the information contained in the analysed sample, hence permitting simultaneous detection of different masses. Time-of-Flight (ToF) analyser is the best candidate for this purpose. The basic principle of ToF detector, schematised in Figure 2.7, is the mass/charge ratio (m/z) separation of the secondary ions that, under the effect of an electric field, acquire fixed kinetic energy and travel through a drift region of a known length (L), with a certain velocity.

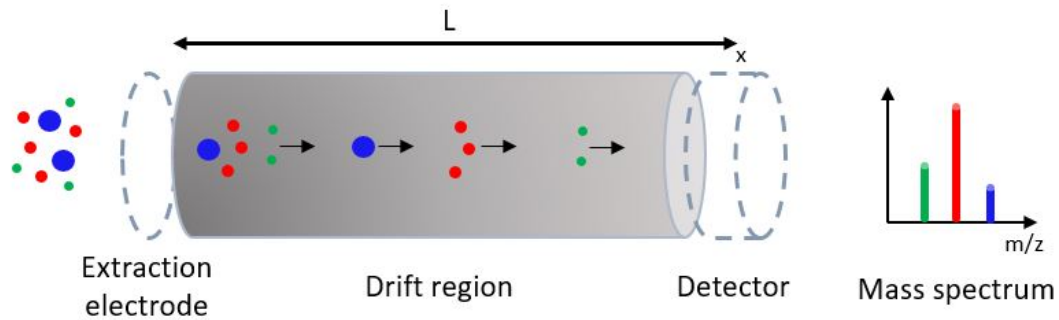


Figure 2.7: Working principle of a linear Time-of-Flight detector.

For ions of a given kinetic energy $e \cdot V = (m \cdot v^2)/2$, where e is the elementary charge, V the electric potential and v the velocity, a magnetic field \mathbf{B} acts as a momentum analyser exerting a deflection through the force $e \cdot (v \times \mathbf{B})$. The mass separation is achieved by a spatial dispersion of the ions almost orthogonal to the main trajectory (in the detector plane). The equivalent field-free path of ToF analyser is a drift region of length L . Travelling with an energy of $z \cdot e \cdot V$, the flight time of the ions to the detector is

$$\text{ToF} = \frac{L}{v} = L \cdot \sqrt{\frac{m}{2 \cdot z \cdot e \cdot V}} \quad (2.36)$$

where $z \cdot e$ stands for the ionic charge state, V is the potential applied to the secondary ions, by an electrostatic extraction section, before entering the field-free section with the same nominal kinetic energy, and v is the velocity of the specific ion.

Mass separation takes place along the spectrometer axis. In ToF-SIMS, the keV-primary ions are generated in very short pulses and, when the primary ion beam strikes the sample, all the secondary ions, (almost) instantaneously emitted, can reach the detector within the pulse length (typically from 100 to 10 ns). The pulsing of the primary ion beam gives the start signal for the time measurements.

Since $\text{ToF} \sim m^{1/2}$, the ToF analyser can, in principle, detect the complete mass range of sample ions in a single event and without specific tuning. The mass calibration can be reduced to the very simple form [105]:

$$T = A + B \cdot \sqrt{m} \quad (2.37)$$

where T is the flight time through the drift region to the detector, and A and B are constants from a least-square fit, carried out using known calibration peaks of a ToF spectrum. The electronic delays in the time measurement, and the time correlation between the start signal and the actual arrival time of the primary species on the sample, are contained in the constant A . In general, the start signal must be correlated to the

primary ion gun pulse as well as possible.

The basic *linear* ToF system in Figure 2.7, with its capability of parallel ion detection, is nominally able to detect all ion masses of a given polarity which are emitted from the sample because ions of different mass will arrive at the detector sequentially. Contrary to magnetic spectrometers, in an electrostatic ToF system, the mass separation is only along the spectrometer axis and no mass tuning is necessary. However, some practical limits influence parallel detection capabilities and the ToF mass spectrum resolution. First of all, a ToF mass analyser needs a very high-performance electronic system. Time-to-digital converters (TDC), in conjunction with pulse counting detectors, are capable in modern ToF-SIMS instruments of detecting 10^3 secondary ions per primary ion pulse. It is indeed possible to register all secondary ions with different nominal mass, as long as the dead time of the detection system is sufficiently small (i.e. 5 ns). The intensity of a certain mass could be, for example, underestimated, if several ions of the same mass are generated by one primary ion pulse and the counting system register their arrival as one event. The probability of having two ions of the same mass at the detector simultaneously depends on the average count rate of the ion species and the repetition rate of the primary ion gun. Statistical corrections can be applied to the mass spectrum, in order to mitigate this effect, but it is in general advisable to maintain under control the operating condition for a relatively small discrimination probability due to count rate.

The celerity of ToF-SIMS analysis is subordinate to the mass range of interest. As seen in Equation 2.36, the flight time is proportional to the length of the spectrometer and to $m^{1/2}$, for given secondary ion energy. For a certain number of primary ions per pulse, the count rate is proportional to the primary ion gun repetition rate, whose maximum permissible value is the inverse of the flight time of the heaviest ion to be analysed, which depends on the mass range of interest. If only the low mass range (i.e. 1 - 300 a.m.u.) is of analytical interest, precautions have to be taken to avoid the heavier ions, emitted through the first primary ion pulse impact, to be registered at the time set by the subsequent primary ion pulse. This situation, called mass wrap-around [105], leads to spurious peaks in the mass spectrum. Mass wrap-around is avoided by the implementation of a secondary ion blanking system for mass range selection of ions to be injected into the analyser. The ion blanking system allows also faster analysis time because the primary pulse repetition rate is defined by the mass spectral range of actual interest.

The mass resolution $m/\Delta m$ strongly influences the quality of the mass spectrum. The basic concept is that it is possible to separate two adjacent masses m_0 and $m_0 + \Delta m = m_0(1 + \gamma)$ in the mass spectrum only if their arrival-time difference Δt at the detector is "sufficient". In first approximation (if γ is small), mass and time resolution relation is:

$$\frac{m}{\Delta m} = \frac{t_0}{2 \cdot \Delta t} = \frac{1}{\gamma} \quad (2.38)$$

The smallest time width of a mass signal is given by the length of the primary ion pulse Δt_0 . The mass resolution improves as the ion flight time increases, so with the spectrometer length L or the ion mass. At low masses, the resolution is largely affected by the width of the primary ion pulse and the detection timing system speed. At high masses, the voltage stability and the detector play a more crucial role in mass resolution improvement. The major source of resolution degradation in a linear ToF analyser is the starting energy spread (ΔE) of ions of the same mass. Secondary ions are emitted with more or less broad energy distribution. Such initial energy spread is some eV for organic molecules and tens of eV for atomic secondary ions. In a linear ToF, the initial

energy distribution for ions of the same mass will intrinsically cause a broadening of the ion packet traveling from the sample to the detector [106]. The width of the secondary ion packet increases as the flight time/path increases, therefore a longer flight path does not actually improve mass resolution.

It is possible to define the total secondary ion energy E in terms of the nominal kinetic energy $E_0 = eV_0$ and the energy spread ΔE :

$$E = E_0 \cdot \left(1 + \frac{\Delta E}{E_0}\right) = E_0 \cdot (1 + \delta) \quad (2.39)$$

In first order approximation ($\delta \ll 1$), the flight time error, caused by the energy spread, leads to mass resolution definition:

$$\frac{m}{\Delta m} = \frac{E_0}{\Delta E} \quad (2.40)$$

The just mentioned approximation means that an ion with energy higher δ than some "average" will travel through the drift path L_0 when, at the same time, a reference ion will have only travel the distance $L_0 - (L_0/2) \cdot \delta$.

A possible solution to this problem could be to increase of a distance $(L_0/2)\delta$ the flight section of high-energy ions, hence the idea of using an ion mirror [107].

The ion mirror utilises an electrostatic field to reflect secondary ions, in order to provide positive time dispersion, i.e. to increase the flight path of high energy ions with respect to the lower energy ions. Regarding the scheme in Figure 2.8b, with a parabolic axial potential distribution $U(x) \sim x^2$ inside the ion mirror, and with ion source and detector located at $x = 0$, the time that the secondary ions will take to stop and accelerate again before they leave the field is [108]:

$$t = 2\sqrt{\frac{m}{2}} \int_0^{x_{\max}} \frac{dx}{\sqrt{E_0 - zU(x)}} \quad (2.41)$$

E_0 is the initial kinetic energy and x_{\max} is the distance ($\sqrt{E_0/k}$), needed to stop the ions. Then, the resulting flight time for secondary ions simply reduces to

$$t = \pi \sqrt{\frac{m}{2 \cdot z \cdot k}} \quad (2.42)$$

which is completely independent of the initial secondary ion kinetic energy and its spread.

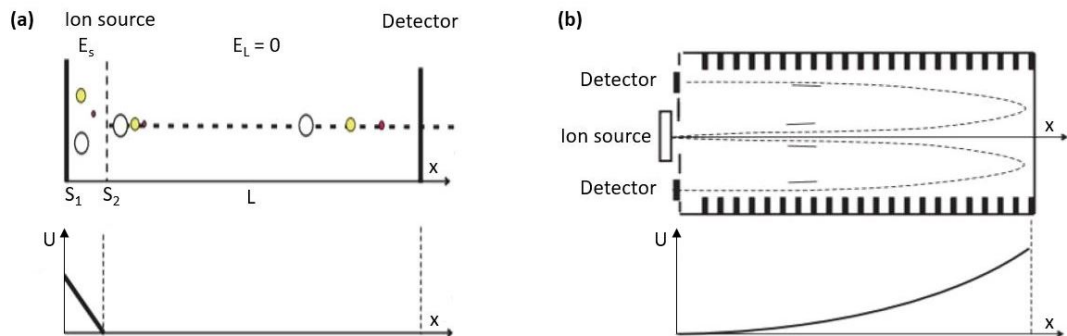


Figure 2.8: Linear (a) and quadratic field ion mirror (b) designs for ToF analyser. For both schemes, top: ions path and mirror positioning, bottom: potential curves. Figure reproduced from [107].

However, experimental implementation of such an ion mirror is not achievable for a ToF-SIMS mass spectrometer [107]. As mentioned above, this solution requires the source and detector position to be at $x = 0$, but this does not provide any access for the primary ion beams or focusing system to the sample.

Two much more suitable and adopted solutions are the single-stage and two-stage reflectron designs [105], shown in Figure 2.9. The single-stage reflectron system (Figure 2.9a) consists of a field-free drift region l_1 , a homogeneous retarding mirror field of length h_r and a second drift region l_2 from the mirror to the detector. In order to reflect the secondary ions to the detector, the retarding potential $U_r \sim x$ of the mirror has to satisfy the relation $e \cdot U_r \geq e \cdot U_0/5$, where $e \cdot U_0$ is the nominal secondary ion energy. In such a system, ion mirror works as a low energy pass filter for secondary ions, i.e. all ions of energy $< e \cdot U_r$ are reflected towards the detector. At a given time, the higher energy ions will be further along the drift direction than the lower energy ions. Entering the mirror field, the secondary ions are slowed down, come to a stop and turn around to exit the mirror.

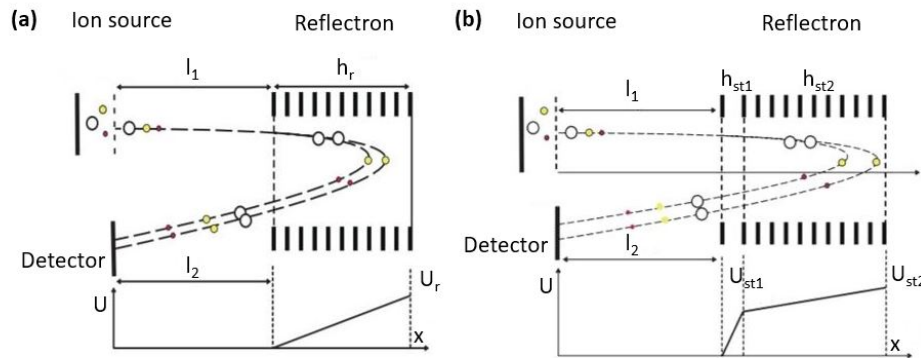


Figure 2.9: Single-stage (a) and two-stage (b) reflectron design for ToF analyser. For both schemes, top: ions path and mirror positioning, bottom: potential curves. Figure reproduced from [107]

Ions with higher kinetic energy will enter the mirror deeper than lower energy ions. At the reversing point, the high energy ions are trailing behind the low energy ions. The ions are then accelerated out of the mirror towards the detector, entering the drift region. High energy ions will close on low energy ions until they arrive simultaneously at the detector.

The general operation of two-stage reflectron system is schematized in Figure 2.9b. Analogously to the single-stage ion mirror, the two-stage operation is based on two drift section (l_1 and l_2). However, in this case, the mirror includes a strong homogeneous deceleration field (U_{st1}/h_{st1}), followed by a weaker field region (U_{st2}/h_{st2}). The basic principle of energy compensation through the trajectories elongation for high-energy ions, with respect to the low-energy ions and their position reversal at the reflection point, is the same as for the single-stage ion mirror. The only difference between the two designs in Figure 2.9 concerns the strong first deceleration section h_{st1} , through which the secondary ions penetrate the two-stage mirror less deeply. Therefore, a two-stage mirror can be smaller than a comparable single-stage mirror.

More in general, a ToF-SIMS spectrometer has a short acceleration section. The flight time errors introduced by the accelerating section have also second order terms. The time dispersion in the acceleration section is non-linear, for this reason the ion mirror cannot be operated under true nominal first-order energy focusing condition in order to obtain a mass resolution of $m/\Delta m \sim 10.000$. Mass resolutions of $m/\Delta m > 10.000$ are

obtained by adjusting the retarding mirror potential to linearly approximate the required parabolic energy compensation curve over a reasonable range on initial kinetic energies ($\delta = 0.0004$) [105]. The impact of the flight time dispersion for the single-stage and two-stage reflectron systems is the same. On both cases, in order to get high mass resolution in SIMS, the mirror fields are tuned to approximate the required curve for energy compensation. It is also true that no matter how well the analyser can match the required energy compensation behaviour, a very short accelerating (few mm) section should be used to minimise the error.

Delayed extraction and post-acceleration voltages are two other possible examples of design strategies for the ToF resolution improvement.

4 Analysis beams of ToF-SIMS

In ToF-SIMS instruments the incident beam, which impinges on the target surface, is pulsed. The secondary ions, which are also ejected in pulses, are then accelerated by the ToF extractor to enter the flight tube of the analyser.

The incident beam was commonly called "primary" ion beam, while the beam of ions from the sample is referred as "secondary" ion beam. The development of configurations with two or more interlaced primary beam for dynamic SIMS experiments, requires to distinguish the primary ions into "analysis beam" and "etching beam".

For conventional ToF-SIMS applications, the key properties of an ion source are:

1. Pulse duration of the beam
2. Kind of ions contained in the beam
3. Brightness of the beam
4. Energy spread of ions in the beam

These properties impact on some crucial experimental requirements, summarised as follows: **(i)** the beam must be pulsed such that the pulse duration does not reduce mass resolution; **(ii)** the kind of ions, i.e., primary ions-target interaction, affects the secondary ion yield and the degree of fragmentation, which must be not excessive and with surface damage degree within acceptable limits; **(iii)** the brightness influences the spot-size performance of the beam and the current density than can be achieved at the target. The spot must be small and stable to give sufficient lateral resolution; **(iv)** energy spread could causes chromatic aberration and increases the final spot size, because the focal length of an electrostatic lens depends on the ion energy. It is also necessary to pay attention to the beam scan rate of the sample, and to the source and column operation reliability and reproducibility.

The ion sources chosen as analysis and etching beams, in this thesis work, are described in the first part of this section, then some principal sources used in major and most recent ToF-SIMS instruments are briefly reported.

4.1 Liquid metal ion sources (LMIS)

When a flat liquid metal surface is exposed to a high electrostatic field, the equilibrium between the surface tension of the liquid and the impressed electrostatic force determines the formation of shaped protrusions (cones) [109]. Field evaporation of singly charged ions from the tip of such cone, known as Taylor cone, may occur when the

electrostatic field strength exceeds a specific critical value. The use of liquid metal ion sources (LMIS) as primary ion gun in ToF-SIMS is based on the above-mentioned evidence. The LMIS can emit singly charged monoatomic ion and also multiple charged cluster. The common assembly of a LMIS is shown in Figure 2.10. The heater filament is fixed to two support legs, which serves as electrical contacts and they are set on an insulating disc. The reservoir and needle are welded to the filament and they are coated with the chosen metal. The source, here in place with an annular electrode close to the tip of the needle, is normally placed on an insulating mounting inside the ion gun housing and is connected to a positive high-voltage supply. With an extractor potential value in the range of -5 kV to -10 kV relative to the source, a strong electric field is set up around the needle tip. Positive metal ions near to the tip move forward, while electrons move back down the needle because of the electrostatic force. This led to the formation of the Taylor cone and, when the source moves into a state of dynamic equilibrium, ion emission can start from the cone apex with a constant flow of ion current. The emission point is as small as 10 nm in diameter.

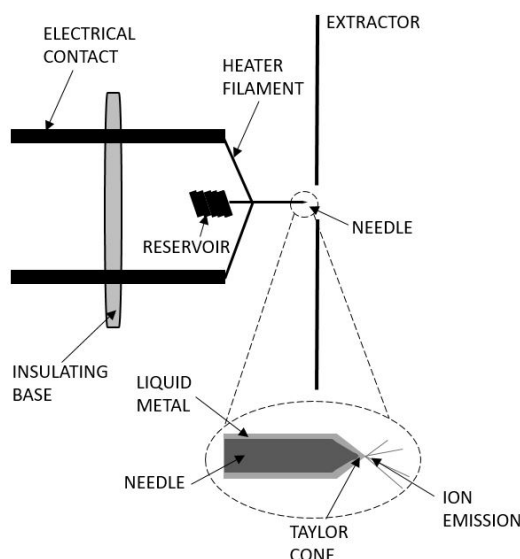


Figure 2.10: Schematic of liquid metal ion source.

Gallium was for many years the most used choice for LMIS, because of its favourable properties such as its low melting point (29.8°C). However, in the last twenty years, heavier atomic primary ions, like gold and bismuth, was recognised as better materials for superior secondary ions yields. Au_n^+ and Bi_n^+ small cluster ion beam have become the standard analysis beams on most ToF-SIMS instruments.

LMISs offer a wide range of useful properties for a good ion source: stability, consistency in operation and pretty simple servicing. Among all the ion sources, it is the brightest, providing the highest current density and the smallest spot size for ToF-SIMS apparatus. The ion beam from this type of source is also easily adaptable in terms of mass filtering, pulsing, scanning and focusing. The only disadvantages of LMIS are that it is limited to the generation of metal cluster beam of few atoms per cluster and also its tendency to damage the underlying chemical structure. The latter feature forces to use it only up to an ion dose limit, before the target is excessively damaged by metal clusters which sputter the surface layers. In order to overcome this limitation, beam interlacing technique has been developed, where the cluster LMIS alternate with a less damaging large cluster beam.

4.2 Surface ionisation sources

Many ToF instruments are equipped with cesium (Cs^+) gun, whose emission comes from a surface ionization source. Surface ionisation of a particle of a given energy E_i , which is adsorbed at a metal surface with a given work function ϕ , is based on electron exchange between the top of the conduction band of the metal and the ground state energy level of the adatom valence electron. This exchange is thermally stimulated if the adatom is equilibrated with the surface. At a certain temperature, the ratio between positive ions and neutral particles j^+/j^0 , vaporizing from a surface element, depends on the equilibrium occupation density (Maxwell distribution of the electron in a metal). In thermal equilibrium, the flux density \bar{v} of particles supplied to the surface must be equal to the total rate of vaporizing ions and neutrals, $j^+ + j^0$. When the surface coverage of adatoms is small, it is possible to find the maximum ion current density which can be drawn from the surface through the Saha-Langmuir equation [76]:

$$j^+ = \bar{v} \frac{j^+}{j^+ + j^0} = \bar{v} \frac{1}{1 + (g^+/g^0)e^{(E_i - \phi)/kT}} \quad (2.43)$$

where g^+/g^0 is the ground state statistical weights ratio. When the total evaporation rate $j^+ + j^0$ is increased above \bar{v} by an increase in temperature, the emission changes from a neutral-dominated to an ion-dominated regime. The transition temperature T_c (between 900 and 1200°C cesium on tungsten (W) is practically fully ionized) for surface ionization depends on the flux density \bar{v} . Above this transition temperature the current density of emitted ions is given by 2.43. At any value of T_c exists a maximum supply rate, for which an ion-dominated emission regime can be maintained. For the case $E_i > \phi$, (i.e., alkali metals as Cs on W), the maximum achievable current density j_{max}^+ is determined by equation 2.43. The current density which can be emitted by a surface depends also on the extraction geometry and the applied extraction field strength [76].

Generally in the Cs^+ source, cesium vapor from a heated reservoir is fed to a heated tungsten porous plug formed from sintered tungsten powder, typically 1 mm to 2 mm in diameter. The positive cesium ions are extracted from the surface of tungsten plug surface to an optical column.

Cesium bombardment dramatically increases negative secondary ion yields of electronegative elements, which are of great interest in semiconductor technology, and also of hydrogen, carbon, oxygen and the noble metals [110, 111]. Thermal ionized cesium ion source produce higher current than the LMIS type, but has lower brightness. The low energy spread (~ 0.2 eV) of such ion source offers the possibility of obtaining small spot sizes ($< 1\mu\text{m}$).

4.3 Other ion sources

Modern ToF-SIMS tools are often equipped with optical columns to which two different ion sources may be fitted. A typical example of dual-source ion column can contain a thermal sputtering ion source capable of producing Cs^+ and an electron impact source capable of producing C_{60}^+ . As mentioned in section 4.1, less damaging large cluster beam, such as C_{60}^+ and argon, can be interlaced to LMIS beam pulses in order to avoid sample damages during the measurements. As we will see in the next sections, the combination of a low-energy sputter beam with a high-energy, well-focused liquid metal ion gun (LMIG) is at the base of the so-called dual-beam experimental mode. In

such mode the first beam sputters a crater, the second beam progressively analyses the crater bottom (depth-profiling analysis).

Electron bombardment sources These sources are mainly used for the ionisation of gaseous clusters such C_{60}^+ and argon cluster. Ion sources using electron impact ionisation work, in practice, by supplying a source of electrons (typically a filament cathode), and a way to accelerate them to an energy sufficient to cause ionisation of the chosen material. C_{60} gas is usually generated in a small oven attached to the rear of the source by sublimation of C_{60} powder. Such sources are not inherently very bright and the extracted beam is less easy to focus compared with a LMIS beam. However, electron bombardment sources are very versatile for beams generation of a wide range of gaseous cluster ions.

Gas cluster sources Large (1000 - 3000 atoms per cluster) argon clusters sources have been recently developed for low-damage sputtering application on polymeric materials [112–114]. This type of source has two separate region for the cluster formation and the ionisation processes. Argon gas is fed at high pressure to a small aperture where the gas is subjected to an adiabatic expansion. Substantially, cooled argon atoms travelling co-axially at supersonic velocity condense to form the cluster. The second stage of the gas cluster source, where the ionisation take place, is based on the electron bombardment source operation as described in section 4.2.

Plasma sources This source type has originally found wide application as a high-current ion source in high-energy ion accelerators. The duoplasmatron is the main example of this family of sources. In a duoplasmatron a low voltage arc, burning between a cathode and an anode, is geometrically and magnetically confined by an opening in an intermediate electrode and anode, both made from magnetically soft material. The plasma is produced on the symmetry axis of the gap between anode and intermediate electrode. Ions are extracted from the plasma through a strong external electrostatic field. [76]. The duoplasmatron has higher brightness than an electron impact source, but lower than a LMIS. With sufficient beam energy, this source can bring good current density into a beam diameter up to 100 nm.

5 Instrumental setup

The ToF-SIMS instrument is installed at Roma Tre University (Surface Analysis Laboratory-INFN). The system is configured with a bismuth liquid metal ion gun (LMIG) as primary ion source, that can provide monoatomic or cluster Bi_n^+ beams at 30 keV. Furthermore, the system is equipped with a dual-source column designed to generate carbon cluster ions (C_{60}^+) and Cs^+ ions. In our instrumentation setup, Cs^+ source, ranging from 0.250 to 11 keV, can be used as etching beam for depth profiling measurements. The instrument also has an electron gun (flood gun) for charge compensation of insulating samples. The cesium and bismuth guns are positioned at $\pi/4$ to the surface of the sample holder in the analysis chamber, that is maintained at ultra-high vacuum pressure of 10^{-9} mbar with a turbo-molecular pump and a titanium sublimation cryogenic pump (in Figure 2.11, a scheme of the main components of the TOF.SIMS V equipment). Before being inserted in the analysis chamber, the samples are kept in a load lock chamber, maintained at 10^{-7} mbar. The sample transfer from the load lock to the main chamber takes place via a gate plate and an external arm fixed to the sample holder.

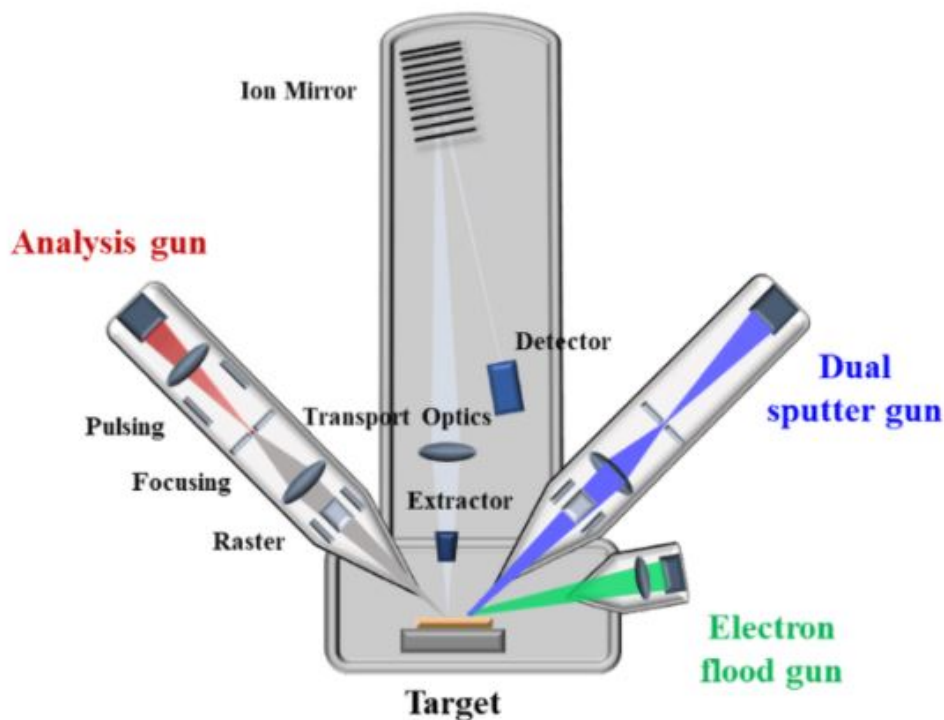


Figure 2.11: Schematic of the TOF.SIMS V analysis chamber, with ion beam columns, electron flood gun and mass analyser.

5.1 Analyser

In between the two guns in the analysis chamber, there is a reflectron type ToF mass analyser, already described in Section 3.1. The secondary ions (SI) from the bombarded target enter the analyser through the extractor electrode (usually with a voltage of 2 kV) and are subsequently focused in the flight tube. Before hitting the multi-channel plate of the detector, the SI pass the reflectron ion mirror and the post acceleration unit that increase the signal conversion rate in the scintillator (see Figure 2.12). The energy focusing usage of reflectron has already been described in Section 3.1. After the SI have left the reflector, they all have their initial kinetic energy and the higher energetic secondary ions overtake the slower ones (with shorter path in the reflector) at a certain point. The spectrometer is designed in such a way that this point is on the multi-channel plate. The detector convert an impacting secondary ion into a processable digital signal. A sufficient conversion of secondary ions into electrons is ensured by the post accelerator unit, typically sets with a voltage 10 kV. The electron emitted from the microchannel plate (MCP) after the impact of the secondary ions, are then accelerated toward a scintillator, converted into photons and detected by a photomultiplier. The photomultiplier signal is further processed to generate a trigger signal that is independent on the peak height. A time-to-digital converter then assigns these signals to a time scale with a resolution of 100 ps. Finally, the mass spectrum can be calculated. Several parameters can be tuned to optimise the analyser mass resolution, the most user-accessible are the distance of the extractor tip from the sample surface (typically 1.5 nm) and the reflectron voltage. The tip-target distance depends on the features of the analysed sample, the optimum reflectron voltage is 20 V for positive ions and -20 V for negative ions.

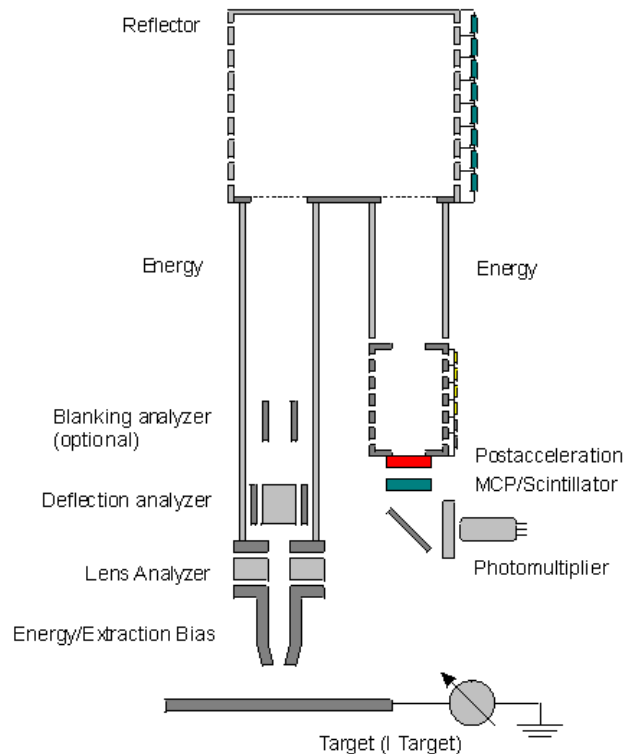


Figure 2.12: Schematic illustration with the main components of the TOF.SIMS V mass analyser setup. (Taken from IONTOF help manual).

5.2 Primary ion beam column

In Figure 2.13, the components of the primary ion column are schematised. The column starts with the LMIG bismuth emitter tip, the functioning of which is described in Section 4.1. The emitter potential defines the ion beam energy and the ion emission starts when the field strength, at the needle tip, exceeds a threshold value. The field strength is fixed by the extraction voltage, but for fine field adjustments and emission control the suppressor voltage should be used. LMIG column consists of three lens systems, respectively in order the lens source, lens magnification and lens target, to create an image of the source at the target. The alignment of the beam is achieved by the operator through two current measurement apertures (Ap. 1 and Ap. 2 in Figure 2.13). A deflection system X/Y is located in front of both apertures to center the beam through them. It is possible to measure the current across the two apertures to find the optimal focusing parameters. Similarly, the X/Y blanking deflection unit is used to align the beam through the blanking aperture, which is grounded inside the column. Therefore it is not possible to measure the current directly at this aperture, but the focusing through it can be optimised by measuring the current hitting the target, with a Faraday cup present on the sample holder or even a conducting sample. For all analysis modes, the primary ion beam must be pulsed. The beam pulsing is done by the pre-chopper and the chopper systems, that define the pulse width and select species of different masses with different velocities for the same energy beam (i.e., Bi^+ , Bi_3^+ etc..). The choice between monoatomic bismuth ions or small clusters is motivated by whether one needs to enhance the signal intensity or to preserve high mass intensities by decreasing the average energy per atom, respectively. Reducing the pulse length narrows the dispersion of the measured times of flight for fragments of the same mass and, consequently, it increases the mass resolution. Beyond the chopper, an axial bunching can be applied to the primary beam, in order to generate extremely short pulses of high current. This

improves considerably the mass resolution, but broadens the kinetic energy distribution of the ions inside a pulse, implying they are not deflected the same way inside the optical focusing system (chromatic aberration). The beam diameter is thus negatively affected, and the lateral resolution is degraded. For this reason, when high lateral accuracy is required, the buncher unit can not be used, implying that the mass resolution is reduced. Finally, at the end of the LMIG column, the lens target system focuses the beam on the target plane. The lens target voltage can be modified to minimise the beam spot diameter on the sample. Additionally, the X/Y-Stigmator unit can be used to compensate possible astigmatism effects.

The tuning of some components of the column allows the operator to switch from one operational mode to another one. For example, the lens magnification is used in the High Current Mode and in the Ultimate Imaging Mode in order to transmit the beam by a larger solid angle. In Fast Imaging Mode the lens magnification is switched off, since a smaller solid angle needs to be transmitted across the column. The burst blanker is used to generate a series of very short pulses in the Burst Mode.

In Table 6.2, an overview of the bismuth LMIG modes with nominal performances is sketched. The applications of the different operational modes for sample analysis will be described further down.

Mode	Spectrometry	High current Spectrometry	Fast Imaging	Burst	Ultimate Imaging
Description	High current, Highest mass resolution, Reduced lateral resolution.	Highest current, High mass resolution, Reduced lateral res.	Good current, High lateral resolution.	High mass res., High lat. res., Reduced current.	Highest lateral res., Reduced current.
Application	Surface spectrometry, Depth profiling, Mass resolved imaging with reduced lateral res.	Surface spec., Depth profiling, Mass resolved imaging with reduced lateral res.	Fast and high lateral res. imaging with unit mass res.	Surf. spec., High lateral res. imaging with high mass res.	Surface mapping with highest lat. res. and unit mass res.
DC Current target	> 30 nA	> 30 nA	> 400 pA	> 25 pA	> 50 pA
Spot size (Tip.)	< 5 μm	< 10 μm	< 150 nm	< 300 nm	< 100 nm

Table 2.1: Operational modes of the bismuth LMIG column in the TOF.SIMS V instrumentation, with nominally achieved performances and applications.

5.3 Dual-source column

In Figure 2.14, the dual-source ion column with the thermal ionisation cesium source, present in our instrumentation setup, is schematised. The working principles of the ionisation sources have already been outlined in Section 4.2. The dual-source column is a high current ion optical column, to which also an electron impact ion source may be fitted, as shown in Figure 2.14. The deflection units and the pulsing, focusing and bunching working principles are similar to those of the primary ion beam column. The suppressor, at the column top, defines the potential of the first electrode below the Cs emitter. If, for example, the suppressor voltage is 100 V and an ion energy of 10 kV is selected, the suppressor will have a potential of 9900 V with respect to the ground. The ion energy defines the potential of the ionisation chamber and the Cs-emitter. Since the target is on ground potential, the emitter voltage determines the impact energy of the

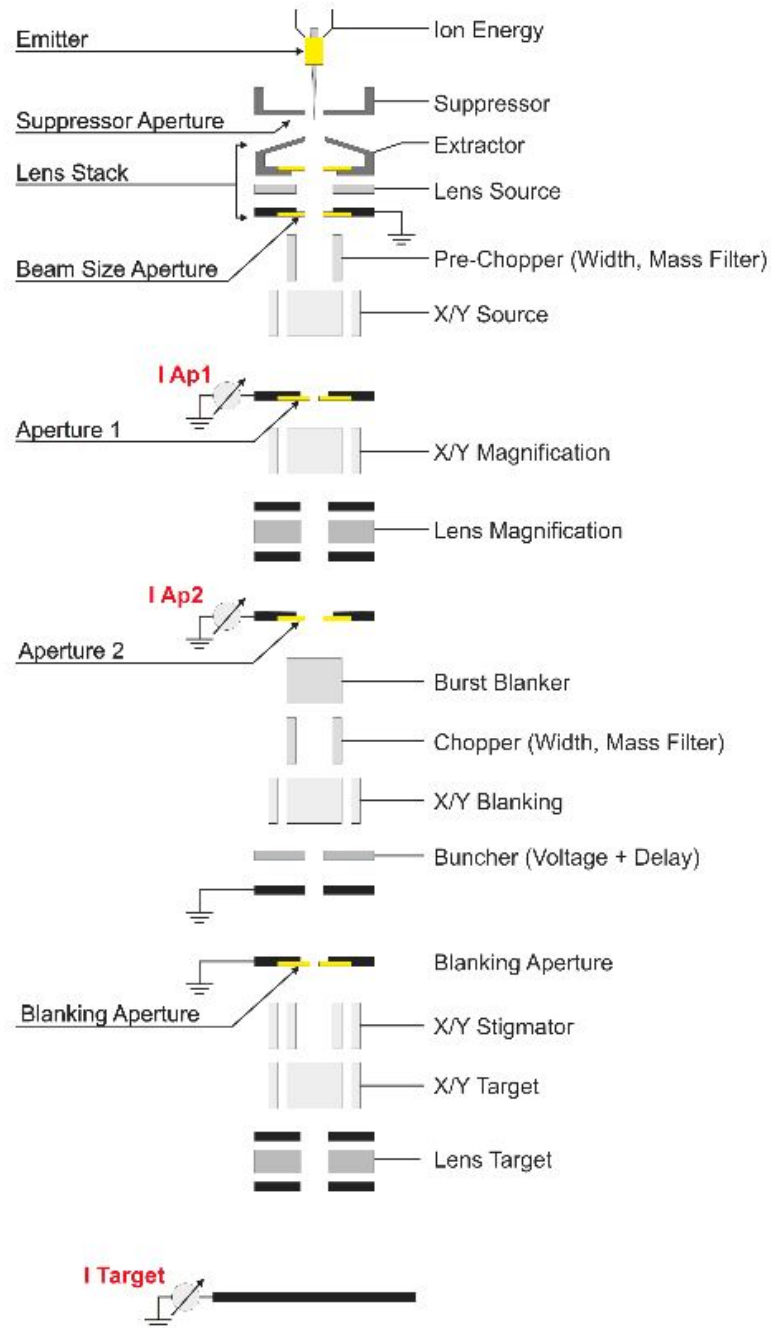


Figure 2.13: Schematic illustration of the components present in the primary ion beam column of the TOF.SIMS V. (Taken from IONTOF help manual).

primary ions on the sample.

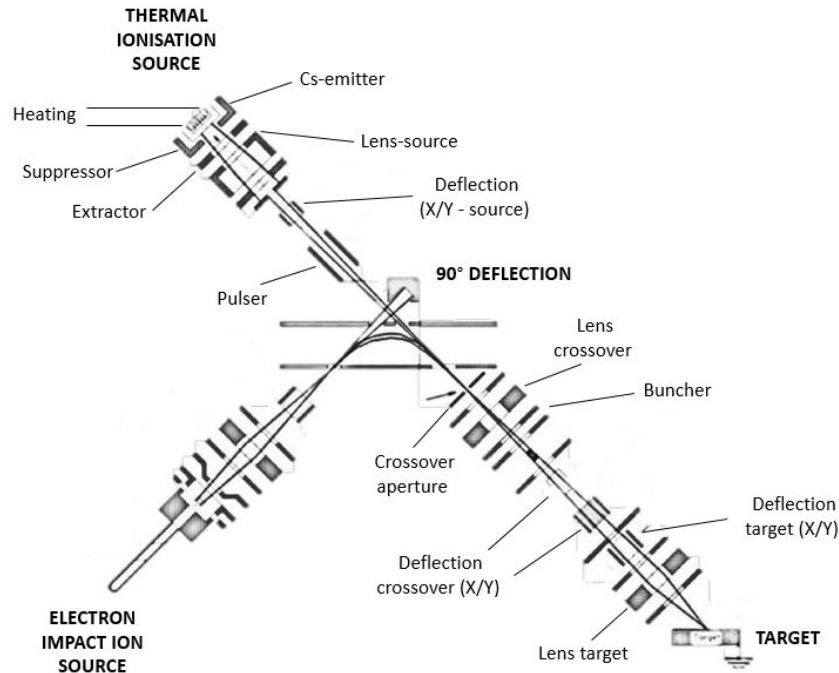


Figure 2.14: Schematic illustration of the components present in the dual-source ion column of the TOF-SIMS V. (Adapted from IONTOF help manual).

5.4 Electron flood gun

Surface of insulating samples can be easily electrostatically charged up by primary ions during the SIMS analysis, due to the electron emission. Such an effect may result in a reduction or in the complete loss of the secondary ions that reach the analyser, hence of the signal. The rise of localized positive sample charging may cause the change of the SI energy and the distortion of SI trajectories, because insulating materials are not characterised by enough electrical conductivity to carry the electrons to the charged regions. A possible strategy to compensate this issue may be the irradiation of the sample with electrons at sufficiently low energy to not cause any damage between the pulses of primary ions. For this purpose, our ToF-SIMS instrumentation is equipped with a low-energy (0-21 eV) electron gun. The energy of the electrons is determined by the potential of a filament shielded by an electrode. When the floodgun is turned on for charge compensation on an insulating sample, the reflectron voltage of the analyser must be changed because the sample surface potential shifts from the ground. In figure 2.15, the so-called adjustment of the virtual surface potential is illustrated. The change of the surface voltage V_S is corrected by the shifting of the reflectron voltage V_R by a quantity $\Delta U_{\text{surface}}$ (surface potential), which is not equal to zero for insulating target under ion bombardment.

6 ToF-SIMS analysis modes

For ToF-SIMS measurements, our instrumentation, described so far, is capable of raster scanning the primary ion beam with a maximum area of $500 \times 500 \mu\text{m}^2$. The analysed sample surface is, practically, divided into pixels. In all analysis modes, a full mass

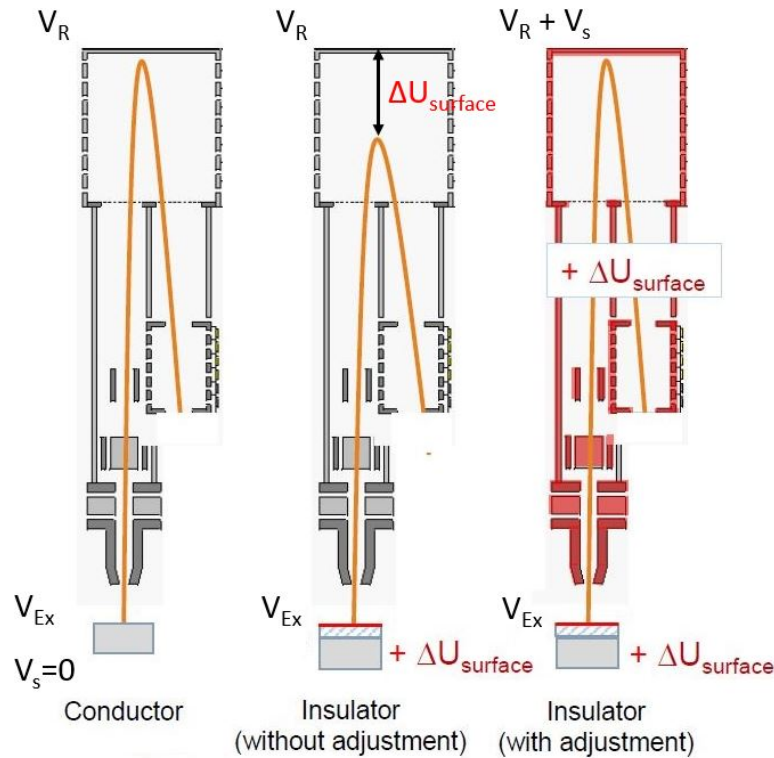


Figure 2.15: Adjustment of the reflector voltage (V_R) for insulating samples. V_{Ex} is the extractor voltage. (Adapted from IONTOF User's Training Course material).

spectrum is acquired and recorded, per pixel, in the raster pattern, enabling also the post-reconstruction of the data sets (Figure 2.17d).

6.1 Static SIMS

In a surface spectrometry experiment, one might simply be interested in the mass spectrum representative of the surface under analysis, and less in the spatial distribution of secondary ions (Figure 2.17a). However, in order to minimise sample damage, the beam is raster scanned over small areas and the spectra of all pixels are collapsed into one final representative mass spectrum. In such cases, there will always be a limit to the ion dose⁴ that can be used without significant damage to the sample structure or chemistry. In the so-called Static SIMS mode, which is considered as a quasi non-destructive mode, the primary ion dose has to remain below the threshold value of 10^{12} ions/cm². For all practical purposes, it indicates when analysis with a metal cluster beam must cease. An important factor, in calculation of the time to reach the static limit, is the duty cycle, defined as the ratio of beam-on time to "real time" of a pulsed ion beam, and determined by the duration of the ion beam pulses, and the repetition rate of pulsing. Just to give an example, if an unpulsed 1 nA beam scanned an area of $100 \times 100 \mu\text{m}^2$, it would deliver singly charged ions up to the static limit in just over 0.001 seconds. If the same beam is pulsed at 10 kHz with 10 ns pulse, such beam is actually on for only 10^{-4} seconds for each second of real time. Consequently, the pulsed beam takes over 100 seconds to reach the static limit. The duty cycle is experimentally constrained by the mass range, which limits the repetition rate, by the required mass

⁴The ion dose is usually defined as the total number of primary ions impacting on the sample per square centimetres.

resolution, closely coupled to the pulse length, and by the required spatial resolution, which defines the beam current. Given these parameters, and the analysis area, the time to reach the static limit can be calculated, it is given by:

$$T = \frac{A \times q \times 10^{30}}{I \times f \times t} \quad (2.44)$$

where q is the electronic charge (1.602×10^{-19} C), A is the analysis area in cm^2 , I is the current of singly charged ions in nA, the pulse length in ns is t , and the repetition rate f in Hz.

The generation of short primary ion pulses (< 1 ns) is the crucial requirement for high mass resolution in spectrometry surface analysis. Referring to the example given above, the time to reach the static limit increases to 1000 seconds with the pulse length at 1 ns. Among the LMIG operational modes (see Table 6.2), the high current (Bunched) mode is one of the most suitable for good mass resolution. Beyond the chopper, the buncher unit in the LMIG column (see Figure 2.13) consists of two plates, both grounded when the pulse enters the zone in between them (Figure 2.16a,b). When the pulsed beam goes exactly between the buncher plates, the rear plate is set to a positive voltage that accelerates the ions (Figure 2.16c). An ion which is passing the exit plate of the buncher as the pulse comes on will continue to the sample in a time t_1 :

$$t_1 = \frac{l}{\sqrt{\frac{2V_0q}{m}}} \quad (2.45)$$

where l is the distance to the sample, V_0 is the acceleration voltage of the column, q the charge, and m the mass. Another ion, at a distance x before the exit plate, would experience the acceleration through the potential V_x , produced by the pulse on the entrance plate. For this ion, the time t_2 from the exit plate to the sample is:

$$t_2 = \frac{l}{\sqrt{\frac{2(V_0+V_x)q}{m}}} \quad (2.46)$$

Both ions will arrive at the sample together if $t_1 - t_2 = t_x$, where t_x is the transit time from x to the exit plate. Such a condition can practically be obtained by introducing some field curvature, through buncher electrodes shaping, making the potential gradient steeper near the entrance than at the exit. The reduction of the pulse length, when the ion beam reaches the target (Figure 2.16d), leads typically to a compression from 20 ns raw pulse into less than 1 ns. As a consequence, the mass resolution is optimised ($m/\Delta m \sim 10000$), with high beam current (~ 30 nA DC on target). The buncher introduces an energy spread that results in serious chromatic aberration in the probe, therefore the lateral resolution is hugely reduced, i.e., 2-10 μm spot size, even when using a bright ion source.

As mentioned before, each pixel of the scanned sample area contains a spectrum. Such a local chemical information can be laterally mapped. In ToF instruments, spatial resolution as low as 0.1 μm is a routine expectation. The main determinants of the spatial resolution in the ion-optical column are the lenses, the apertures, the pulsing unit and the electrical supply to the column. Surface imaging ToF-SIMS measurements (Figure 2.17b) provide mass resolved secondary ion images (chemical maps), from the topmost atomic layers of the target, under the static limit. In order to achieve an adequate lateral resolution, the primary ions pulse has to be increased, hence the Bunched mode is not recommended. Fast Imaging and Ultimate Imaging analysis modes are the most suitable ways for high lateral resolution mapping, obtained with reasonable acquisition

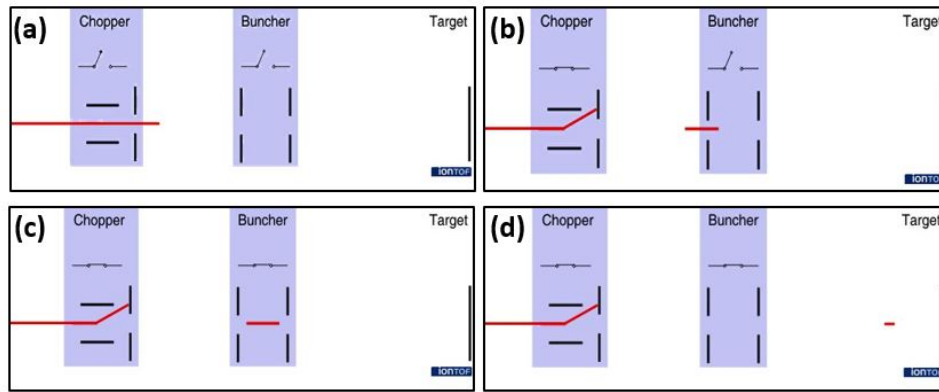


Figure 2.16: Bunching principle schematised in four steps (a)-(d). (Images adapted from IONTOF User's Training Course material).

time or for the best lateral resolution mapping, but with long acquisition time, respectively. The two just mentioned analysis modes are characterised by long pulse length (100-150 ns), spot sizes less than 150/100 nm but very limited mass resolution. The Burst analysis mode (in Table 6.2) can be instead considered a good trade-off between mass and lateral resolution. In this case, long no-bunched pulses are chopped into many short pulses, which result in repeated peaks for the same mass in the spectrum [115]. Such repeated pattern in the spectra may, however, be problematic when several peaks are present in the same nominal mass.

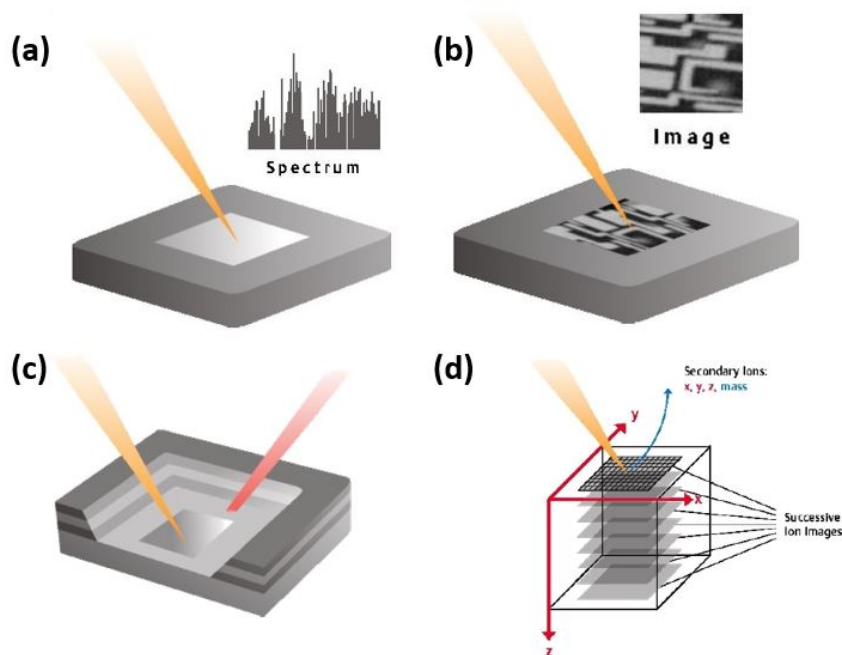


Figure 2.17: Analysis modes with ToF-SIMS. (a) Surface Spectrometry (static SIMS), (b) Surface Imaging (static SIMS), (c) Depth profiling, (d) in-plane (2D) and in-depth (3D) ToF-SIMS data set reconstruction. (Taken from IONTOF User's Training Course material).

In general, the best suited Imaging mode is determined by particular analytical requirements, like the lateral or mass resolution, but also like the measurement acquisition time or the dimensional scale of investigated system (field of view). The diagram in Figure 2.18 summarises all the experimental compromises, listed so far, to consider in

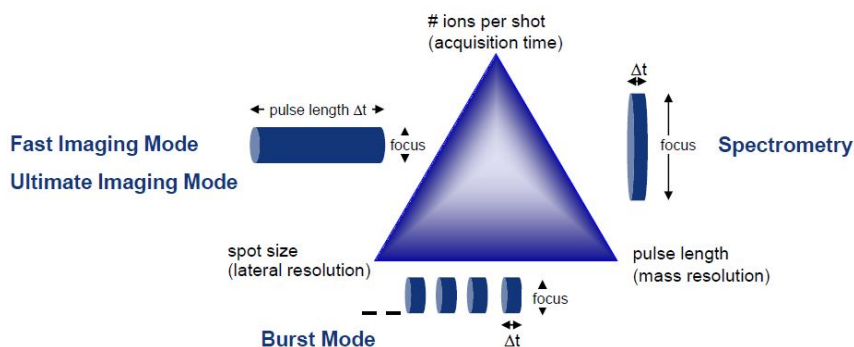


Figure 2.18: Trade-off scheme of static ToF-SIMS analysis modes. (Taken from IONTOF User's Training Course material).

choosing the most convenient Imaging analysis mode.

Another way to satisfy the double requirement of acceptable mass and lateral resolution is to essentially delay the extraction after the primary ions impact [116]. Generally, a pulsed quasi-static extraction is active as default extraction mode of the ToF analyser. In this case, the extraction takes place in while the secondary ions are generated and the Δm value depends on the primary pulse length. In panel (a) of Figure 2.19, the timing cycle of the quasi-static extraction mode is simply schematised.

In Delayed Extraction mode, the extraction is initially turned off while the SI are generated. In this way, the ejected matter forms a "cloud", in the space between the extractor and the target, that expands in the absence of an electric field (see panel (b) of Figure 2.19). Then, when the extractor voltage is turned on, the ions that are further away from the extractor undergo the effect of the acceleration, due to a higher potential difference, for a longer time than ions with a higher velocity that almost reach the analyzer column. In these conditions, the Δm value depends less on the pulse length, but a loss of signal transmission is observed, especially for low mass SI.

6.2 Dynamic SIMS: depth profiling

The in-depth analysis, i.e. investigation of the sub-surface sample regions (in Figure 2.17c,d), of the chemical composition of materials, as well as the interfaces characterization, is of major significance in many areas of research and technology. It is achieved, by using ion bombardment for the controlled erosion of the sample, in combination with surface analytical techniques, like Atomic Emission Spectroscopy (AES), or X-ray Photoelectron Spectroscopy (XPS). Usually, a focused ion beam, with energy up to some keV, is rastered over an area larger than the beam size, in order to shape a well-defined sputter crater with a flat bottom. While in electron spectroscopy the crater bottom analysis is performed by an independent excitation probe, in ToF-SIMS the sputtered particles themselves are used for the analysis. In-depth analysis is also called dynamic SIMS, in contrast to static SIMS, described in the previous section, for the analysis of the uppermost layer of a solid. In ToF-SIMS sputter depth profiling, the most relevant features are the detection limit, nominally in the sub-ppm⁵ range, an information depth⁶ (ID) of 1-2 monolayers, and the high speed of analysis [76].

For in-depth analysis the erosion gun is used alternately with the analysis gun. The

⁵Parts-per-million.

⁶The depth of information is defined as the distance below the surface of a specimen, from which information is contributed at a specific resolution.

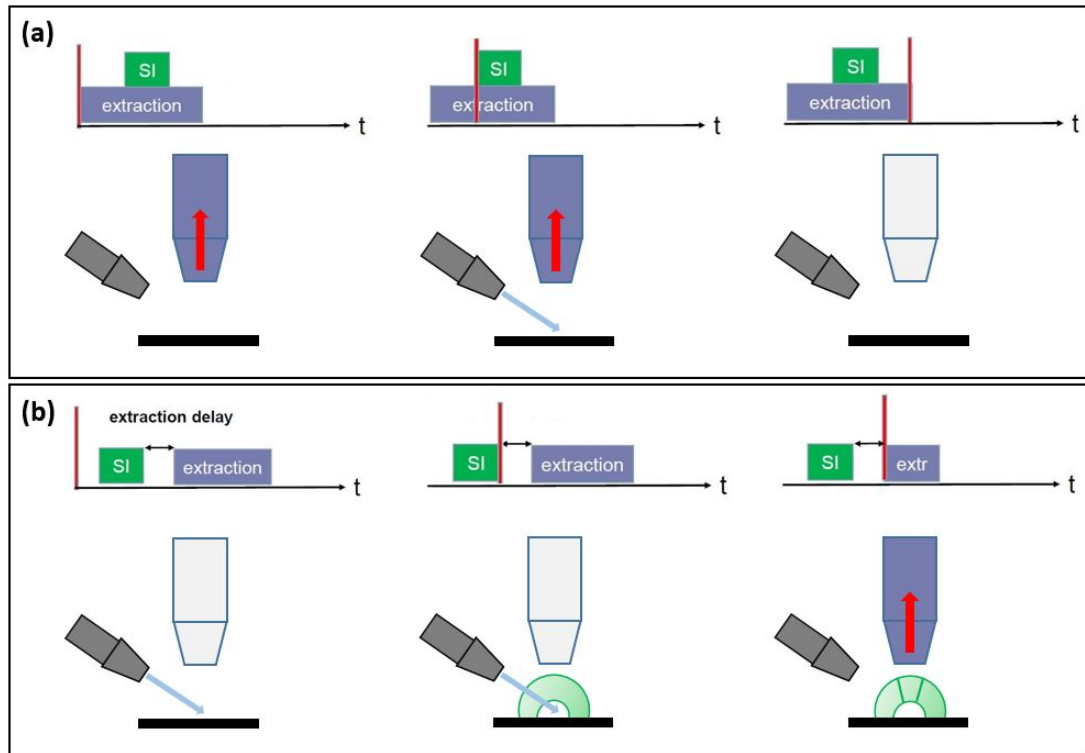


Figure 2.19: Schematic of (a) quasi-static extraction mode and (b) Delayed Extraction mode. (Adapted from IONTOF User's Training Course material).

basic principle of the depth profiling experiments is that the matter ejected during the sputtering process is not analyzed; during this phase, the previously rastered surface is removed and a *fresh* surface, deeper into the sample, is dug up for the next analysis cycle.

Alternating two different guns for the analysis and erosion phases, within one analysis cycle, corresponds to the so-called dual beam measurement mode. This mode offers some advantages:

- The pulsed beam for ToF detection allows the parallel detection of all fragments. Furthermore, the user can reconstruct results retrospectively.
- Despite very low currents employed for the pulsed analysis beam, high sputter yields are guaranteed by the erosion beam.
- The analysis and the sputter parameters can be adjusted independently, for example it is possible to exploit the combination of a low energy Cs^+ sputter beam, to increase the yield of secondary ions, with a high-energy, well-focused LMIG beam.
- Each beam can raster a different analysis area. This means that one can select a smaller area, avoiding the detection of fragments coming from the borders or defectives sample regions.
- A focused analysis beam, while the erosion beam is maintained de-focused, limits the bombarding-induced roughness in the sample.
- High lateral (2D/3D) resolution imaging is possible with highly focused analysis beams.

In dual beam mode, two different approaches, based on the adopted analysis time sequence, can be exploited: the Interlaced mode, where both beams are used quasi-simultaneously and the Non-interlaced mode, where the primary ion beam and analyser operate separately from the sputter gun, with intervals (order of seconds) that give time for surface relaxation and electron flooding, i.e. at least one analysis cycle is completed before the erosion gun is set on.

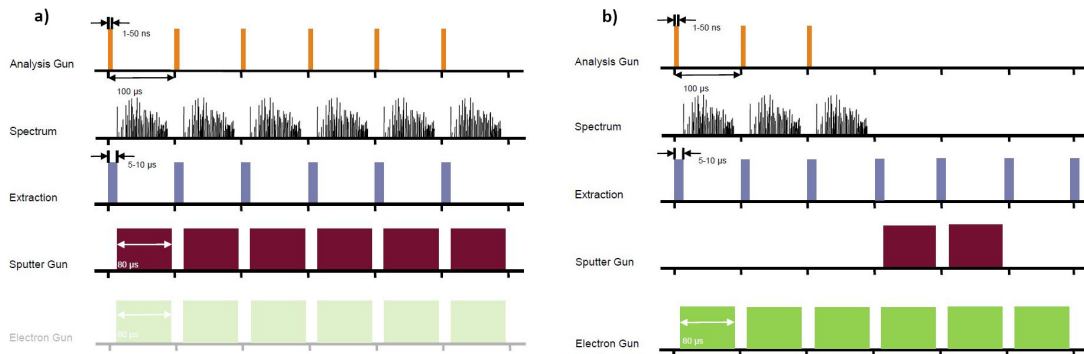


Figure 2.20: Schematic comparison between the time sequences of (a) Interlaced and (b) Non-interlaced modes of ToF-SIMS depth profiling analysis (Taken from IONTOF User's Training Course material).

The Interlaced mode is particularly recommended for the study of conducting samples, while the Non-interlaced mode is useful in the case of insulating samples, because it allows a longer charge compensation interval, since the flood gun is in use during the whole sputtering cycle. Interlaced mode furnishes higher acquisition data rates and optimal material erosion performances.

The main applications of depth profiling investigation are the 3D characterization of multilayer systems, interface phenomena probing, layer-by-layer compositional and structural analysis, and the atomic and molecular species migration checking inside sample bulk.

During a depth profiling experiment, many indicators, like the variation of material-dependent sputtering yields, the roughness before and after the analysis or the depth resolution, need to be taken into consideration to a reliable interpretation of the data.

The depth resolution describes the broadening of the measured intensity profile with respect to the depth distribution. Practically, it can be defined as the interval between 16% and 84% of the maximum intensity of the rising signal when crossing a planar interface [117]. Ultrathin delta layers are frequently used to investigate the various effects which can influence the depth resolution. In these delta layers studies, the obtained profile of the delta layer is a convolution of the ideal profile with a response function depicted in Figure 2.21. This response function, according to the Mixing-Roughness-Information (MRI) depth model [118], is a convolution between a growing exponential, accounting for the information depth, a Gaussian, characteristic of the interface natural or induced roughness and a decreasing exponential, that takes into account the atomic mixing length.

This last contribution might be considerable for inorganic shallow layers, while it is negligible in organic materials, given the large size of sputtered molecules. Such a response function can be described by three parameters, shown in Figure 2.21: the upslope λ_u and the decay length λ_d , i.e. the exponents of the two exponential functions, and the full width at half maximum (FWHM) σ , correlated to the Gaussian width. The MRI model relates these three parameters to sample and analysis properties. The decay

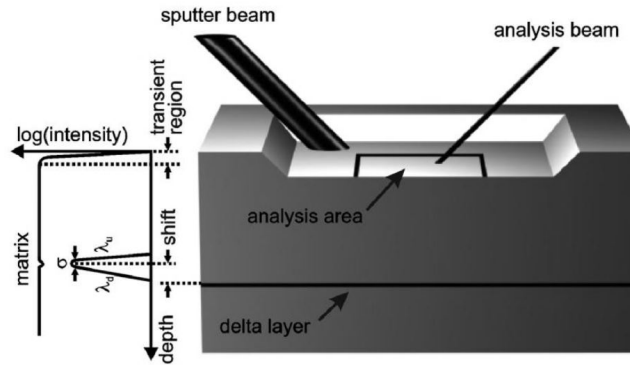


Figure 2.21: Response function of the delta layer for depth profiling resolution evaluation, according to the MRI model [118].

length λ_d is the parameter of the resolution function which is most strongly influenced by the experimental conditions, in particular the sputter energy. The atomic mixing, i.e. the relocation of atoms in the collision cascade, leads to a specific mixing length, resulting in the exponential decay λ_d . It follows that, if the depth resolution obtained in a certain experiment is to be compared with another one, the decay length, i.e. the depth interval over which the signal intensity decreases by a factor of $1/e$, is the most accurate parameter describing the impact of the experimental conditions on the depth resolution.

The ToF-SIMS in-depth information is recognised to have a less than one nanometer resolution [119]. A reasonable sputtering yield value is a key-parameter for achieving outstanding depth profile results for three major reasons:

1. Since the sputtering beam in the analysis cycle is supposed to remove the volume affected by beam-induced modifications from the previous cycle, generated by both analysis and erosion guns (Figure 2.22), a sufficiently high sputtering yield helps to avoid damage accumulation. Generally, the sputtered depth (measured or calculated, if the sputtering yield is known) must imperatively be more than half of the damaged depth (obtainable through simulations). It ensures that a fixed depth is not altered by two consecutive analysis cycles.

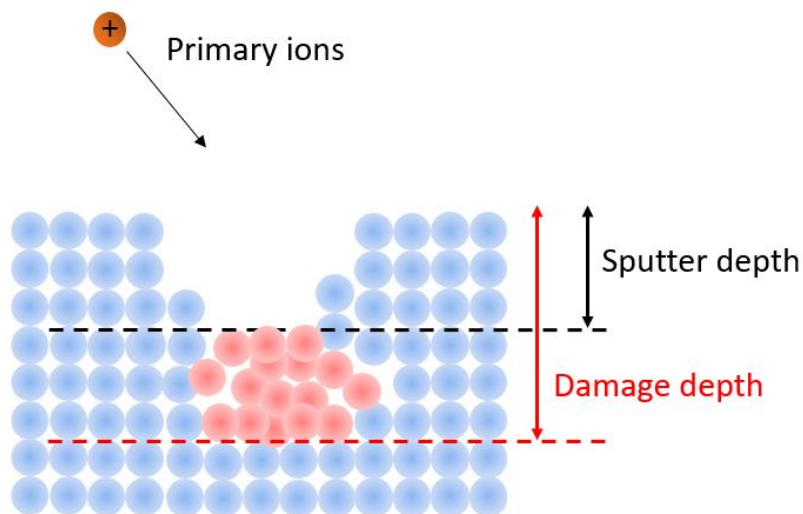


Figure 2.22: Comparison of sputtered and damaged depth after one analysis/sputtering cycle

The sputter rate⁷ ratio parameter, R , can be introduced to define whether the analysis beam-induced damage has to be taken into account. It is defined as the amount of atoms that are ejected by the sputtering beam, compared to the ones ejected by the analysis beam, expressed by the ratio between the sputter rates of the erosion and analysis beams, R_{sputter} and R_{analysis} [120].

$$R = \frac{R_{\text{sputter}}}{R_{\text{analysis}}} \propto \frac{I_{\text{sp}} Y_{\text{sp}} A_{\text{an}}}{I_{\text{an}} Y_{\text{an}} A_{\text{sp}}} \quad (2.47)$$

where I_{sp} and I_{an} are the currents of the erosion and analysis beams, respectively; Y_{sp} and Y_{an} their corresponding sputtering yields, and A_{sp} and A_{an} the raster areas chosen for the erosion and analysis beams, respectively (see in Figure 2.23). A value of 100 for the R parameter, means that that only 1% of the ejected atoms are sputtered by the analysis beam. In practice, a ratio in the range of few hundreds ensures a good profile quality, even if this value may strongly depend on the primary ions and sample features. The sputter rate ratio can be improved by reducing the primary ion current, by increasing the sputter current or the analysis raster size and by decreasing the sputter area size.

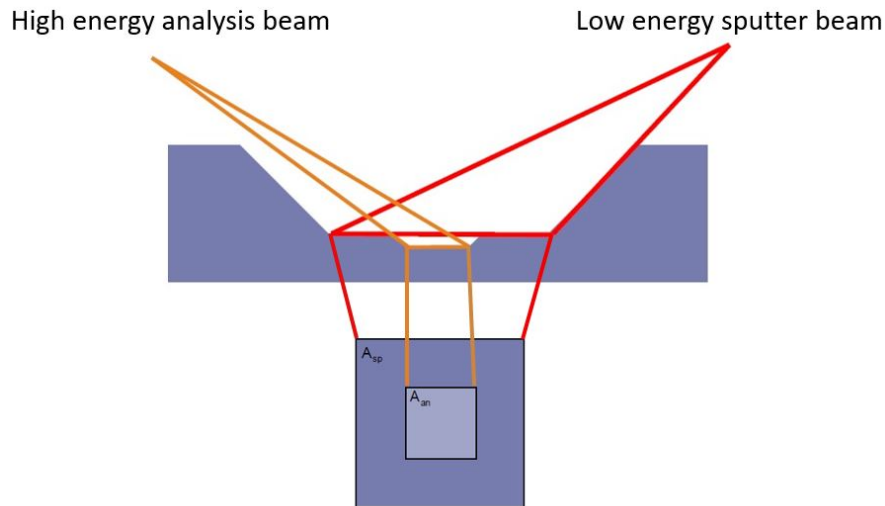


Figure 2.23: Analysis A_{an} and sputtering A_{sp} raster areas in ToF-SIMS dual beam experiments.

2. A variation of the sputtering yield inside a layer of the sample can denote ion beam degradation, typically by cross-linking or by preferential sputtering effects.
3. Differences in the sputtering yields along the sample can induce a certain number of artifacts.

The crucial goal is to minimise the side effects from the profiling process and leave the sample as “undisturbed“ as possible, with the aim of differentiate the intrinsic sample properties from the modifications induced by the measurements. Depth profiling is a destructive and highly perturbing analysis. The interactions of the ion beams with the surface can not be completely avoided, but can be limited, by choosing the energy and nature of the primary ions. This necessitates an accurate and rational choice of the analysis parameters and conditions, which should be adapted to the sample, being in such a way as “gentle” as possible.

⁷The Sputter rate parameter quantifies the sputtered material per unit time, it is usually expressed in nm/s.

6.2.1 Calibration of depth profiles

The successful interpretation of a depth profile needs the correct conversion of the obtained data from an intensity-time to a intensity-depth (or concentration-depth) profile. The first step is to establish a depth scale. It is usually made with the assumption that the sputter rate is constant during the whole profile, ignoring the fact that the sputter rate changes, at least in the transient region between the deposition and the erosion regime, described in Section 2.3.2. The sputter rate can be either determined by internal tracers, such as known interface positions, or calculated after measuring the crater depth by different surface profilometry techniques.

For the intensity to concentration conversion, the assumption of a concentration-independent ionisation is usually made. Under this assumption, and if variations in transmission of the spectrometer and sputter yield are neglected, the concentration $c(A)$ of the analyte A can be calculated according to

$$c(A) = \text{RSF}(A, M) \cdot \frac{I(A)}{I(M)} \quad (2.48)$$

where $I(A)$ and $I(M)$ are the detected intensities of the analyte and a matrix species. The Relative Sensitivity Factor, $\text{RSF}(A, M)$, is usually determined by a standard sample with the same analyte and matrix as the unknown sample.

Chapter 3

Exploring the effects of different projectiles with different energies

As pointed out in the previous chapter, the ToF-SIMS methodology is wide-ranging. The selection of primary ion sources and ion optical system for the analysis guns depends strongly on the kind of analysis that is required, and it can influence the type and the amount of material available for detection. The mechanism of secondary ion formation is, as already mentioned, hugely influenced by the interaction of the primary ion with the sample, and it can alter the analytical capabilities of the experiment, in particular, its imaging resolution and depth profiling skillfulness. As general rule, increasing the mass of the projectile results in increased secondary ion yield.

The static limit of $\sim 10^{12}$ ions per square centimeter, defined in Section 6.1, is valid for beams of atomic ions and small clusters. Larger clusters (e.g., C_{60}^+ or Ar_n^+) produce in general less damage below the sputtered volume; this comes from the fact that their energy is dissipated almost completely within the sputtered surface region. Roughly speaking, the cluster disintegrates on impact and the individual atoms from the cluster have too little energy to penetrate deeply into the surface. So, the ion dose of the static limit can often be several orders higher for this class of primary ion beam. Attempting to perform our analysis within the static limit, the maximum number of impacts on a HOPG surface portion of $1 \mu m^2$ is $\sim 10^4$. A metal primary ion beam typically generates a secondary ion yield of the order of $\sim 10^{-2}$ ions/atom; so it would result in 100 ions to detect, sufficient for quite meaningful data, if the sample chemistry is simple. In the system we investigated, we need to detect molecular species probably present at low concentration values, then this latter sputter yield value may not be sufficient. Large cluster beams can give a secondary ion yield close to unity, and that would make the 1% concentration detectable from a $1 \mu m^2$ area. Actually, we are interested in slightly larger dimensional scales, but there is always a limit to the amount of information that is available from a given area, defined by the sample chemistry, the secondary ion yield, and the efficiency of detection. This introduces a lower threshold on the pixel size that can be used in an imaging analysis.

In this thesis, we are in search of surface and depth information from the HOPG crystal, then the dual beam interlacing mode, described in Section 6.2, must be properly used. Some preliminary results, performed for the need to choose the experimental conditions that better match good spatial and mass resolution, will be shown in this chapter.

1 Comparison of Cesium (Cs^+) and Argon cluster (Ar_n^+) ion beams for HOPG sputtering

1.1 Experimental setup

The ToF-SIMS/SPM tool is an instrument which combines ToF-SIMS and Scanning Probe Microscope (SPM) in the same UHV analysis chamber. Its schematic is shown in Figure 3.1 [121]. In such a system the sample stage can be moved between the ToF-SIMS and the SPM parts with sub- μm precision and high speed, by means of a piezo driven stage. In this way, it is possible to analyse the same region of the sample with both techniques and, if the ToF-SIMS instrumentation is equipped with them, with different types of sputtering beams.

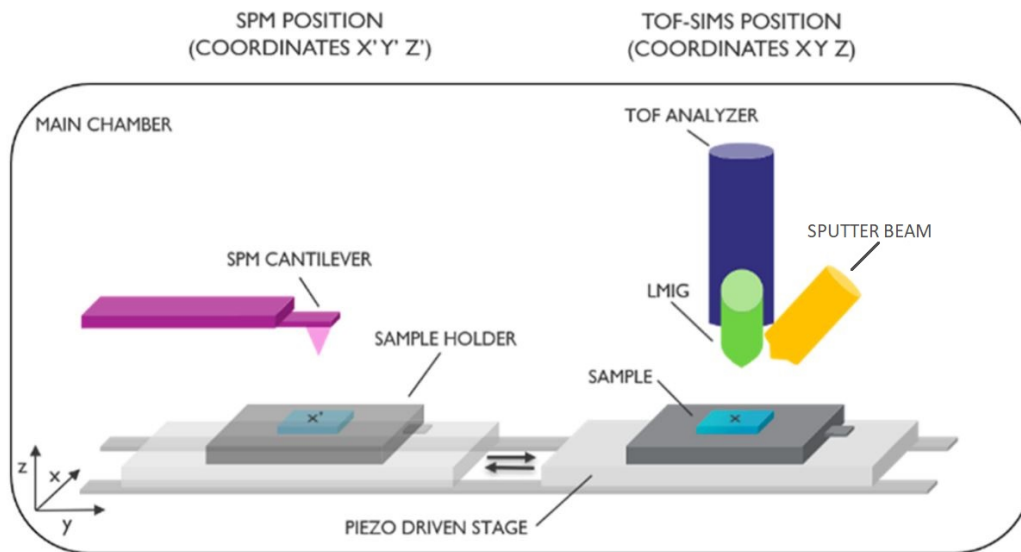


Figure 3.1: Schematic of the combined ToF-SIMS/SPM tool [121].

ToF-SIMS dual beam depth profiling analysis in negative mode was performed on ZYH grade pristine HOPG sample using bismuth (Bi^+ at 30 keV) Liquid Metal Ion Gun (LMIG) as primary beam. Both Argon Gas Cluster Ion Beam (Ar GCIB) and thermal ionisation Cesium source were used as erosion gun, in order to experimentally evaluate the most suitable projectile for the in-depth investigation of our HOPG-based systems. In particular, two Ar cluster sizes, Ar_{1319}^+ and Ar_{1490}^+ , are used at 10 keV (sputter current 2.96 nA) and 20 keV (sputter current 4.73 nA), respectively, while the Cs^+ beam was at the ultra-low energy value of 250 eV (sputter current 14.53 nA). The analysis raster of $100 \times 100 \mu\text{m}^2$ was set at the center of the sputtered area of $300 \times 300 \mu\text{m}^2$.

1.2 Topography modifications induced by ion bombardment

The SPM unit is equipped with a special long-distance surface profiler mode, which allows for measuring the correct shape and depth of large craters (usually several hundreds of micrometers) by switching different independent SPM segments.

The use of long-distance surface profiler is usually exploited for the evaluation of sample sputtered thickness at each point, during dynamic SIMS experiments. This information was then used to convert the sputter time scale into depth scale [121].

As will be described later, such a strategy was used for the crater depth determination in the main investigations of this thesis work, made on the intercalated HOPG sam-

ples. However, for this preliminary work, the SPM long distance surface profiles were mostly used to verify the degree of roughness introduced by the three different sputter guns on the pristine HOPG sample.

The perturbation extent, introduced by the three different ion sources at different energies, can be qualitatively assessed through the three SPM surface profile comparisons in Figure 3.2.

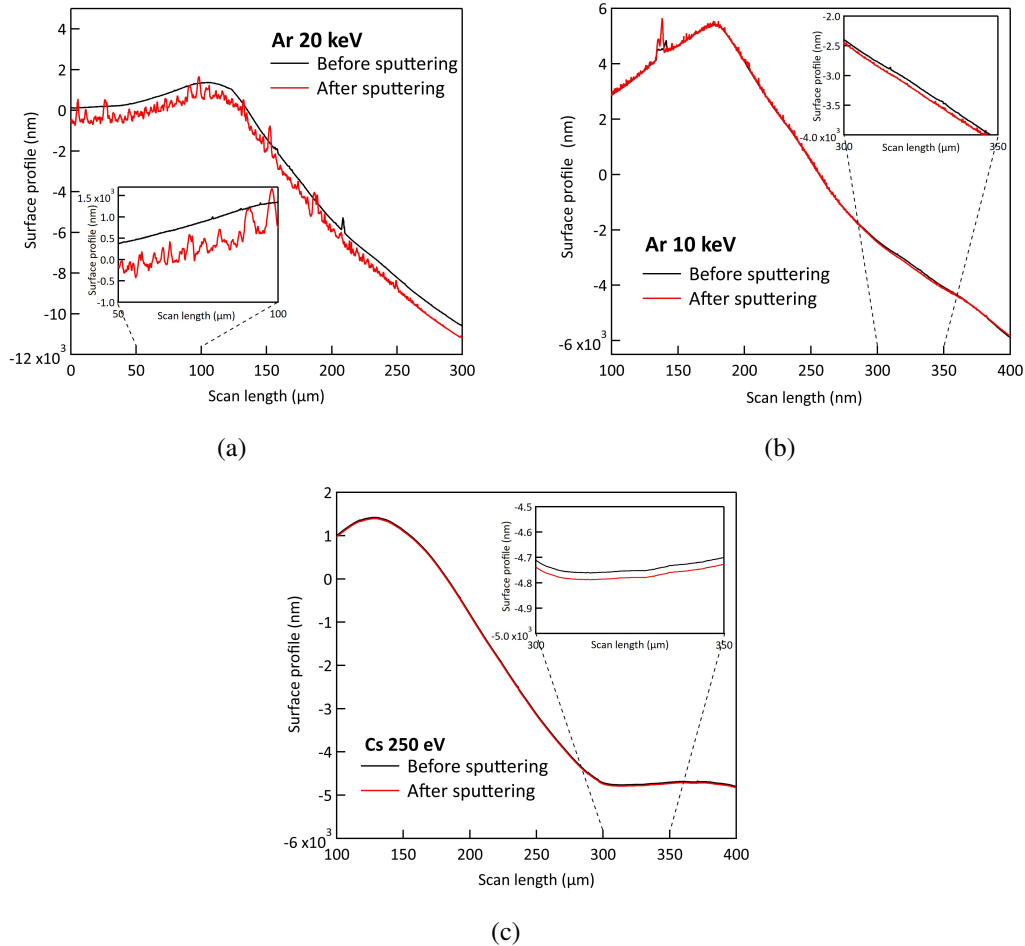


Figure 3.2: SPM surface long-range profiles in X direction ($300 \mu\text{m}$) acquired on the HOPG surface before and after the sputtering process of the ToF-SIMS depth profile measure with (a) Ar^+ cluster beam at 20 keV, (b) Ar^+ cluster beam at 10 keV, and (c) Cs^+ beam at 250 eV. A zoom inset of $50 \mu\text{m}$ along the total profile is shown in each panels.

The ToF-SIMS measurements in dual-beam mode, with Ar^+ cluster at 20 and 10 keV, and with Cs^+ at 250 eV as sputter beams, were all preceded and followed by the SPM profiles acquisitions. The surface profiles of $300 \mu\text{m}$, showed in each plot of Figure 3.2, were performed on the unperturbed and then sputtered area in the X direction, starting from the same X-Y coordinates. In Figure 3.2(a), black and red curves show the topography of the analysed area before and after the sputtering experiment with Ar^+ at 20 keV, respectively. From a qualitative point of view, it appears evident that the Ar^+ cluster sputter beam at high energy heavily perturbs the HOPG surface. Moreover, the zoom inset ($50 \mu\text{m}$) in Figure 3.2(a) clearly shows that the introduced surface roughness does not allow us to obtain information regarding the amount of material removed during the depth-profiling measurements. The same before/after sputtering comparison was made for the Ar^+ at 10 keV beam, in Figure 3.2(b). The roughness introduced by the lower energy Ar^+ beam appears to mainly involve the edges of the crater. In

this case, the red (after sputtering) surface profiles in the zoom inset are qualitatively smoother than in the previous case. The HOPG surface topography appears less perturbed by the 10 keV Ar^+ cluster beam. Comparing the before and after profiles, it is also possible to roughly appreciate the amount of sputtered material. Finally, the best results seem to be those related to ultra low-energy Cs^+ beam. The surface topography after the ToF-SIMS measurements does not seem altered at all in Figure 3.2(c). Here, it emerges that the Cs^+ gun at 250 eV has very gently removed the single layer of the stratified HOPG structure, leaving unaltered the surface shape and not introducing roughness inside the crater. In addition, in this last case, it would be possible to much easier determine the amount of eroded material for sputter time-depth conversion, by evaluating the areas underlying the two curves in the zoom inset in Figure 3.2(c). From these first results we decided to exclude for our purposes the 20 keV Ar^+ , among the three possible choices for the sputtering beam.

1.3 Sputter yield dependence on projectile properties

To evaluate the lateral resolution obtainable with the three considered sputtering beams, the C_2^- (at m/z 24) and C_6^- (at m/z 72) ion signals distribution on the analysed area in the three cases were compared. The two just-mentioned ions were chosen because they are predominant in the mass spectra of the pristine HOPG sample. In Figure 3.3, the ToF-SIMS images ($100 \times 100 \mu\text{m}^2$) of the C_2^- and C_6^- ion signals acquired during the depth profiling experiments with Ar^+ cluster at 20 keV, Ar^+ cluster 10 keV, and Cs^+ at 250 eV are reported in the left panels, central panels, and right panels, respectively. All the images are the sum of the data collected during the total acquisition time of 45 minutes.

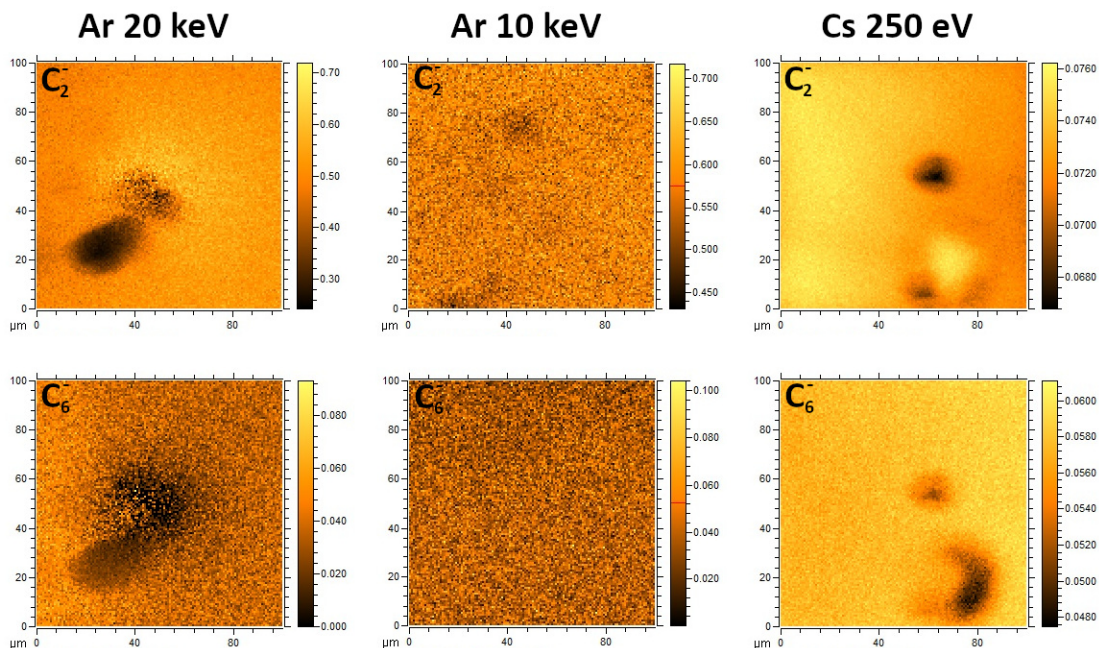


Figure 3.3: ToF-SIMS images ($100 \times 100 \mu\text{m}^2$) obtained in negative mode of C_2^- at m/z 24, and C_6^- at m/z 72 ion signals acquired from pristine HOPG samples with Ar^+ at 20 keV (left panels), Ar^+ at 10 keV (central panels), and Cs^+ at 250 eV (right panels) as sputter beam in the dual-beam ToF-SIMS experiments. The images sum the data collected during the total acquisition time (45 min.). All images are normalized with respect to the total counts image.

The 20 keV Ar^+ cluster beam was excluded, not only for the surface roughness introduced by it on the analysed area, but also because such a surface perturbation was also

reflected in a sort of topographic distortion, well recognisable in the chemical maps in the left panels of Figure 3.3. This topographic deformity is clearly visible in the lower-left part of the C_2^- ion image. In addition, the signal of the C_6^- ion has low intensity counts. The same ion images, in the case of 10 keV Ar^+ cluster (central panels of Figure 3.3), show the absence of topographic distortion effects, but also much lower intensity counts. Considering the same acquisition time (45 min.), the lower energy Ar^+ cluster sputter beam provide a more uniform but less intense distribution for both C_2^- and C_6^- ions, than the higher energy one. It must be taken into account that the 10 keV Ar^+ cluster beam current is slightly lower than in the 20 keV case. For what concern the ultra low-energy Cs^+ sputtering beam, the ToF-SIMS images of the C_2^- and C_6^- ions, in the right panels of Figure 3.3, definitely exhibit the best resolution. In this last case, the intensity counts values are very high and it is possible to appreciate real structural defects of the sample on the uniformly distributed chemical maps of both graphite signals. Choosing to use ultra low-energy Cs^+ as sputtering beam instead of Ar^+ cluster beam, both at high and low energy, the amount of available information from the HOPG analysed area results certainly more adequate. This conclusion was also confirmed by the ToF-SIMS depth profiling results in Figure 3.4. Here, the C_2^- and C_6^- ion depth profiles signals are reported, for the three considered sputtering beams, as a function of the depth predicted on the base of the three different experimental conditions.

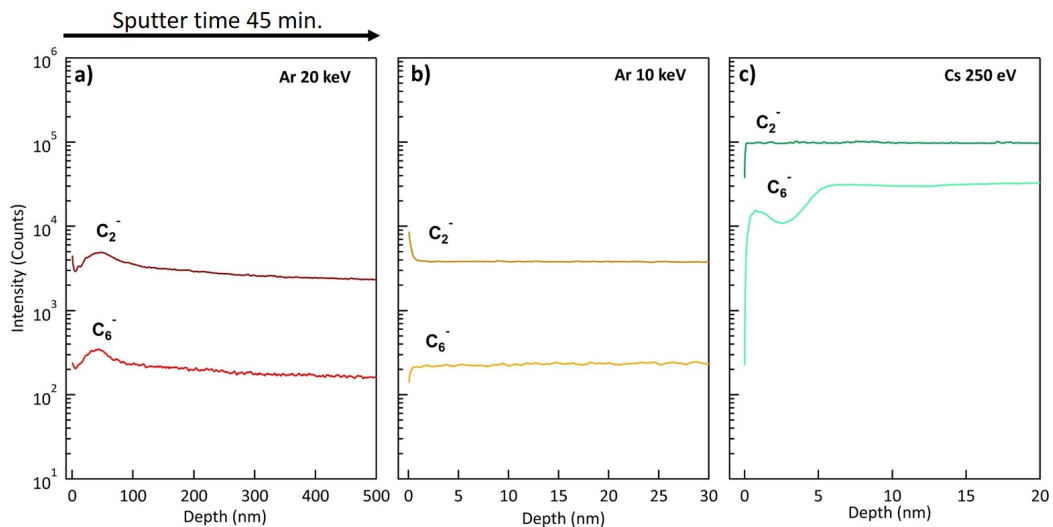


Figure 3.4: Depth profile results from pristine HOPG sample using (a) Ar^+ cluster at 20 keV, (b) Ar^+ cluster at 10 keV, and (c) Cs^+ at 250 eV as sputter beams. Secondary ion intensities of C_2^- at m/z 24, and C_6^- at m/z 72 are plotted versus the expected depth from [67] in (a) and (b), and the depth obtained from SPM profilometry measurements in (c). The acquisition time (45 minutes) is the same for the three reported measurements (a-c).

The sputter time-depth conversion, for 20 keV and 10 keV Ar^+ cluster beams, was made considering the universal equation for argon gas cluster sputtering yields obtained in the M.P Seah work [67]. In this study, the analysis of the sputtering yields of different materials (i.e. organic and inorganic, elemental species and compounds) is made, for argon gas cluster ion beams used in SIMS, as a function of the beam energy, E , and the cluster size, n . It was found that the elemental and compound data expressed as the yields Y of atoms sputtered per primary ion may all be described by a simple universal equation that depends on some parameters, established by fitting.

For the Cs^+ at 250 eV beam, the sputtering yield value present in the literature [89] was compared with our experimental result, from before/after surface topography in Figure

3.2c, about the thickness removed from the HOPG basal plane during the sputtering process. In the wide range of theoretical works on sputter yield calculation, of which the cited one [89] is an example, different projectile-target combinations, energies, and angles on incidence are taken into account. The computational results are then checked through comparable experimental results. Our sputter rate and sputter yield values for Cs^+ at 250 eV on graphite target (~ 0.01 nm/s and 2.14 atoms/ion, respectively) are in good agreement with the expected ones. This accordance will be exploited in the main depth-profiling results on HOPG systems obtained in this thesis work.

The C_2^- and C_6^- depth profile signals were collected up to the deep sample bulk (500 nm along the z-direction) with high energy Ar^+ cluster beam, as shown in Figure 3.4(a). The two graphite signals have a broad intensity maximum within the first 100 nm, then they remain constant during the remaining acquisition time. The intensity counts are however very low, compared to the values expected for carbon cluster ions on a sample of graphite. The depth profile measurement with Ar^+ cluster beam at lower energy and with the same acquisition time, in Figure 3.4(b), involved the first 30 nm of the sample bulk. Also in this case, the intensity counts of the carbon-based signals are low. Finally, the sputter rate value found for the ultra low-energy Cs^+ sputter beam allows us to follow the in-depth evolution of the signals of interest through a very gentle material erosion. The depth scale achieved in 45 minutes, in Figure 3.4(c), can be considered similar to that of the 10 keV Ar^+ cluster beam case, taking into account the uncertainties of this type of calculations [67, 89]. However, in the ultra low-energy Cs^+ case, the detected counts for the C_2^- and C_6^- ions in Figure 3.4(c) are much more intense, as expected. The C_6^- ion intensity fluctuations within the first 5 nm of the sample depth in Figure 3.4(c) will be discussed later. In Figure 3.5, the maximum value of C_2^- and C_6^- secondary ion intensities are shown as a function of the three sputter beams used, in order to better evaluate the ionisation yield difference. The best result is obtained with Cs^+ beam, also considering the experimental uncertainties on the intensity values reported in Figure 3.5.

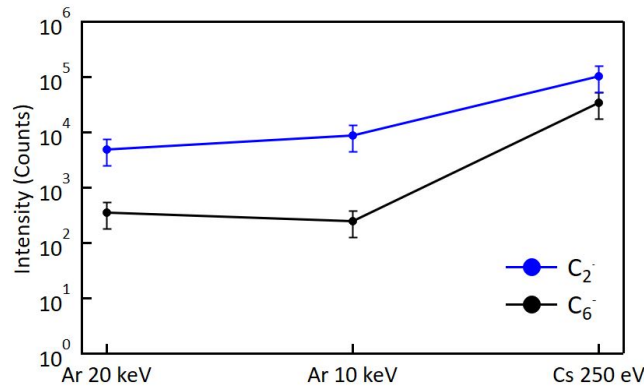


Figure 3.5: Comparison of the maximum value for C_2^- and C_6^- secondary ion intensities from pristine HOPG sample as a function of the sputter beam used. The error bars represent the ToF-SIMS measurement uncertainty, evaluated on the basis of our experimental conditions.

In the light of all these results, we decided to use Cs^+ at 250 eV as sputtering beam for our in-depth analysis of HOPG-based systems. The ultra low-energy Cs^+ beam is, in fact, the best candidate thanks to the smaller induced perturbation on the HOPG surface, and its intrinsic high performance in terms of sputtering yield of negative secondary ions. In addition, it is well known that the use of Cs^+ beam as etching gun, interlaced with bismuth LMIG as analysis beam, gives excellent results in elemental inorganic analysis.

Chapter 4

Anion intercalation in HOPG: surface phenomena

As described in Chapter 1, graphitic electrodes in ion batteries, and graphite electrochemical exfoliation for graphene production are technological processes based on the anion intercalation mechanism in the stratified crystal structure upon immersion in acid solutions. In this context, my thesis work focused on HOPG samples. In the first analysis step, the surface of HOPG samples, treated with electrolyte solutions of 2 M HClO₄ and 1 M H₂SO₄ was studied, in order to identify elemental and molecular species involved in the intercalation processes and, at the same time, find local surface defects through which solvated ions easily reach the HOPG subsurface regions. Results from Cyclic voltammetry (CV), X-ray Photoelectron Spectroscopy (XPS), and Time-of-Flight secondary ion mass spectrometry (ToF-SIMS) will be described and discussed in the following sections.

1 Sample preparation

The preparation procedure for EC intercalation of HOPG samples is schematically represented in Figure 4.1.

Electrochemical techniques are fundamental tools for oxidation and reduction process studies. In dynamic electrochemical techniques, the EC potential can be controlled [123]. When the controlled EC potential is tuned in a certain energy range, the technique is known as voltammetry, and the resulting current, I_{EC} , flowing through the electrode, is measured as a function of the applied EC potential, V_{EC} . A traditional electrochemical setup for voltammetry is the so-called three-electrode cell. It consists of a working electrode (WE), a reference electrode (RE), and an auxiliary (counter) electrode (CE). The surface oxidation(reduction) of interest takes place at the WE, while reduction (oxidation) occurs at the CE, for balancing the total charge of the system; the RE has a constant potential inside the electrochemical bath and ensures a good reference for the WE. Working and counter electrodes are immersed directly in the electrolyte, whereas the RE is generally placed in a separate compartment. The RE potential is usually referred to the standard hydrogen electrode (SHE), which can be realized by contact between molecular hydrogen and its ions on the surface of a platinum (Pt) wire, therefore the main reaction is the electron transfer between the neutral species (H₂) and the ions (H⁺). Unfortunately, the SHE has a limited range of applicability because the liquid junction could be problematic and it cannot be used, either with wholly solid-state EC cells or for very high-temperature reactions. To overcome these problems, a Pt wire, immersed inside an EC can be used. It is the so-called Pt-quasi RE

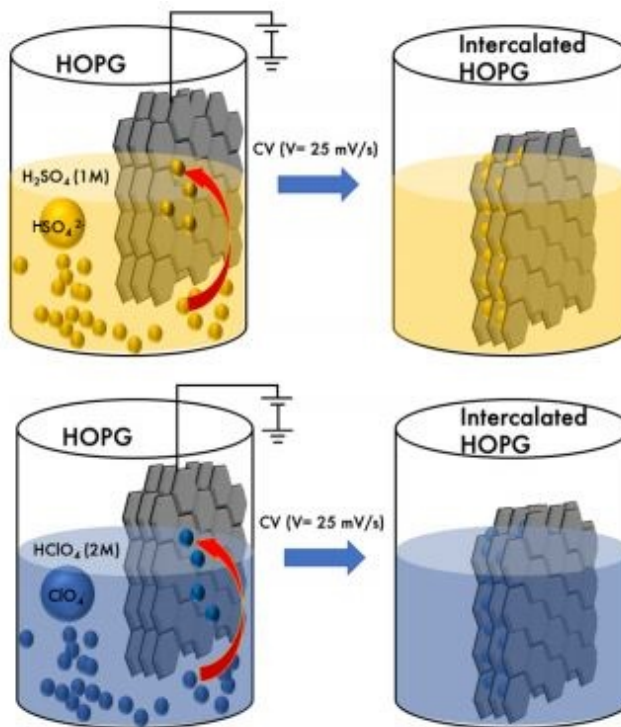


Figure 4.1: Schematic representation of the intercalation process operated on the HOPG samples [122].

(QRef) and maintains a steady (within a few mV) electrode potential; it is very easy to be used; it does not contaminate the electrolyte solution; it is stable in many acids and does not disperse undesired ions in the EC solution. A Pt-QRef is utilised in all the reported experiments of this study.

In cyclic voltammetry (CV), the EC potential applied to the WE is linearly swept starting from an initial value (V_{EC}^i) [35]. After reaching a switching potential (V_{EC}^f), the sweep is reversed and the potential returns to its initial value V_{EC}^i . Conventionally, the positive potentials are plotted in the positive abscissa direction in a CV graph, thus the anodic currents (due to oxidation) are positive, while the cathodic currents (due to reduction) are negative. The presence of current anodic and cathodic peaks ($I_{p,a}$, $I_{p,c}$), at different EC potentials, denotes that an electro-active couple is in the electrolyte solution. The primary CV parameter is the potential scan rate ($v_{\text{scan rate}} = \Delta V_{EC}/t$), since it controls the timescale of the voltammetric experiment. Typical scan rate values range from 1 to 1000 mV/s, accordingly to the studied EC process [124]. The CV scan rate, driving the electron transfer at the electrode-electrolyte interface, can influence the reversibility of the overall EC process. In particular, if the scan rate is too fast with respect to the ion diffusion, the WE is polarized and an overpotential is required for the oxidation (or reduction) process. In a reversible process, the ratio $I_{p,a}/I_{p,c}$ is equal to 1 and this condition is not respected for an irreversible process. The energy separation (ΔV_p) between the anodic and cathodic peaks, defined as $\Delta V_p = (V_{p,a} - V_{p,c})$, is relatively small and corresponds to a value of about $59/n$ mV at 298 K [125]¹. If ΔV_p changes as a function of the scan rate, the redox process is considered irreversible. During a redox reaction, the total charge exchanged between solution and electrode can be evaluated from the acquired voltammogram curve, considering its subtended area value that is proportional to the exchanged charge. In this way, the anodic curve gives the oxidation

¹Values greater than $59/n$ mV are indicative for an irreversible process.

	Conjugated base	pKa	M	pH
H ₂ SO ₄	HSO ₄ ⁻	-3	1	0.0
HClO ₄	ClO ₄ ⁻	-10	2	-0.3

Table 4.1: Important chemical parameters of the used diluted acid electrolytes.

charge (Q_a), while the cathodic curve gives the reductive Q_c . If the ratio $Q_a/Q_c = 1$, the electrochemical process is reversible; for $Q_a/Q_c > 1$, the process is quasi-reversible or irreversible [126].

ZYH grade HOPG samples are used as WE in the EC cell (see Figure 4.1). Before the EC intercalation procedure, the graphite crystals were prepared by peeling using an adhesive tape. Two kind of diluted acid solutions were prepared: 2 M perchloric (HClO₄) and 1 M sulfuric (H₂SO₄) acid, obtained using 70 %, ACS reagent, Sigma-Aldrich and 99.999 %, Sigma-Aldrich, respectively. The samples were intercalated with the two acids at different concentrations in order to have an equal number of anions present in solution.

HClO₄ is a strong acid that completely dissociates when diluted in water, its conjugated base is ClO₄⁻; H₂SO₄ is a strong acid for the first dissociation (HSO₄⁻), while the concentration of SO₄⁻ in water is immaterial. In Table 4.1, the chemical parameters of the two used acids and the prepared solutions are listed [123]. The chosen electrolyte concentrations are in agreement with preliminary graphite intercalation studies present in the literature [62, 127]. The electrolyte solutions were purified by bubbling pure argon (Ar) in a separator funnel for several hours, before each experiment. Ar bubbling helps to remove the dissolved and reactive atmospheric gases, such as oxygen and carbon dioxide, from the liquid.

Cyclic voltammetry was conducted with sweep rate of 25 mV/s and voltage ranging from 0 to 1.3 V (sulfuric acid) and from 0.3 to 1.1 V (perchloric acid). The potential sweep rate was chosen in agreement with a long-standing tradition in the literature regarding graphite anion intercalation [36]. After the EC treatment, intercalated HOPG samples were cleaned under a gentle nitrogen flow.

2 Surface analysis techniques

X-ray Photoelectron Spectroscopy (XPS). The XPS investigation was performed in an ultra-high-vacuum chamber, working at a base pressure of about 1×10^{-10} mbar. The spectrometer contains a 150 mm hemispherical analyzer from SPECS GmbH, working in magnification mode at a pass energy of 20 eV and an Al K α ($h\nu = 1486.6$ eV) source, yielding an overall full width at half maximum spatial and energetic resolution of about 2 mm and 1 eV, respectively.

Time-of-Flight Secondary Ion Mass Spectrometry (ToF-SIMS). ToF-SIMS analysis was performed using a ToF-SIMS V instrument, described in detail in Section 5. Positive and negative ion ToF-SIMS spectra and images were acquired in Bunched mode with Bi⁺ at 30 keV as the primary beam, with dose density below the static limit. The area of analysis for chemical mapping and mass spectra was $500 \times 500 \mu\text{m}^2$. The images were acquired at a lateral resolution of $1/2.6 \mu\text{m}$, approximately. The cycle time of

the ToF analyzer was set to 100 μ s, allowing the acquisition of the spectra in the mass range $1 \leq m/z \leq 882$. Positive and negative mass spectra were calibrated using C^+ , CH^+ , CH_2^+ , CH_3^+ , $C_2H_3^+$, $C_4H_7^+$, and $C_6H_9^+$ peaks and C^- , CH^- , CH_2^- , C_2^- , and C_4^- peaks, respectively. Six mass spectra for each sample were collected in both polarities. All the ToF-SIMS data were acquired, calibrated, preprocessed, analyzed, and exported for further analysis by SurfaceLab v6.5. All images were normalized to total ion image in order to reduce possible topographic effects.

Atomic Force Microscopy (AFM). A Keysight 5500 AFM was employed for morphological characterization of HOPG surface. The acquisition mode was non-contact; the tip radius was approximately 30 μ m, and it was mounted onto an Al-coated cantilever showing a resonant frequency of 300 kHz.

3 Results and discussion

3.1 HOPG intercalation with perchloric and sulfuric acids

The electrochemical behavior of HOPG was first examined by CV measurements, in order to monitor the characteristic intercalation anodic peaks at the proper EC potential values and, hence, the achieved GIC stages. In Figure 4.2, results from CV of HOPG during EC treatment in both 2 M $HClO_4$ (a) and 1 M H_2SO_4 (b) solutions are shown.

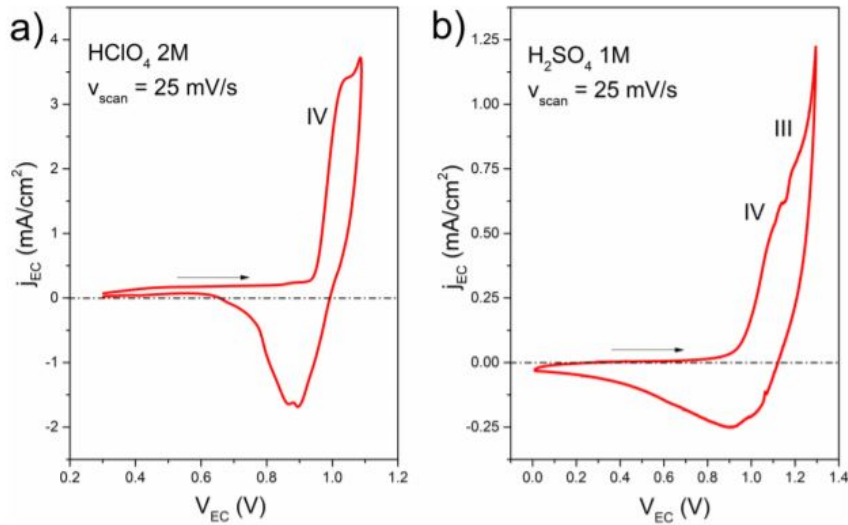


Figure 4.2: Characteristic CV ($v_{scan} = 25$ mV/s) acquired on HOPG treated with (a) 2 M $HClO_4$ and (b) 1 M H_2SO_4 solution. The reported arrows show the CV scan direction [122].

In Figure 4.2(a), the voltammogram for $HClO_4$ acid case is reported in the 0.3 V \div 1.1 V range. Here, three main EC potential intervals can be distinguished: 1) a low-current interval between 0.3 and 0.9 V; 2) an enhancement current window between 0.9 and 1 V; 3) the perchlorate anion (ClO_4^-) intercalation interval between 1 and 1.05 V. In close analogy, in Figure 4.2(b) the CV for H_2SO_4 , in the 0 V \div 1.3 V range, presents the almost null current interval between 0 and 0.9 V, the enhancement current window between 0.9 and 1.1 V, and the sulfate anion (HSO_4^-) intercalation interval between 1.1 and 1.2 V. During the cathodic sweep, negative currents are usually interpreted in terms of a partial de-intercalation process. The difference between the area under the anodic and cathodic peaks in both voltammograms suggests that a non-zero charge has been stored in the sample [59]. The observed features change their energy position

and intensity as a function of the last activated intercalation stage [128]. The fourth intercalation stage is visible as a shoulder in the (a) and (b) voltammograms. Lower numbers of intercalation are placed at higher EC potentials (e.g., see the III intercalation indicated in panel b). Nonetheless, according to the model proposed by Murray and co-workers [56], gas evolution and blister formation are already expected at the fourth stage.

After anion intercalation, in both used acid electrolytes, the HOPG surface morphology was investigated in detail by AFM images acquired in-situ, directly inside the EC cell (EC-AFM) [59]. Here, a precise analysis of the surface quality of the HOPG electrode after the EC treatment is reported. Cracks, blisters-like structures, detriments, and an increase of the mean surface roughness, are statistically predominant features of the collected AFM images. These results cast light on the peculiar alterations (in Figure 4.3) that arise on the HOPG surface during the intercalation process, when HClO_4 or H_2SO_4 are used as diluted electrolytes.

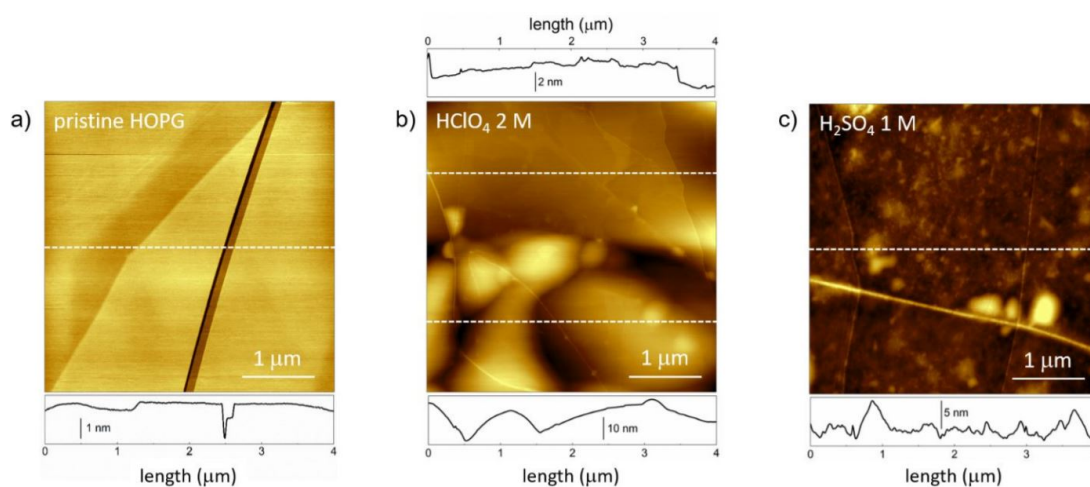


Figure 4.3: AFM images of the sample (a) before the EC treatment, (b) after CV in HClO_4 electrolyte, and (c) after the anion intercalation in H_2SO_4 electrolyte (c). The profile along the dashed lines are reported at the bottom of each image. Having big blisters on the scanned region reported in panel (b), a second profile, acquired along an almost unperturbed area, is also reported at the top of the panel. From a statistical analysis, the measured roughness (defined as the maximum hill-to-valley distance of a profile) is 0.1 nm in (a), 0.4 in the flat region of (b) and 1.0 nm in (c) [122].

3.2 High-resolution XPS results

After the electrochemical treatment, HOPG crystals are analyzed by XPS to collect a first signature of the intercalation process [122].

Figure 4.4(a) is a XPS wide scan of the pristine HOPG, collected for comparison. Wide XPS scans acquired after the sample treatment in perchloric and sulfuric electrolytes are reported in panel (c) and (e), respectively. Individual elemental scans on Cl 2p, S 2p, O 1s, and C 1s have been already discussed in the literature [64]. Our results confirm that the relative intensities of both Cl 2p and S 2p with respect to the C 1s signal (respective intensity ratios of 0.05 and 0.04) can give a rapid countercheck that the intercalation region is correctly reached during the CV.

We focus our attention on the nitrogen (N) peak acquired on pristine HOPG (b, null signal for comparison) and graphite sample surface after CV in (d) HClO_4 , and (f) H_2SO_4 (f) electrolytes. Surprisingly, N is already visible in the wide XPS scans (c and e pan-

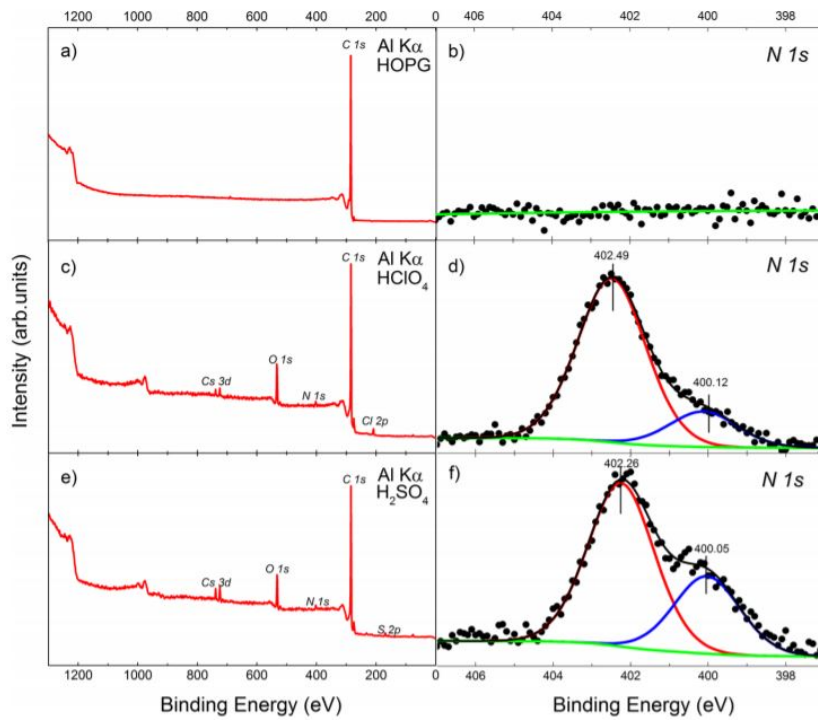


Figure 4.4: XPS survey spectrum and high-resolution N 1s spectrum of pristine HOPG (a and b, respectively); HOPG treated with 2 M HClO_4 solution (c and d, respectively); XPS survey spectrum and high-resolution N 1s spectrum of HOPG treated with 1 M H_2SO_4 solution (e and f, respectively). Regarding the sample treated in perchloric acid, the ratios of N 1s and Cl 2p, with respect to the main carbon feature, are 0.08 and 0.05, respectively. Regarding the sample treated in sulfuric acid, the ratios of N 1s and S 2p, with respect to the main carbon feature, are 0.05 and 0.04, respectively [122].

els), but it has been never considered in previous studies because, in principle, it is an element that is not present among the compounds used for the EC treatment. Nonetheless, even high-purity perchloric and sulfuric acids have contaminants, as side-results of their production. Among them, nitrogen and nitrogen compounds (e.g., NH_4) reach the highest concentration (tens of ppm). Even though the presence of nitrogen was revealed as contamination coming from the high-purity acid solutions, this aspect can be crucial in evaluating HOPG surface modifications induced by the electrochemical treatment. As a consequence, an XPS comparative analysis was reputed to be necessary as a preliminary step in the surface characterization.

The N 1s curves were fitted with two different components. The results collected from the HOPG sample treated in HClO_4 solution discern two binding energies, at 402.49 and 400.12 eV. The N 1s component at a higher binding energy is normally referred as pyrrolic component, while the component at 400.12 eV usually corresponds to the so-called pyridinic component. Their ratio is different on the HOPG sample treated in H_2SO_4 solution. The dissolution process of the graphite basal plane is different in the two acid electrolytes [52, 64] and this can give a rationale of the observed signals.

3.3 Static ToF-SIMS results

Figure 4.5 shows ToF-SIMS negative (Figure 4.5a-c) and positive (Figure 4.5d-f) ion mass spectra of the pristine HOPG surface (Figure 4.5a,d), and the HOPG surface after the electrochemical treatment in perchloric acid solution (Figure 4.5b,e), and in sulfuric acid solution (Figure 4.5c,f) [122].

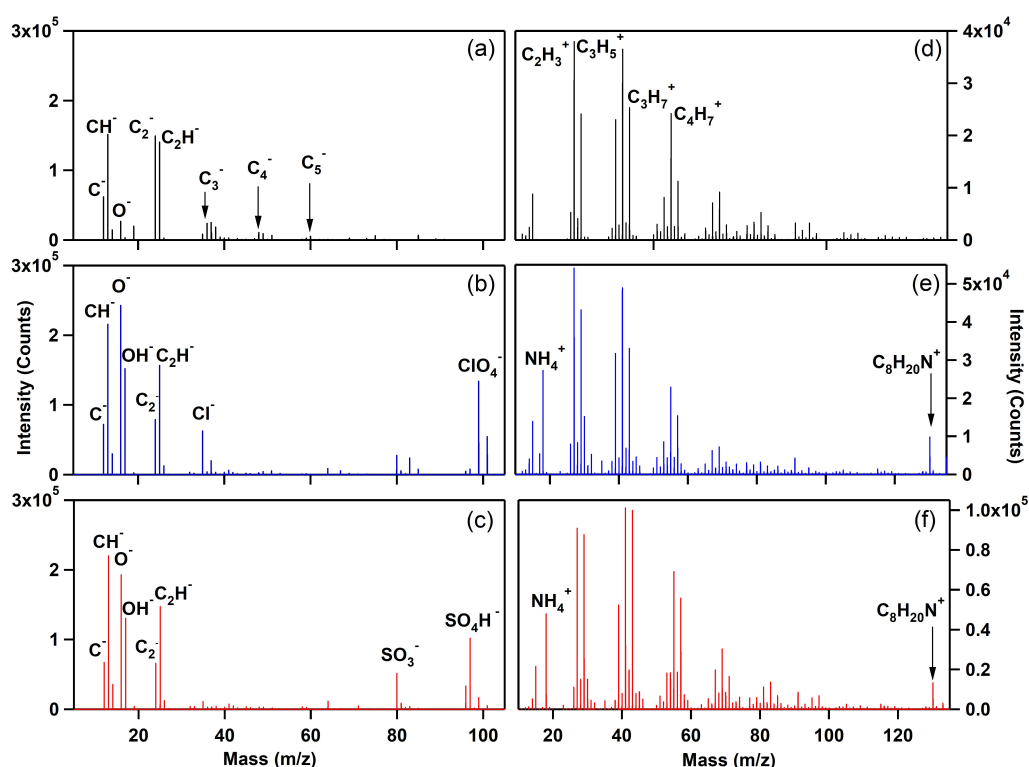


Figure 4.5: ToF-SIMS negative (a-c) and positive (d-f) ion spectra of pristine HOPG (a, d), HOPG after intercalation with HClO_4 solution (b, e), and HOPG after intercalation H_2SO_4 solution (c,f) [122].

Negative ToF-SIMS mass spectra of pristine HOPG (Figure 4.5a) show typical negative fragment ions of graphite: the spectrum is dominated by CH^- ($m/z = 13$), C_2^-

($m/z = 24$), and C_2H^- ($m/z = 25$) ion signals together with the C_n^- ($n = 1, 2, 3...$) ion series. These characteristic HOPG ion signals have been already reported in previous works [129–131]. It is interesting to note, when comparing Figure 4.5a to Figure 4.5b, and Figure 4.5c, that graphite characteristic ion peaks such as C_2^- , C_3^- , C_4^- , C_5^- and C_6^- strongly decrease in intensity when HOPG crystals are electrochemically treated in both diluted acid electrolytes. In addition, mass spectra in negative ion mode obtained from intercalated HOPG samples reveal a much more intense oxygen ion peak O^- ($m/z = 15.99$), than the pristine graphite surface. These results can be interpreted assuming that the well-ordered HOPG topmost layer lattice is damaged by the aqueous electrolytes, which oxidise the carbon atoms, forming graphite oxides. Thus, as a consequence of the electrochemical oxidation process, an increase in the HOPG surface roughness can be revealed at the nano-scale (see the AFM data reported in Figure 4.3).

Several chemical species related to the diluted acids have been detected. In particular, chloride Cl^- ($m/z = 35$) and perchlorate ClO_4^- ($m/z = 98.95$) ions in Figure 4.5b, sulfide SO_3^- ($m/z = 79.96$), and SO_4H^- ($m/z = 96.96$) ions in Figure 4.5c are clearly appreciable in the mass spectra due to their higher intensity.

In positive ion mode (Figure 4.5d-f), the presence of typical $C_xH_y^+$ fragment ion signals, in the low-mass range, characterizes the surface chemical structure of all three samples. These non-specific hydrocarbon fragment can be imputed to the graphite fragmentation occurring during the ion bombardment [131].

Comparing the mass spectra of pristine and intercalated HOPG, one of the most unexpected features is the presence of a very intense NH_4^+ ($m/z = 18$) signal, and also of a series of different nitrogen-based compounds. The most appreciable of them can be observed, in both intercalated samples, at $m/z = 130.15$ (Figure 4.5e,f). On the base of the calibration we used for the mass spectra, this peak was assigned to the $C_8H_{20}N^+$ ion. The same assignment was done by Alexander and co-workers in the context of the surface characterization of ammonium-bicarbonate electrolytically oxidized PAN-based carbon fibers. In the above-mentioned work, the presence of nitrogen-containing species was attributed to an incomplete graphitization of PAN fibers or a presumed aliphatic amine contaminant [132]. On our case, the considerations previously made about the possible sources of nitrogen [133] are also valid. However, this unexpected surface functionalization could be of great interest considering the large use of nitrogen functionalized graphene in energy and biomedical applications [134, 135].

In Figure 4.6, the spatial distribution of NH_4^+ and $C_8H_{20}N^+$ secondary ion signals on the same analyzed area is provided for both intercalated samples. The ToF-SIMS images are normalized with respect to the total ion image. The space distribution of the NH_4^+ signal on the HOPG surface treated with $HClO_4$ (Figure 4.6a) and H_2SO_4 (Figure 4.6b) validates the picture described above. The chemical identification of the NH_4^+ ion on the sample intercalated with $HClO_4$ solvent shows a higher signal in well-defined small (few tens of microns) spots. The latter are placed around the edges of a circular macroscopic defect present at the top left of the ToF-SIMS map and close to two macroscopic fractures, which extend transversely across the analyzed area (starting from the top right of the reported image). Furthermore, in the $C_8H_{20}N^+$ secondary ion image of the sample intercalated with perchloric acid (Figure 4.6c), we do not recover the same features observed for the ammonium ion. Here, the counts collected are less intense, except in an area on the right of the image, where the signal seems to be more intense very near the edge of one of the two macroscopic fractures. In Figure 4.6b, the surface distribution of the NH_4^+ ion signal on the HOPG surface after EC intercalation

in H_2SO_4 solution is shown. In the same way, the ammonium ion spreads on the intercalated HOPG surface follows the shape of the typical surface defects, where acid functionalities can be in higher concentrations. Regarding the chemical mapping of the $\text{C}_8\text{H}_{20}\text{N}^+$ molecule in the sample treated with sulfuric acid (Figure 4.6d), it shows a similar intensity with respect to the previous case, but the $\text{C}_8\text{H}_{20}\text{N}^+$ molecule results more evenly distributed with respect to the NH_4^+ signal.

These first results gave us a clear and detailed picture of the surface chemistry of the HOPG samples, before and after the anion EC intercalation process.

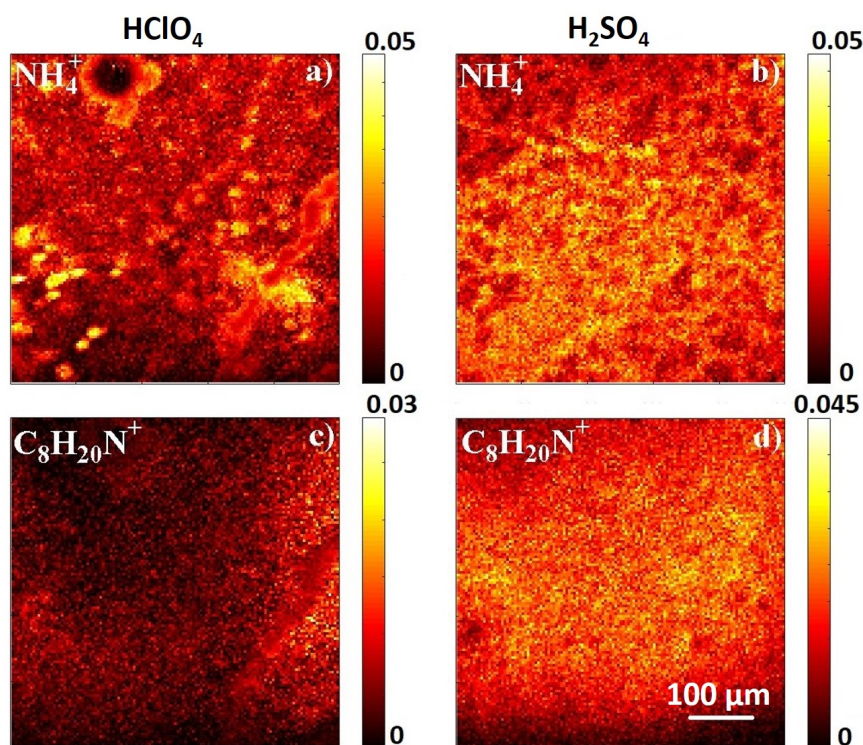


Figure 4.6: Normalized ToF-SIMS images ($500 \mu\text{m} \times 500 \mu\text{m}^2$) obtained in positive ion mode from HOPG surface after treatment with 2 M HClO_4 solution of (a) NH_4^+ and (c) $\text{C}_8\text{H}_{20}\text{N}^+$ secondary ion signals and from HOPG surface after treatment in 1 M H_2SO_4 of (b) NH_4^+ and (d) $\text{C}_8\text{H}_{20}\text{N}^+$ secondary ions signals [122].

In order to exploit at best the ability of ToF-SIMS images to identify the surface makeup of the samples, both from a structural and chemical point of view, we have chosen to focus our attention mainly on the elemental and molecular species coming from the acids and the EC treatment. As mentioned above, a considerable number of fractures rise up on HOPG surface after the intercalation process in diluted HClO_4 . It was possible to observe such fractures from the total ions ToF-SIMS images, as reported in the example of Figure 4.7a. Figure 4.7b-d shows ToF-SIMS chemical maps representing the spatial distribution of C^- , Cl^- , and ClO_4^- ions, respectively [122].

From this damaged area, the C^- ion signal intensity, which we expected to be uniformly distributed, is less intense on the fracture boundaries (Figure 4.7b). The Cl^- ion signal (Figure 4.7c) spreads all over the analysed sample surface, with specific areas with a higher ion signal intensity. It seems to delineate a defined surface portion corresponding to a macro-blister of tens of microns. Finally, it is interesting to take attention to the chemical map of the solvated anion ClO_4^- , which is directly involved in the intercalation process (Figure 4.7d). It is evident that the ClO_4^- ion signal has a different spatial distribution when compared to the Cl^- ion one: the perchlorate ion signal

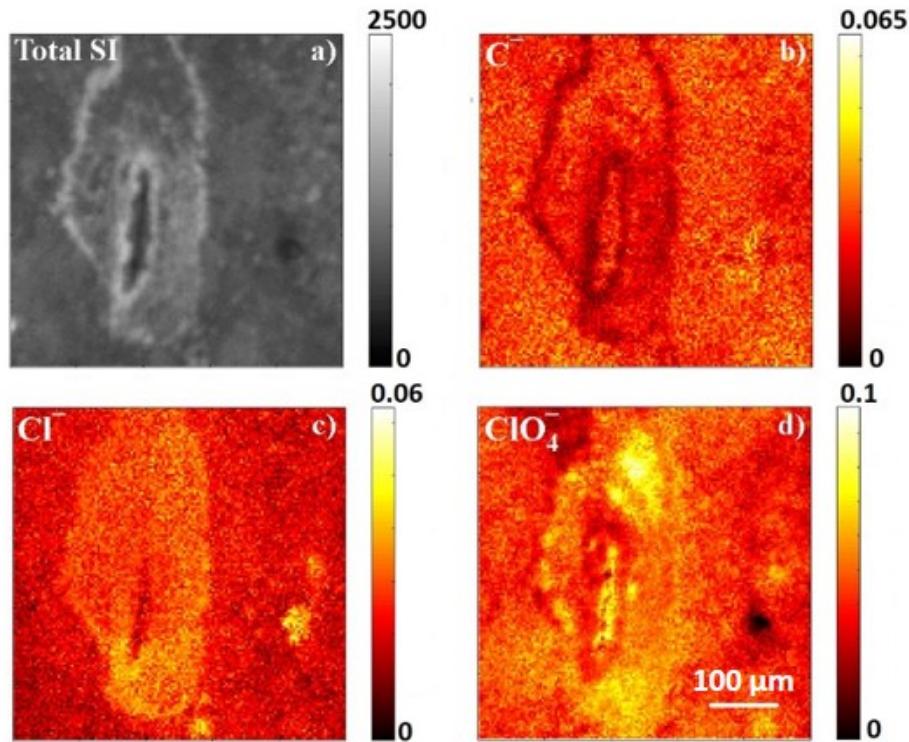


Figure 4.7: Normalized ToF-SIMS images ($500 \mu\text{m} \times 500 \mu\text{m}^2$) obtained in negative ion mode from HOPG after treatment with 2 M HClO_4 solution of (a) total, (b) C^- , (c) Cl^- , and (d) ClO_4^- secondary ion signals [122].

is more intense right in the middle of the fracture, where the graphite crystal surface is clearly damaged. Considering that all the chemical maps were normalized to the total ion image in order to avoid topographic effects, the not uniformly distributed ion signal can be imputed to a higher count rate for specific regions. This unexpected outcome underlines the presence of a higher concentration of perchlorate ions in well-defined areas. Specifically, such results give us a direct proof of the long-standing theoretical hypothesis regarding the preferential intercalation sites of the inserted solvated ions in HOPG layered structure. It is possible to definitively affirm that graphite defects are the preferential starting structural points for the electrochemical anion intercalation process. Similar considerations were made even for other chemical species from the electrolyte, such as ClO_2^- , ClO_3^- , and ClO_4H^- , whose chemical maps are in Figure 4.8.

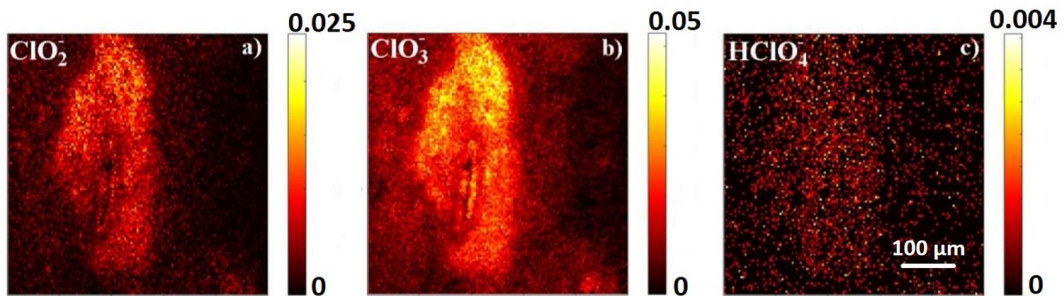


Figure 4.8: Normalized ToF-SIMS images ($500 \mu\text{m} \times 500 \mu\text{m}^2$) obtained in negative mode from HOPG after intercalation with 2 M HClO_4 solution of (a) ClO_2^- (b) ClO_3^- and (c) ClO_4H^- secondary ion signals [122].

Regarding the sulfuric acid case, in the early stages of the HOPG intercalation process, the predominant contribution to the chemical reaction, described by the second Equation in 1.1, come from the SO_4H^- anion. With this in mind, the comparison between the surface chemical distributions of C^- , S^- , and SO_4H^- ions, reported in Figure 4.9 [122], is absolutely eye-catching.

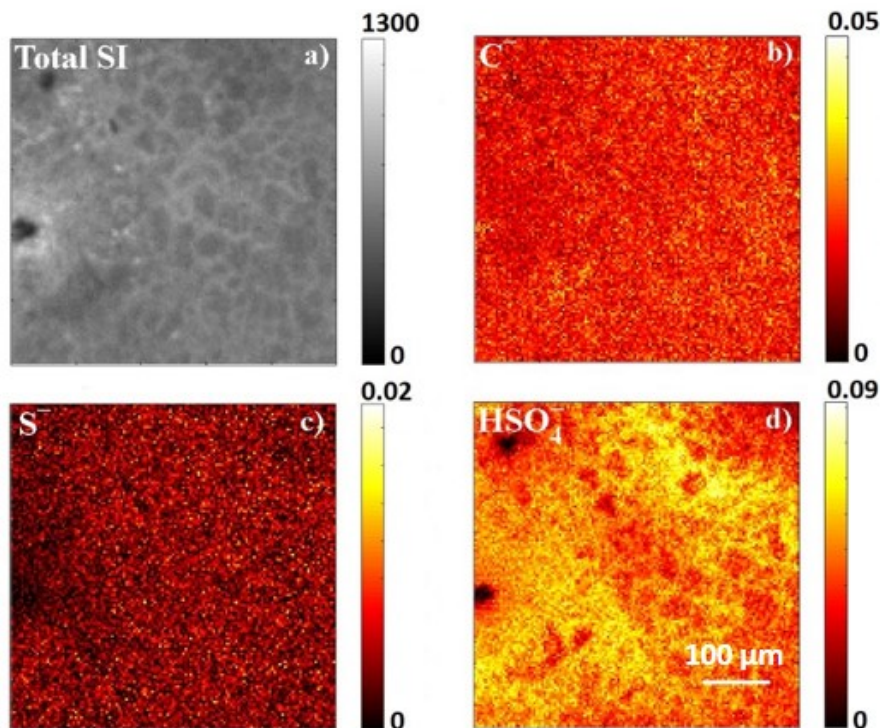


Figure 4.9: Normalized ToF-SIMS images ($500 \mu\text{m} \times 500 \mu\text{m}^2$) obtained in negative ion mode from HOPG after intercalation with 1 M H_2SO_4 solution of (a) total, (b) C^- , (c) S^- , and (d) SO_4H^- secondary ion signals. [122].

The total ion image in Figure 4.9a outlines a representative region of the sample where, conversely to Figure 4.7a, there is not clear damage of the HOPG basal plane. However, a dense network of interconnected micro fractures is easily recognizable. Despite the absence of macroscopic structural defects, there are again explicit differences in the spatial arrangement of the chemical species highlighted on the HOPG surface. The C^- signal, in Figure 4.9b, is uniformly distributed, as expected; the S^- ion, showing a homogeneously spread mapping over the entire analyzed area in Figure 4.9c, looks as to be a residual contamination from sulfuric acid. Looking at the SO_4H^- ion map, it is instead possible to recognise distinct areas with higher ion signal intensity. This emerges distinctly in Figure 4.9d, where the chemical planar distribution of SO_4H^- exhibits a definite network similar, in shape, to the microscopic surface fractures, found in the total secondary ion image. The SO_4H^- ion signal is not homogeneously distributed all over the HOPG surface like the sulfur ion, and as usually observed in the case of the chemical in-plane arrangement of contaminants. Conversely, it is mostly present within the defective surface regions, so far observed and followed on intercalated HOPG samples only from a morphological point of view. Moreover, we found that an atypical ion signal distribution, albeit to a lower degree, is present also in the chemical maps of SO_2^- , SO_3^- , and SO_4^- , in Figure 4.10.

All the results showed so far, gave us an explanation for some of the observations previously earned on such kind of systems [59]. In particular, the crucial chemical role of

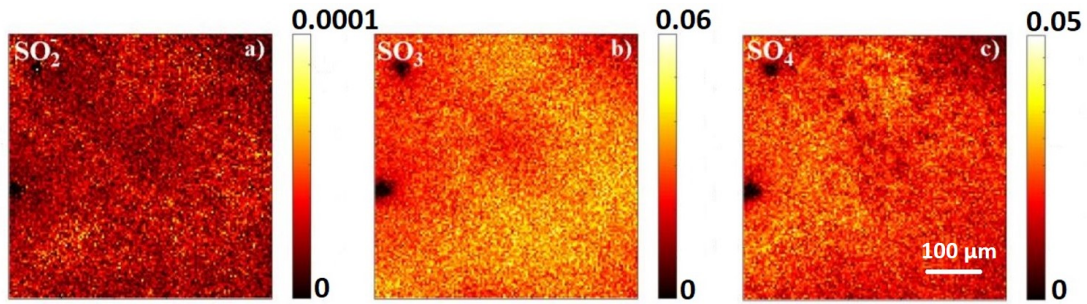


Figure 4.10: Normalized ToF-SIMS images ($500 \mu\text{m} \times 500 \mu\text{m}^2$) obtained in negative mode from HOPG after treatment with 1 M H_2SO_4 solution of (a) SO_2^- , (b) SO_3^- , and (d) SO_4^- secondary ion signals [122].

the acid conjugated bases, specifically of the ClO_4^- and SO_4H^- ions, has been proven and correlated to the formation of HOPG surface detriment (e.g., graphite terraces² dissolution, blisters..). We can contribute to the improvement of the model proposed by Murray [52] and, then, adopted by Alliata [61, 62], through the localisation, at the micrometer scale, of the molecular species present on the HOPG surface after the very first stages of graphite intercalation in both perchloric and sulfuric acid aqueous solutions. On the strength of these achievements, we realized that key-findings would be obtained by the investigation of the sub-surface regions of HOPG crystal through low-energy ion beam depth profiling experiments.

²Crystal terrace is defined as the removal of an atom or molecule from the uppermost surface.

Chapter 5

Anion intercalation inside the HOPG buried layers

Starting from the new results presented in the previous chapter, further details of the intercalation mechanism on graphite electrodes with diluted HClO_4 and H_2SO_4 electrolytes were investigated. Both a pristine HOPG crystal and a simply immersed one in the same acid solutions were used as reference samples in this case. Exploiting the ToF-SIMS/ in-situ SPM tool, described in Chapter 3, a picture of the chemical species involved in the intercalation reaction was provided through the depth concentration profiles of the anion signals along the HOPG electrode.

The model that describes the solvated ClO_4^- and SO_4H^- anion percolation between the HOPG layers involves the Graphite Intercalated Compounds (GIC) formation, with different transport properties with respect to the pristine sample. It follows that GIC is considered a new crystal having intercalated ions between ordered arrays of one or more graphite layers.

It is well-known that the most evident morphological change on the crystal surface after the graphite intercalation, in perchloric and sulfuric acids, is the formation of blisters. Such a bubble-like circular structures, that swell the HOPG basal plane, are generally interpreted as a consequence of the evolution of gaseous molecular species (CO , CO_2 , and O_2) during the oxidative process. If blisters induce a detriment of the HOPG surface, the gas production significantly affects the crystal bulk (defects, dislocations, strains, etc.). Because of this, having a complete picture not only of the HOPG surface but also of the bulk chemical evolution during the exfoliation process becomes crucial. In order to investigate intercalation also in the sub-surface regions of the HOPG crystals, we exploited dual beam ToF-SIMS depth profiling experiments at very low energy. The use of low energy ion Cs^+ ion sputtering has been already demonstrated to be efficient for characterizing hybrid organic/inorganic architectures with sub-nanometer depth resolution [136]. In addition, the preliminary investigations described in Chapter 3 demonstrated that ultra low-energy Cs^+ beam is the best performing for HOPG samples.

1 Samples preparation

ZYH grade HOPG samples were electrochemically intercalated in (2 M) HClO_4 and (1 M) H_2SO_4 acid solutions with the same methodology described in Section 1 of Chapter 4. In addition, ZYH grade HOPG samples were only immersed for some minutes, in view of having comparable time intervals as those ones required for performing the Cyclic-Voltammetries (CV), in the two diluted acid solutions. The simple crystal

immersion was used as a countercheck for the final data interpretation. CV (25 mV/s) was performed in the range 0.0 to 1.3 eV (H_2SO_4) and from 0.0 to 1.1 V (HClO_4) to reach the IV intercalation stage in both cases. After the EC process, HOPG samples were dried under gentle nitrogen flux.

2 ToF-SIMS/in-situ AFM setup

HOPG crystals were analyzed with the ToF-SIMS/SPM tool, already described in Chapter 3. Such an instrument allows the suspension of the ToF-SIMS depth profile experiment and a subsequent transfer of the sample stage to the SPM position without breaking the vacuum. Regarding the dual beam ToF-SIMS depth profile conditions, Bi^+ at 30 keV in bunched mode was used as primary beam and low energy (250 eV) Cs^+ ion source (250 eV) as erosion gun. The analysis raster of $(100 \times 100) \mu\text{m}^2$ was set at the center of the sputtered area of $(300 \times 300) \mu\text{m}^2$. With the in-situ Scanning Probe Microscopy instrumentation, both AFM morphological images, and SPM long distance surface profiles were acquired. ToF-SIMS chemical maps were collected on the same sample areas of the AFM ones, with the purpose of comparing the topography and the chemical information at the surface and sub-surface regions. AFM was operated in contact mode for all the reported measurements.

2.1 Craters depth evaluation

The depth crater values were experimentally established through the same methodology used in 3. In-situ SPM long distance surface profile measurements is acquired on the analysed area before and after each depth-profiling measure. The values were afterward used for intensity-time to intensity-depth profile calibration, assuming a constant sputter yield during the depth profiling experiments. The sputter yield value, resulting from the calibration, is consistent with the literature data regarding our experimental conditions [89].

3 Results and discussion

3.1 General remarks of the intercalation process

A schematic representation of the HOPG intercalation process from the surface, then through the sub-surface regions, and finally down to the crystal bulk is reported in Figure 5.1. This reaction can be conceived as a two-step process. The first one involves the HOPG basal plane: solvated anions (water molecules are not depicted in Figure 5.1) exploit structural crystal defects to reach buried graphene layers. The second process stage foresees the anions spread within the graphite layers. At the end of these two-steps, anions should be located, along the z-direction, at a mean ordered spatial intervals of n graphene layers ($n = 1, 2 \dots$). Up to now, a detailed analysis of this second phase and the effects of the different employed electrolytes have not been fully explored, yet. Figure 5.2, the CVs show the evolution of the Faradaic current through HOPG in (a) HClO_4 and (b) H_2SO_4 electrolytes.

The shoulder, related to the fourth anion intercalation stage ($n = 4$) is highlighted in the positive scans of the voltammograms (a) and (b). The negative peak is traditionally interpreted in terms of a partial ions de-intercalation, which gives a quasi-reversible character at the overall reaction.

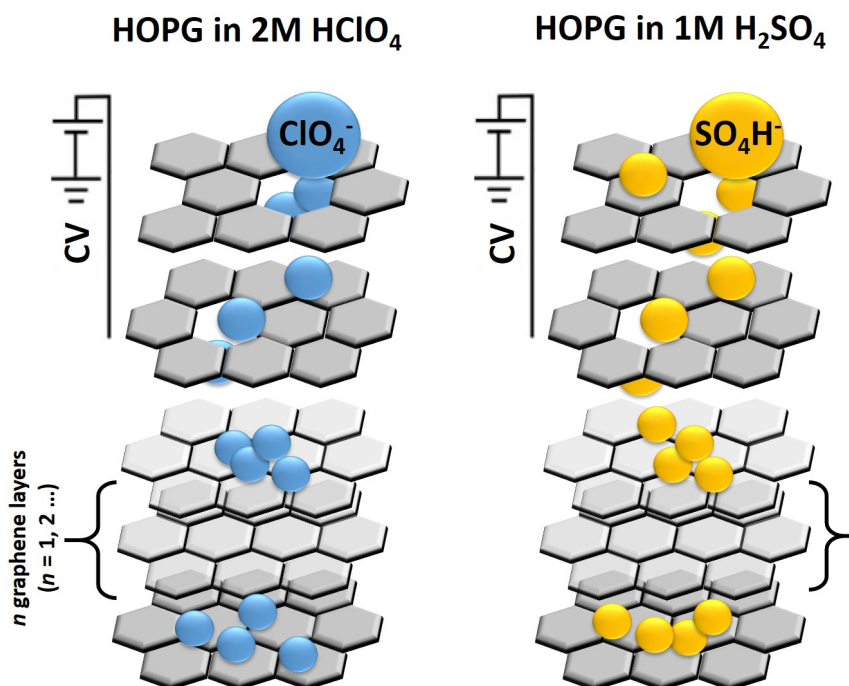


Figure 5.1: Schematic illustration of the intercalation process operated on the HOPG samples with acid solutions of HClO₄ (left) and, on the right side, H₂SO₄ (for more simplicity, anions are not solvated in the picture). The scheme shows the proposed model for the generic n th ion intercalation stage, where the electrolyte anions take advantage from the crystal surface defects to reach the HOPG sub-surface regions.

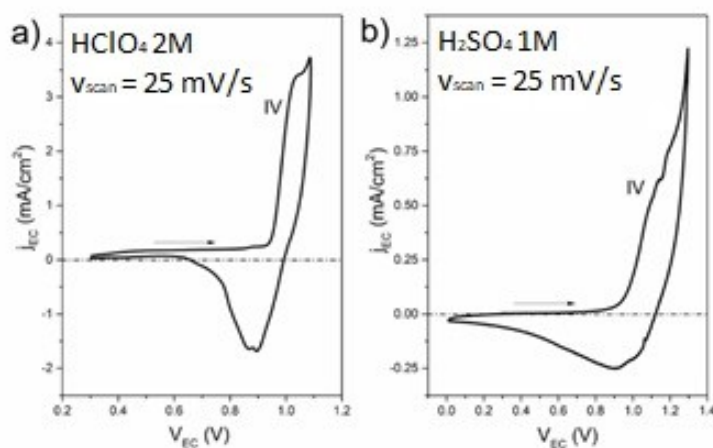


Figure 5.2: Characteristic CV ($v_{\text{scan}} = 25 \text{ mV/s}$) acquired on HOPG treated with (a) 2 M HClO₄ and (b) 1 M H₂SO₄ solution. The reported arrows show the CV scan direction.

3.2 Chemical and morphological analysis of the “surface” and buried graphite layers

Pristine HOPG sample was initially studied as a reference sample for the ToF-SIMS depth-profile investigation in dual-beam mode. In Figure 5.3, depth profile results, which sums the data over the entire analysed area of untreated HOPG sample are reported.

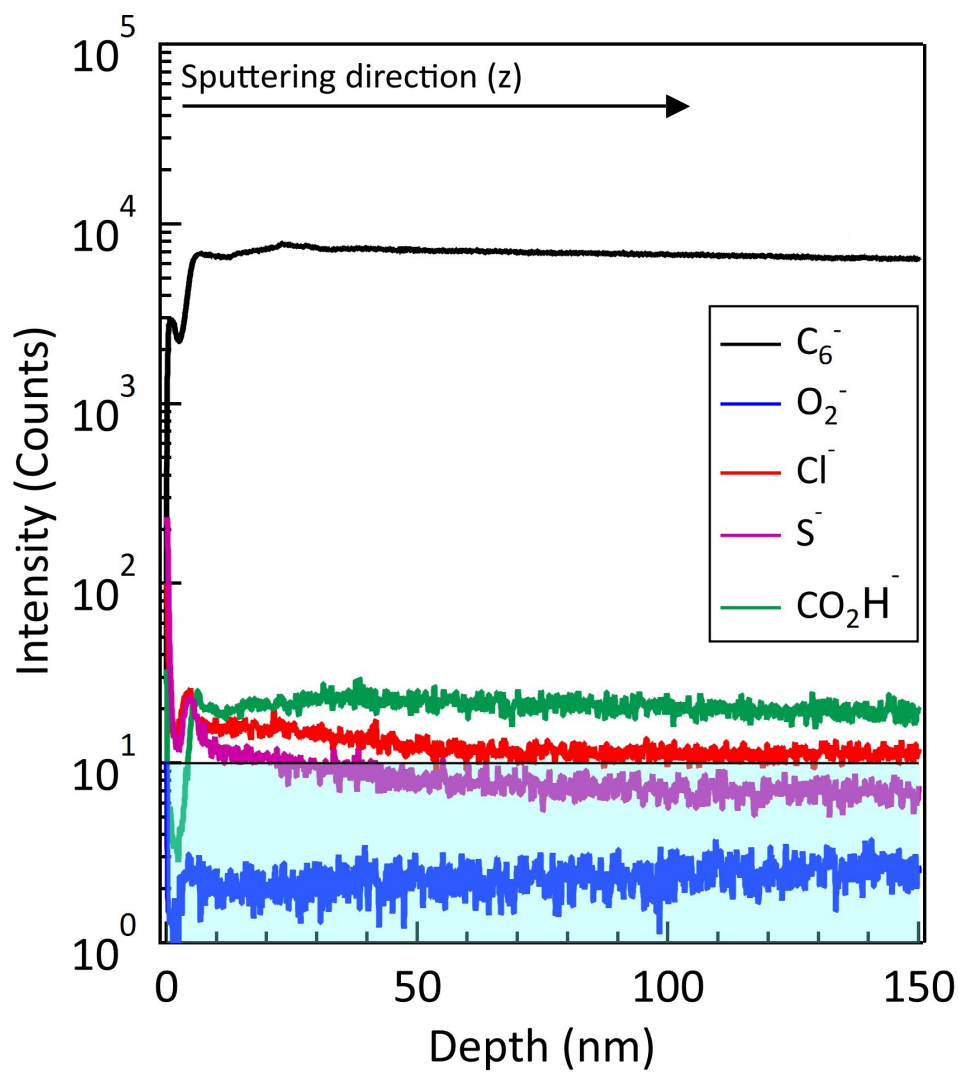


Figure 5.3: Depth profile of a pristine HOPG sample. Secondary ion intensities of C_6^- at m/z 72, O_2^- at m/z 31.99, Cl^- at m/z 34.96, S^- at m/z 31.97, and CO_2H^- at m/z 44.99 are plotted versus the depth.

The elemental and molecular ion signal intensity for C_6^- , O_2^- , Cl^- , S^- , and CO_2H^- is represented as function of the depth. As already done in some works present in the literature [129], the C_6^- signal can be used as reference secondary ion for graphite. The O_2^- , Cl^- , S^- , and CO_2H^- compounds, which we expect to measure on the EC treated and immersed samples, show negligible intensities close the detection limit (light blue shaded area). The latter is reported in each depth profile plot for a better evaluation of the data. Sulphur and chlorine are present on the crystal surface in elemental form (S^- , Cl^-). Their signal decrease in intensity very rapidly together with O_2^- ion signal. Contamination from sulphur and chlorine in both elemental form and as compounds can occur when HOPG surface is exposed to the atmosphere [137].

With exploratory purposes, HOPG was analysed by AFM to confirm the evolution of surface blisters, the latter being a fingerprint of the happened reactions, following the EC treatment. In Figure 5.4, we report two representative AFM images of the HOPG surface upon reaching the fourth stage of intercalation in (a) HClO_4 and (b) H_2SO_4 electrolytes. In the former case, it is possible to recognize sub-micrometric lattice defects; in the lower-left area, different blisters affect the surface and, just above, a general detriment of the electrode surface is observed by AFM. In Figure 5.4b, blisters (having an average size of less than $1\ \mu\text{m}$) are even more evident after the H_2SO_4 treatment.

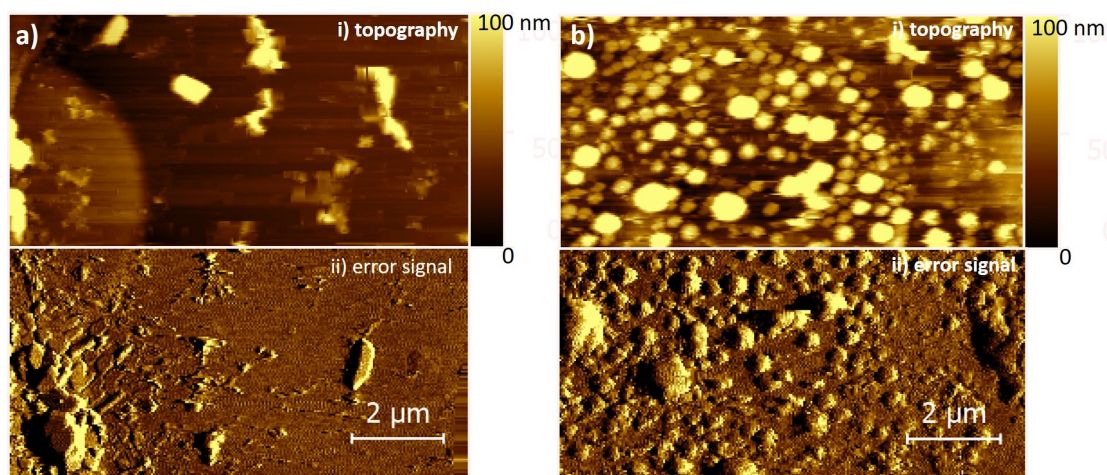


Figure 5.4: AFM images ($10 \times 10\ \mu\text{m}^2$) of HOPG surface intercalated in (a) 2 M HClO_4 solution and in (b) 1 M H_2SO_4 solution. For both images, AFM topography (top panel) and error signal AFM mode (bottom panel) are shown.

The intercalated samples were thus studied by the dynamic ToF-SIMS approach. The results are then compared with those acquired on the immersed samples.

In both cases (intercalated and immersed samples) the C_6^- signal intensity reaches a plateau approximatively within the first 4 nm, as clearly visible in Figure 5.5.

Intensity signals related to the anions from (a) HClO_4 and (b) H_2SO_4 (b) acids and some oxygen-based ion fragments (c,d) are reported.

Considering that the chlorine and sulfur based molecular species are directly involved in the EC process, we would like to figure out possible differences in ClO_4^- and SO_4H^- ions behavior.

For what regards the HOPG **intercalated sample** with HClO_4 , it is possible to appreciate that the ClO_4^- ion, panel (a) of Figure 5.5, is more concentrated in the first 2 nm. Nevertheless, the anion is strongly present even in the sample buried layers. This result suggests that the intercalation process proceeds beyond the uppermost graphite layers.

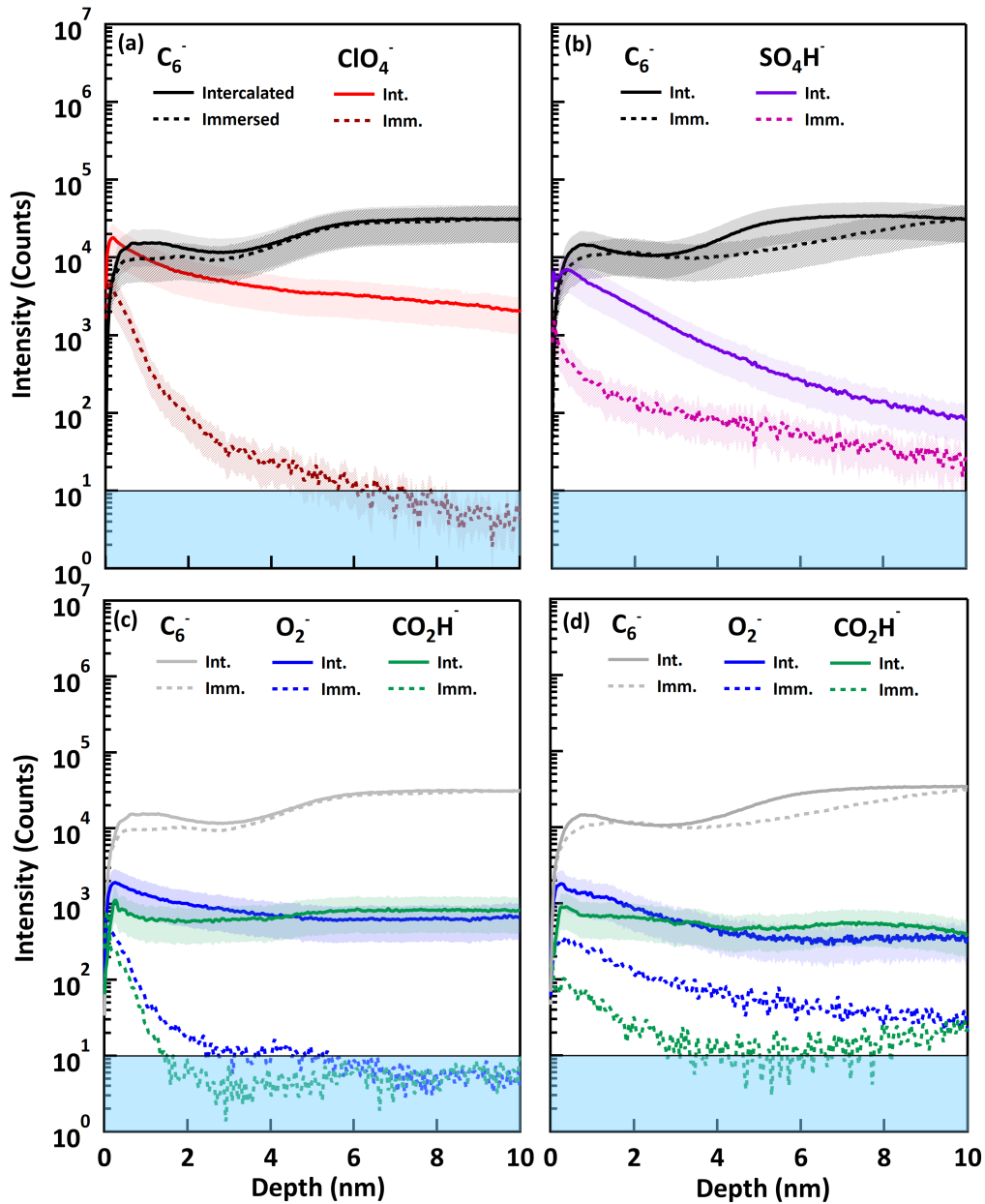


Figure 5.5: ToF-SIMS depth profiles of HOPG intercalated and immersed in HClO_4 solution (a,c) and in H_2SO_4 solution (b,d). Secondary ion intensities of C_6^- at m/z 72, and ClO_4^- at m/z 98.94 are shown in panel (a) for immersed and intercalated sample in HClO_4 solution; C_6^- , and SO_4H^- at m/z 96.95 are shown in panel (b) for immersed and intercalated sample in H_2SO_4 solution; O_2^- at m/z 31.99, and CO_2H^- at m/z 44.99 are shown in panel (c) for immersed and intercalated sample in HClO_4 solution and in panel (d) for immersed and intercalated sample in H_2SO_4 solution. All secondary ion intensities are plotted versus the depth, starting from the surface to 10 nm. The shaded bar areas of the profile curves represent the ToF-SIMS measurement uncertainty, evaluated on the basis of our experimental conditions.

On the contrary, in **immersed sample**, the ClO_4^- ion signal intensity rapidly reaches the zero value at about 4 nm. This result put in evidence the crucial role of the EC process in forcing the anions inside the HOPG crystal.

A similar approach in the evaluation of the EC process was followed for the sample treated with H_2SO_4 . In Figure 5.5b the signal intensity variation of the SO_4H^- species is reported. Also in this case, the EC treatment led to a better insertion of the acid molecules and their diffusion throughout the crystal.

As already explained, in the intercalation theoretical model [56], the authors propose that gases molecules, such as CO , CO_2 , and O_2 , develop during the graphite oxidation. Consequently, we decided to search traces of this products in the evolution of O_2 and CO_2H molecular species.

In panels (c) and (d) of Figure 5.5, the behavior of O_2^- and CO_2H^- ion signals for the **intercalated sample** in perchloric and sulfuric acid, respectively, is reported. The signals show an initial increase of intensity, with a maximum within the first 2 nm (sample “surface”). As already seen for the ClO_4^- ion, the signal intensity for both ions remains pretty constant even in the HOPG buried layers. The presence of such ions within the first tens of nanometers in depth confirms the strong oxidative action operated by the acid during the EC treatment, with subsequent formation of related gaseous products. In addition, this result agrees and gives a justification of previous results obtained by Alliata and co-workers [52], where the authors deduce an intercalation depth of about a hundred nm as a consequence of the swelling of the HOPG basal plane, observed by an EC-AFM analysis.

When the **sample** is only **immersed** in the two acids, the O_2^- and CO_2H^- signal behavior starts with a fairly intense value at the surface and it rapidly decreases in intensity.

These results shed a light on the importance of studying the effects of EC treatment in the HOPG buried layers. While the correlation between the surface chemistry and the microscopic analysis has been already discussed, a similar investigation is still lacking for the buried graphite layers. Therefore, we have broadened our interests considering a wide depth range (from 0 to 150 nm) and by combing microscopic and chemical analysis using the ToF-SIMS/AFM set-up.

In Figure 5.6, results from depth profiling experiments on a sample intercalated with HClO_4 are presented.

The C_6^- , ClO_4^- , O_2^- , and CO_2H^- depth profiles, and chemical maps for ClO_4^- at three specific depth values (25 nm, 75 nm, and 150 nm) are shown.

Excluding the C_6^- signal, all the other ion signals taken into account decrease in intensity as a function of the sample depth (top panel). The ToF-SIMS chemical maps are helpful to rationalize the signals behaviour. At $z = 25$ nm, the ClO_4^- 2D distribution, in the bottom-left panel, reveals the presence of widespread blister-like structures with an average diameter ranging from hundreds of nanometers to 1-2 μm , similar to those detected on the very top surface by AFM (Figure 5.4). Interestingly, the number of blisters decreases going downward with respect to the sample surface (compare the bottom panels). This is in agreement with a picture of the intercalation process where the insertion of inorganic acid molecules begins at the crystal surface and gradually decreases going deep inside the buried layers, far beyond the first tens of nanometers. AFM measures performed on the same area at the end of the sputtering process, in Figure 5.7, confirm this picture revealing the existence of a more regular surface at a depth of 150 nm.

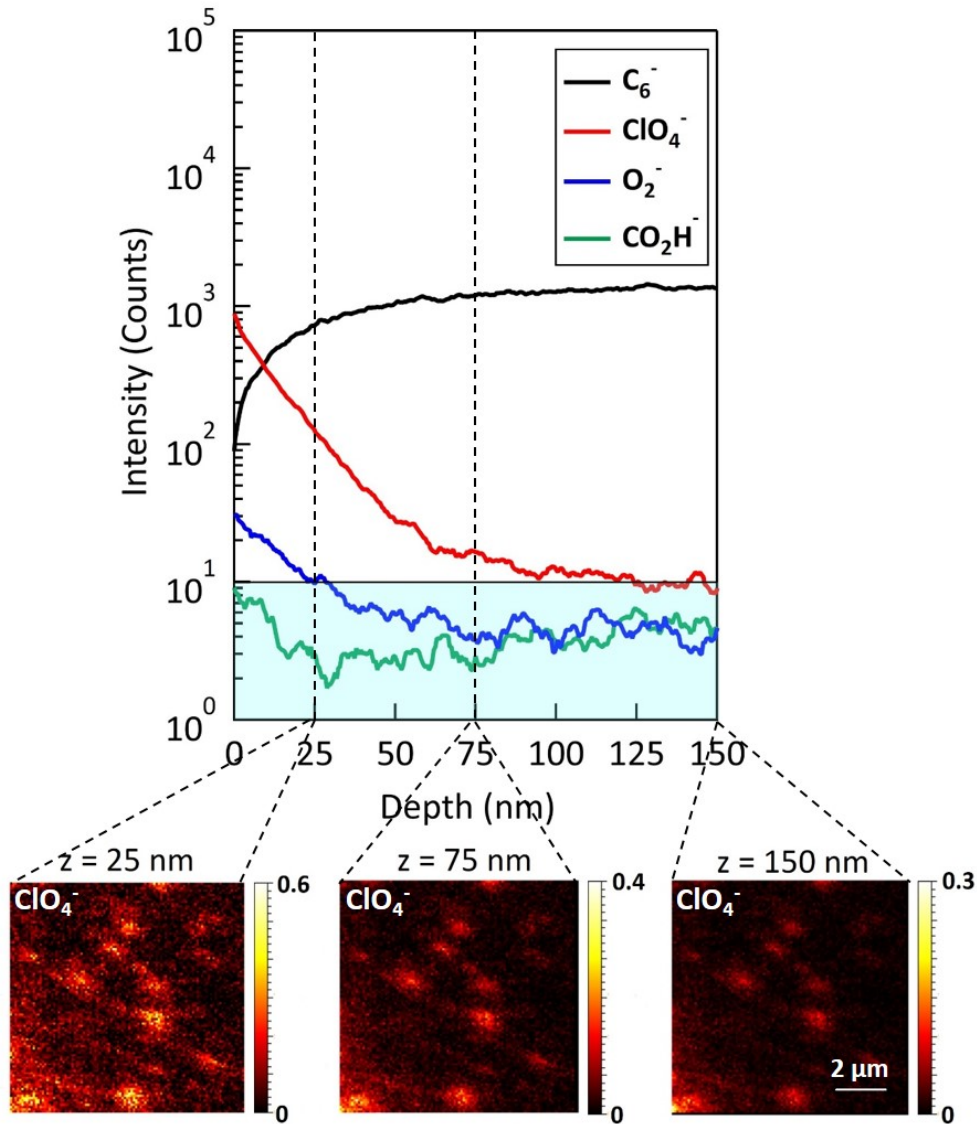


Figure 5.6: ToF-SIMS depth profiles (top panel) and images (bottom panels) of HOPG intercalated in HClO_4 solution. Secondary ion intensities of C_6^- at m/z 72, ClO_4^- at m/z 98.94, O_2^- at m/z 31.99, and CO_2H^- at m/z 44.99 are plotted versus the depth (0-150 nm) in the top panel. The normalised ToF-SIMS images ($10\ \mu\text{m} \times 10\ \mu\text{m}^2$) show the ClO_4^- secondary ion in-plane (XY) distribution at different depths (z values): $z = 25\ \text{nm}$ in the bottom-left panel, $z = 75\ \text{nm}$ in the bottom-center panel and $z = 150\ \text{nm}$ in the bottom-right panel. The scale bar ($2\ \mu\text{m}$), in the bottom-right panel, refers to each chemical maps reported here.

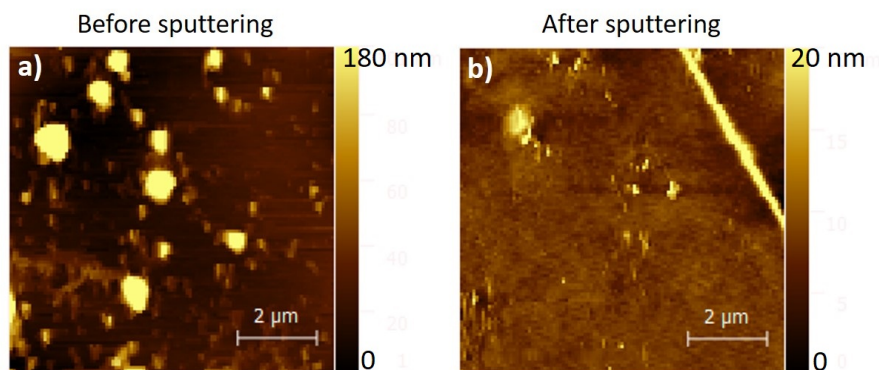


Figure 5.7: AFM images ($10 \times 10 \mu\text{m}^2$) of HOPG intercalated in HClO_4 solution, acquired on the surface sample before the sputtering process of the ToF-SIMS depth profile measure (a) and on the same area, but after the depth profile measure (at $z = 150 \text{ nm}$) (b). For both images, only topography AFM is shown.

3.3 The problem of the graphite crystal defects

Despite being of high quality, HOPG samples have intrinsic defects both on the basal plane and in the crystal bulk. In particular, graphite is constituted by wide grains more or less aligned with the neighbors according to the graphite grade.

An important question concerns the role of such defects in the anion intercalation process. In fact, by using gaps between grains, anions can cover longer paths with respect to those through not-aligned defects present in the different graphite stratified layers. The role of defects can be highlighted observing some results collected on the H_2SO_4 -treated graphite sample.

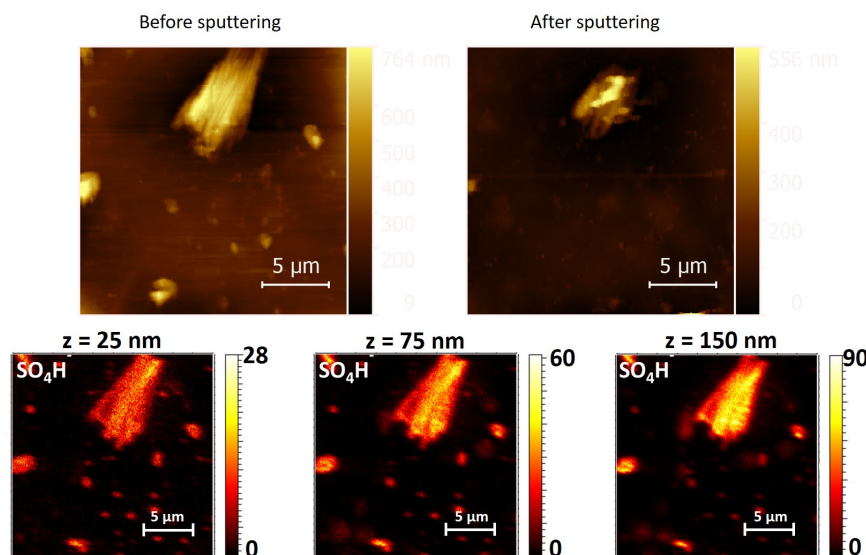


Figure 5.8: AFM images ($20 \times 20 \mu\text{m}^2$) of HOPG intercalated in H_2SO_2 solution, acquired on the surface sample before the sputtering process of the ToF-SIMS depth profile measure (a) and on the same area, but after the depth profile measure (at $z = 150 \text{ nm}$) (b). Bottom panels: Normalised ToF-SIMS images ($20 \times 20 \mu\text{m}^2$) show the SO_4H^- secondary ion XY distribution at different $z = 25 \text{ nm}$ (bottom-left), $z = 75 \text{ nm}$ (bottom-center) and $z = 150 \text{ nm}$ (bottom-right).

In Figure 5.8, AFM (top panels) and ToF-SIMS chemical maps of the SO_4H^- ion as a function of the depth are shown in a region where a large defect is present. Bright areas, symptoms of the presence of the SO_4H^- ions, highlight both some blisters and

a trapezoidal crystal defect. Nonetheless, while the SO_4H^- ion signal is progressively reduced on blisters at deeper layers, the crystal defect is even more brighter with respect to $z = 25$ nm. This result gives a definitive proof that defects are preferential sites for anions thickening and intercalation.

Clear phenomena of segregation were also observed in other areas of the H_2SO_4 -treated graphite samples. An example is given in Figure 5.9. In the left panel a very particular SO_4H^- ion signal trend, collected from a portion ($100 \times 100 \mu\text{m}^2$) of the HOPG surface analysed for 150 nm in depth, is reported. Six points on the depth profile are marked, corresponding to the six ToF-SIMS images on the right. These images show the distribution of the SO_4H^- ion on the HOPG XY plane (perpendicular to the sputtering direction), at the corresponding depth.

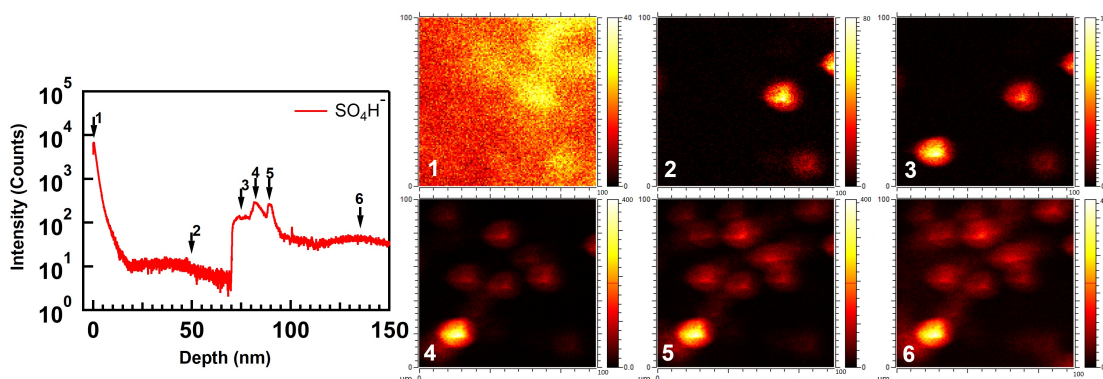


Figure 5.9: ToF-SIMS depth profile (left panel) and images (right panels) of HOPG intercalated in H_2SO_4 solution. Secondary ion intensity of SO_4H^- at m/z 96.95 is plotted versus the depth (0-150 nm) in the left panel. The ToF-SIMS images ($100 \times 100 \mu\text{m}^2$) show the SO_4H^- secondary ion XY distribution at the six different depths indicated in the depth profile.

The distribution of the anion from the H_2SO_4 electrolyte is mostly located on the surface (point 1), then showing a rapid decreasing behavior. The diffusive process of the SO_4H^- ion seems to go through a stationary phase at point 2, from 25 to 75 nm. Here, the XY-distribution is no longer uniform but concentrated in well-defined spots of few tens of micrometers. Thereafter, the diffusion is suddenly interrupted and the SO_4H^- ion signal begins to rapidly increase and decrease in intensity (points 3 to 5), while the spotted accumulation pattern of SO_4H^- XY distribution changes. A second stationary phase of the SO_4H^- ion depth profile corresponds to the appearing of grouping high-intensity spots on the HOPG basal plane at 150 nm in depth.

In Figure 5.10, ToF-SIMS images as XY and XZ slices ($z = 35, 55, 70,$ and 75 nm) and two signal intensity profiles were reported for further analysis of the spatial segregation of SO_4H^- ion inside the HOPG layered structure.

In the first 70 nm, SO_4H^- ions can be found again as isolated circular spots with a larger but quite constant diameter of about $20 \mu\text{m}$ on the XY plane. Between 70 nm and 75 nm, such circular spots seem to be more concentrated and distributed all over a few tens of HOPG basal planes. The higher concentration of electrolyte molecules homogeneously dispersed over HOPG basal planes could be responsible for the production of high quantity of O_2^- ions at these depths. An alternative scenario here arises with respect to the current intercalation interpretative model: solvated anions can be segregated in an orderly manner even in the buried layers as it usually happens on the HOPG surface during the EC treatment. As a consequence, all the electrochemical reactions and related products that usually are located at the crystal surface are now

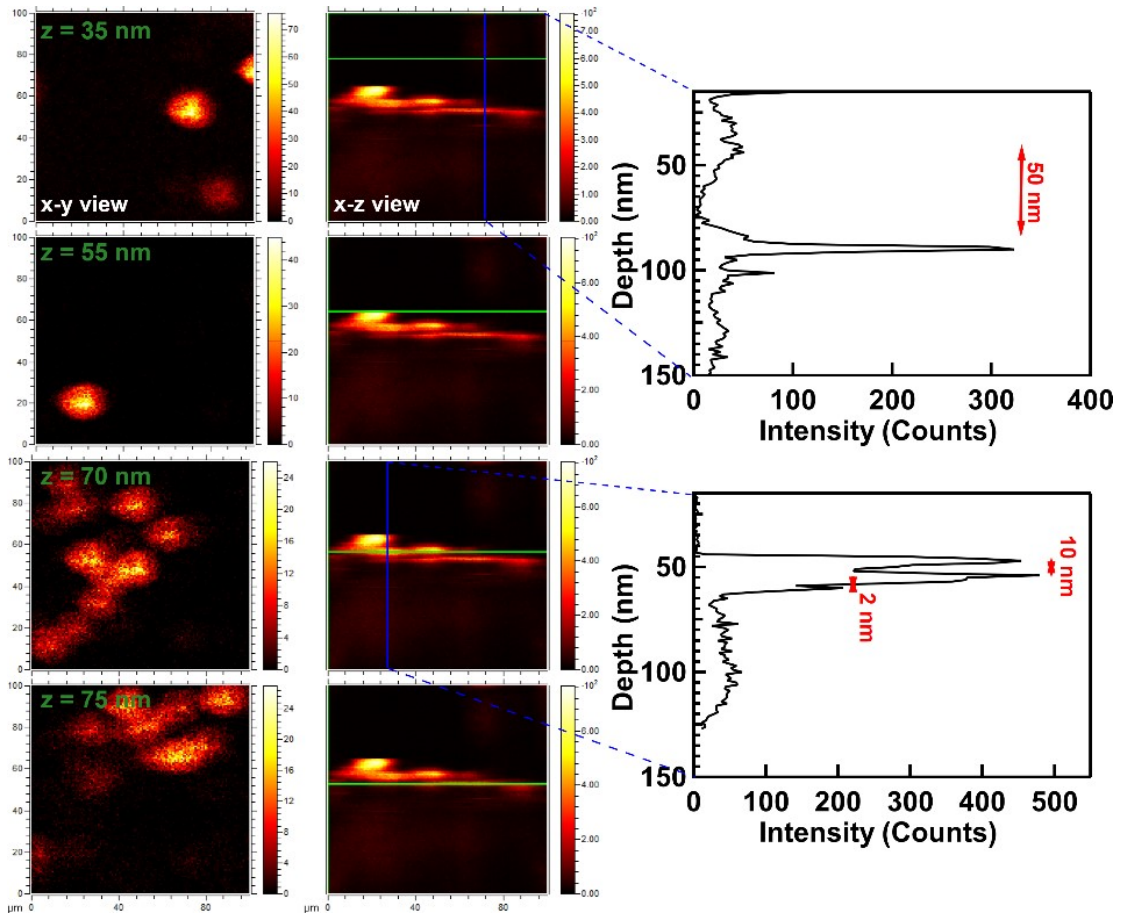


Figure 5.10: XY ($100 \times 100 \mu\text{m}^2$) and XZ ($z = 35\text{-}75$) slices reconstruction of SO_4H^- ion signal from ToF-SIMS depth profile experiments on HOPG intercalated in H_2SO_4 solution. At different depth values ($z = 35, 55, 70, 75$ nm), the XY (in-plane) SO_4H^- ion intensity distribution and the corresponding XZ (vertical cross-section) distribution are shown in the same row, starting from the first top-left panel to the lower-left one. In the two panels on the right, the line scans acquired on the first and the third XZ slice (blue lines) are plotted in depth vs intensity graphs, in order to highlight the dimensional scale of the SO_4H^- ion segregation within the HOPG crystal

generated and placed deeper inside.

All the collected results demonstrated that the electrochemical intercalation of inorganic acids in HOPG is a process not limited to the uppermost layers of the crystal but it concerns the first hundreds of nanometers. This was hypothesized in the past by Murray and coworkers and it actually represents the theoretical model adopted to describe the electrochemical exfoliation of graphene or the insertion of acid molecules in graphitic electrodes. However, this was never experimentally confirmed. The picture of the electrochemical intercalation can be represented as a mechanism where the electrolyte molecules are forced to travel along the crystal for hundreds of nanometers. At the same time, the EC treatment products are not located only at the crystal surface but can move inside the crystal with different diffusion behavior trends. Moreover, a crucial role is played by the large crystal defects. They can be assimilated to preferential lanes for the electrolyte molecules moving and represent a sort of collection point where diffusing molecules can be trapped.

Chapter 6

Low energy ion beam analysis applied to other low dimensional materials

1 Cysteine-modified self-assembling peptides on gold

Molecular self-assembly consists of the spontaneous aggregation of molecules into a well-defined structure guided by noncovalent bonds. The self-assembly strategy is ubiquitous in nature and recently has been proposed as a nature-mimetic strategy in polymer science. Self-assembling peptides are useful in a wide range of applications including protein engineering, nanotechnology, and nanomaterial engineering [138]. In this context, innovative but simple chemical strategies to efficiently modify surfaces by exploiting minor modifications in the bioactive molecule functionalities, for example, introducing cysteine (Cys) as a terminal residue in self-assembling peptides (SAPs), have been designed and tested. A previous study, about preliminary measurements carried out on an SAP modified with a terminal Cys residue (namely, Cys-EAK16-II; sequence: H-Cys-Ala-Glu-Ala-Glu-Ala-Lys-Ala-Lys-Ala-Glu-Ala-Glu-Ala-Lys-Ala-Lys-OH) at the amino end-group, demonstrates that the Cys moiety can induce the formation of a stable and well-organized layer of EAK16-II on polycrystalline gold surfaces, preserving the ability of the SAP to self-assemble [139]. Here, the effectiveness of the surface functionalization in the monolayer regime and the molecular stability of the SAP-Cys were tested by X-Ray Photoelectron spectroscopy (XPS), while the molecular organization attained by the SAP was evaluated in the multilayer regime by means of angular-dependent near-edge X-ray absorption fine structure (AD-NEXAFS) spectroscopy studies.

In this work, the study was extended to the investigation of the influence of the Cys residue position in the SAP chain on the self-assembled film's quality and behavior. Three different Cys-EAK16-II samples, depicted in Figure 6.1, were synthesized: two with one Cys terminal group (either at the amine end group or the carboxyl end group) and one with both terminal groups functionalized with Cys (i.e., a bidentate SAP): Cys-EAK, EAK-Cys, and Cys-EAK-Cys respectively. These peptides belong to a class of peptides able to form β -sheet¹ structures in aqueous solutions because they contain two distinct surfaces, one hydrophilic and the other hydrophobic. In addition, the introduction of one or two residues of Cys gives the possibility to employ these peptides as anchored sequences on gold surfaces.

¹ β -sheet assembly is one of the most common methods to produce oligopeptide-based materials. The β -strands formation occurs when hydrophilic and hydrophobic peptide side chains are positioned on opposite sides of a peptide backbone. Hydrogen bonding between individual strands promotes association into intermolecular β -sheets that contain both a hydrophilic and a hydrophobic face.

Attenuated Total Reflection-Fourier Transform Infrared Spectroscopy (ATR-FTIR), and ToF-SIMS investigation have been performed on the oligopeptide/gold proposed systems.

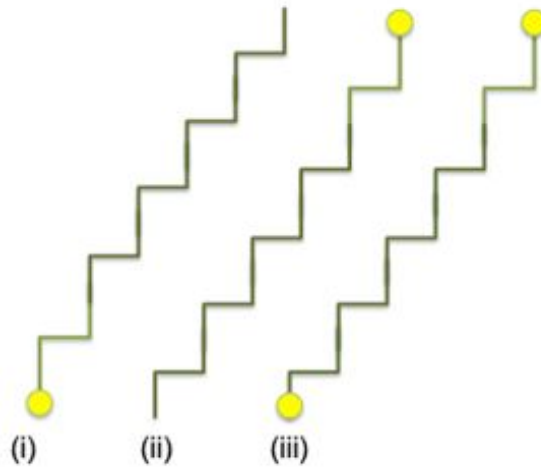


Figure 6.1: Schematic representation of the three proposed systems: (i) Cys-EAK, (ii) EAK-Cys, and (iii) Cys-EAK16-Cys [140].

ToF-SIMS measurements were carried out using the TOF-SIMS instrument, described in Section 5. Positive and negative ion spectra and images were acquired in the Spectrometry mode with Bi_3^{2+} at 30 keV, as the primary beam with a dose density below the static limit, defined in Section 3 and described in Section 6.1. ToF-SIMS depth profiles were collected in the dual beam mode using Bi_3^{2+} (30 keV with current ranging from 0.43 to 0.37 pA), as the primary ion source and a low-energy Cs^+ (250 eV, current: 0.93-0.54 nA) gun, as the etching beam. The area of analysis for chemical mapping and mass spectra was $500 \times 500 \mu\text{m}^2$, whereas the depth profiling analysis area was of $100 \times 100 \mu\text{m}^2$, placed at the center of the sputtered region ($300 \times 300 \mu\text{m}^2$). The 2D maps were acquired at a lateral resolution of approximately $1/1.9 \mu\text{m}$. Ion images were normalized to the total ion image. The cycle time of the ToF analyzer was set to 285 μs , allowing the acquisition of the spectra in the mass range of $1 \leq m/z \leq 7000$. Positive and negative mass spectra were calibrated using H^+ , H_2^+ , C^+ , CH^+ , CH_2^+ , CH_3^+ , and Au_3^+ peaks and C^- , CH^- , CH_2^- , CH_3^- , OH^- , Au^- , and Au_3^- peaks, respectively. Six measurements in different areas of the samples were collected in both polarities in order to perform reliable statistical analysis on the datasets. All ToF-SIMS findings were acquired, calibrated, pre-processed, and exported for further analysis. For the statistical analysis, peaks were manually selected from mass spectra. Characteristic amino acid fragment ions [141] and some ion peaks of interest related to cysteine and the gold substrate are listed in Table 6.1.

ATR-FTIR measurements were performed with an FTIR interferometer equipped with a mid- and far-IR-capable diamond ATR accessory. The spectra were collected in the range between 400 and 4000 cm^{-1} with a resolution of 8 cm^{-1} , a zero-filling factor of 2, and the co-addition of 300 scans. After the data acquisition, the air background spectrum, obtained before each sample spectrum acquisition, was subtracted from the spectra.

Mass (m/z)	Formula	Source
28.02	CH_2N^+	Lys
29.04	C_2H_5^+	Lys
30.03	CH_4N^+	Lys
31.02	CH_3O^+	Lys
39.03	C_3H_3^+	
41.04	C_3H_5^+	Lys
42.04	$\text{C}_2\text{H}_4\text{N}^+$	Ala
43.02	$\text{C}_2\text{H}_3\text{O}^+$	Lys
43.06	C_3H_7^+	Lys
44.05	$\text{C}_2\text{H}_6\text{N}^+$	Ala
44.98	CHS^+	Cys
45.03	$\text{C}_2\text{H}_5\text{O}^+$	Lys
54.05	$\text{C}_3\text{H}_6\text{N}^+$	Lys
58.07	$\text{C}_3\text{H}_8\text{N}^+$	Glu
58.99	$\text{C}_2\text{H}_3\text{S}^+$	Cys
71.05	$\text{C}_4\text{H}_7\text{O}^+$	Lys
76.02	$\text{C}_3\text{H}_6\text{SN}^+$	Cys
83.05	$\text{C}_5\text{H}_7\text{O}^+$	Glu
84.04	$\text{C}_4\text{H}_6\text{NO}^+$	Glu/Lys
84.08	$\text{C}_5\text{H}_{10}\text{N}^+$	Lys
17.00	OH^-	
26.01	CN^-	
31.97	S^-	
32.98	HS^-	
33.97	$^{34}\text{S}^-$	
196.97	Au^-	
228.93	AuS^-	
229.94	AuHS^-	
393.91	Au_2^-	
590.87	Au_3^-	

Table 6.1: Positive and negative ion species selected from ToF-SIMS Spectra of Cysteine-Modified EAK16-II on Gold [140].

1.1 Results

ATR-FTIR Spectroscopy. The ATR-FTIR spectra of Cys-EAK-Cys and EAK-Cys samples in the range of 450-4000 cm^{-1} are reported in Figure 6.2. In the 1400-1800 cm^{-1} range (the inset in Figure 6.2), the ATR-FTIR spectra features of Cys-EAK-Cys and EAK-Cys are in good agreement with the spectra already reported for the simple EAK sample [139]. In particular, the amide-I band², resulting from C=O stretching vibration, is located at 1628 cm^{-1} with a well-defined shoulder of approximately at 1680 cm^{-1} . These features are typical of the antiparallel β -sheet conformation of the peptide backbone [142], as already evidenced for EAK [139]. On the contrary, the absorption peak at 2553-2556 cm^{-1} , indicating the S-H stretching vibration of cysteine, is not present in our FTIR spectra. This characteristic peak is usually difficult to detect by ATR-FTIR in thin films. In this case, probably, we do not have a large enough concentration of SH molecules to observe it.

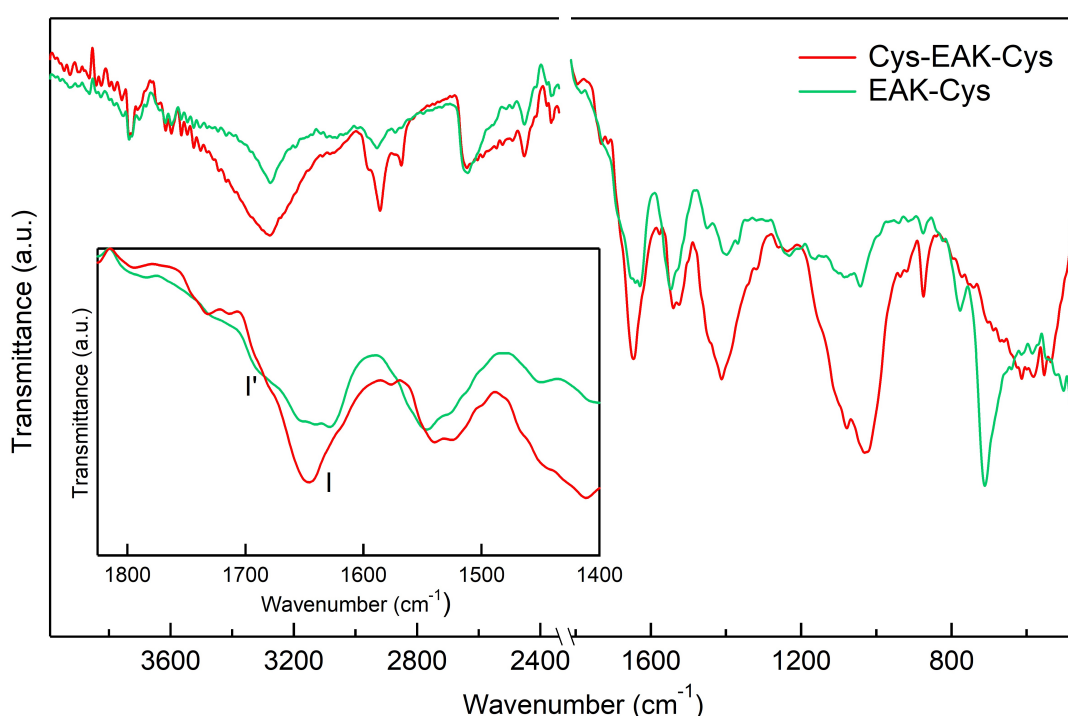


Figure 6.2: ATR-FTIR spectra of Cys-EAK-Cys and EAK-Cys samples [140].

Static ToF-SIMS - Surface chemistry The main results obtained by static TOF-SIMS experiments on Cys-EAK-Cys, Cys-EAK, and EAK-Cys monolayers are summarized in Figure 6.3. Here, the mean values of the normalized peak intensities for selected positive ions of Cys-EAK-Cy, Cys-EAK, and EAK-Cys are reported in Figure 6.3a, 6.3b, and 6.3c, respectively. The mean value of the peak intensities of the amino acid fragment ions was calculated considering the sum of the peak intensities of their characteristic fragment ions reported in Table 6.1.

The resultant values should be representative of the surface chemistry of the self-assembled monolayers when anchored on the Au/Si(111) surface. The results obtained from ion bombardment in the static regime can already give us some information about

²Amide-I band is one major band of the protein infrared spectrum. It is mainly associated with the C=O stretching vibration (70-85%), and is directly related to the backbone conformation.

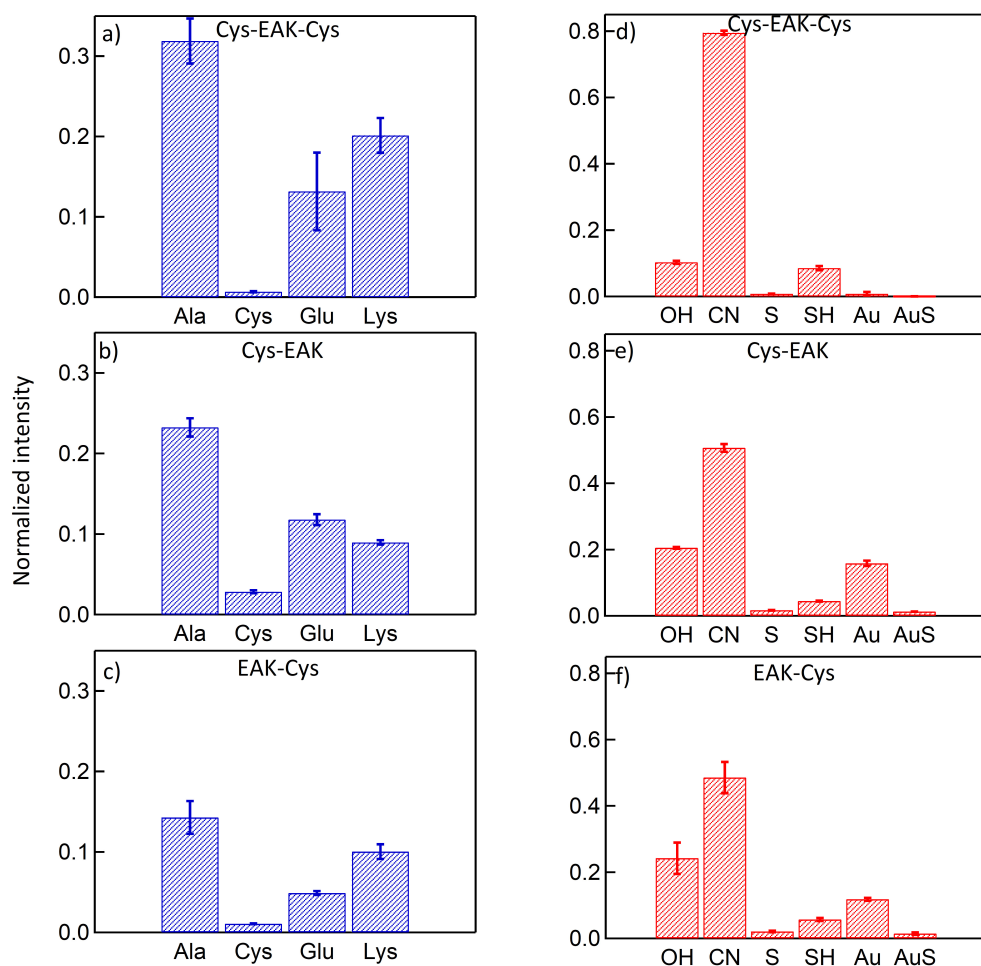


Figure 6.3: Normalized mean values of peak intensities for selected secondary ions from ToF-SIMS positive and negative spectra acquired on (a, d) Cys-EAK-Cys, (b, e) EAK-Cys, and (c, f) Cys-EAK samples. The mean value for each amino acid was calculated by summing the peak intensities of all its related characteristic fragment ions. Error bars represent the standard deviation calculated acquiring six spectra from each sample [140].

Sample	Ala/Cys	Glu/Cys	Lys/Cys	CN ⁻ /S ⁻	AuS ⁻ /Au ⁻
Cys-EAK	7.74	4.55	3.47	27.35	0.12
EAK-Cys	13.32	4.56	8.43	23.01	0.12
Cys-EAK-Cys	47.51	19.61	29.40	97.51	0.08

Table 6.2: Peak intensity ratios for Ala, Lys, and Glu to Cys coming from positive ion mass spectra of Cys-EAK, EAK-Cys, and Cys-EAK-Cys samples [140].

the SAP geometry and the degree of substrate coverage. In Table 6.2, the ratios of the intensities of the Ala, Lys, and Glu peaks to the Cys peaks from the positive ion mass spectra for the three samples are shown. These ratios should be as follows Cys (1), Ala (8), Glu (4), and Lys (4), considering the exact aminoacidic composition. From Table 6.2, the peak intensity ratio values for the Cys-EAK sample are quite similar to the theoretical ones, suggesting that the ion beam easily reaches the entire peptide chain. The assumption of a well-defined molecular orientation presence in the Cys-EAK sample, suggested by the angular-dependent NEXAFS data [139], could be supported by these results. In the EAK-Cys sample, the values of the ratios differ from the theoretical ones; this can be explained with certain changes in the geometrical arrangement, or with a matrix effect, due to the presence of several clusters of salt ions, such as sodium (Na⁺) and potassium (K⁺), detected on the surface of the samples, as shown in the chemical maps in Figure 6.4.

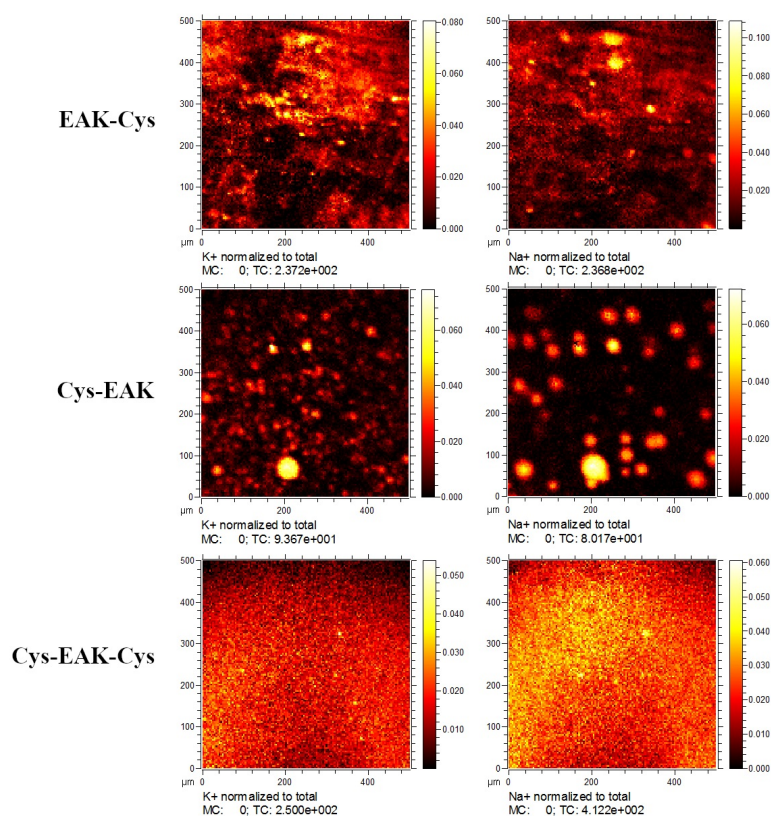


Figure 6.4: ToF-SIMS images obtained in positive ion mode from Cys-EAK (top), EAK-Cys (middle), and Cys-EAK-Cys bottom) samples for 2D chemical maps of Na⁺ and K⁺ ion signal [140].

It is well known that the ionization yield of the target fragments may be influenced by matrix effects. In particular, salts like potassium and sodium can form adducts with

the organic molecules, resulting in a promotion of ionization. The Cys-EAK sample shows well-defined clusters of salt ions, while in EAK-Cys, they are spread all over the sample surface. For this latter sample, the irregular distribution of salt ions may have slightly influenced the ionization yield. For what concerns the Cys-EAK-Cys sample, the surface distribution of the salt ions seems to be pretty homogeneous. It is interesting to note that, for the Cys-EAK-Cys sample, the ratios in Table 6.2 are up to five times greater than the expected values. A different arrangement of the peptide chains, or a different degree of substrate coverage, could explain this discrepancy. In Figure 6.3d-f, normalized peak intensities of OH^- , CN^- , S^- , SH^- , Au^- , and AuS^- ions from Cys-EAK-Cys, Cys-EAK, and EAK-Cys samples are reported. The following CN^-/S^- and AuS^-/Au^- ratios are reported in Table 6.2. The CN^-/S^- peak ratios for Cys-EAK and EAK-Cys samples are quite consistent with the nominal value of CN bonds (i.e., 21) present in the peptide chain. Again, in the Cys-EAK-Cys sample, the CN^-/S^- ratio is almost five times greater than expected. The detection, on the top of the SAPs, of cysteine fragment ions (Figure 6.3b,c), and the presence of the SH^- ion in the negative ion mass spectra (Figure 6.3e,f), could support the hypothesis of an antiparallel β -sheet configuration for Cys-EAK and EAK-Cys samples. In the Cys-EAK-Cys sample, the signal intensity of the secondary ions generated from the gold substrate (Au^- and AuS^-), is lower than in Cys-EAK and EAK-Cys (Figure 6.3d-f). Furthermore, the AuS^-/Au^- ratio, in Table 6.2, supports the presence of a multilayer or a higher degree of surface coverage. This is in excellent agreement with the thicknesses estimation of the sample from XPS measurements [140].

ToF-SIMS imaging - SAPs 2D spatial distribution In Figure 6.5, the chemical maps of specific amino acid fragment ions of Cys-EAK, EAK-Cys, and Cys-EAK-Cys samples, are shown. The 2D-distributed signals were obtained by summing the ion images of all characteristic fragment ions for each amino acid. The positive total ion image of the EAK-Cys sample (Figure 6.5b.1) shows widespread inhomogeneity, probably due to the presence, over the analysed surface, of residual chemical reagents used in the SAP synthesis. On the contrary, the total ion distribution for Cys-EAK and Cys-EAK-Cys samples (Figure 6.5a.1, c.1) seems to be more homogeneous. The lower signal intensity spots, in the latter two mentioned maps, is probably related to the presence of mesoscopic defects on the Au substrate. Cysteine, alanine, glutamic acid, and lysine fragment ions are distributed all over the entire analysis area.

It is possible to make similar considerations about the negative ion maps, shown in Figure 6.6. The total ion images (Figure 6.6a.1, b.1, c.1) highlight some topographic defects due to a not perfectly flat substrate. In general, negative ions appear homogeneously distributed. It is noteworthy that the signal intensity for Au^- and AuS^- ions is lower for Cys-EAK-Cys, compared to the other two samples. Such a difference can be considered as further evidence of a thicker layer formation for the Cys-EAK-Cys sample [140].

Dynamic ToF-SIMS - SAPs Molecular architecture In order to follow the in-depth evolution of the SAP layer molecular assembly, TOF-SIMS depth profile measurements were carried out, and the results are shown in Figure 6.7. In ultra low-energy bombardment conditions (Cs^+ at 0.25 keV), it was possible to study hybrid organic-inorganic architectures with a depth resolution lower than 1 nm [136]. At first glance, the profiles for EAK-Cys and Cys-EAK are different from those obtained from the Cys-EAK-Cys sample. Referring to the EAK-Cys sample (Figure 6.7a), the signals of NH^- and CHO^- ions are present on the surface and then slowly decrease in intensity. The Au^- ion sig-

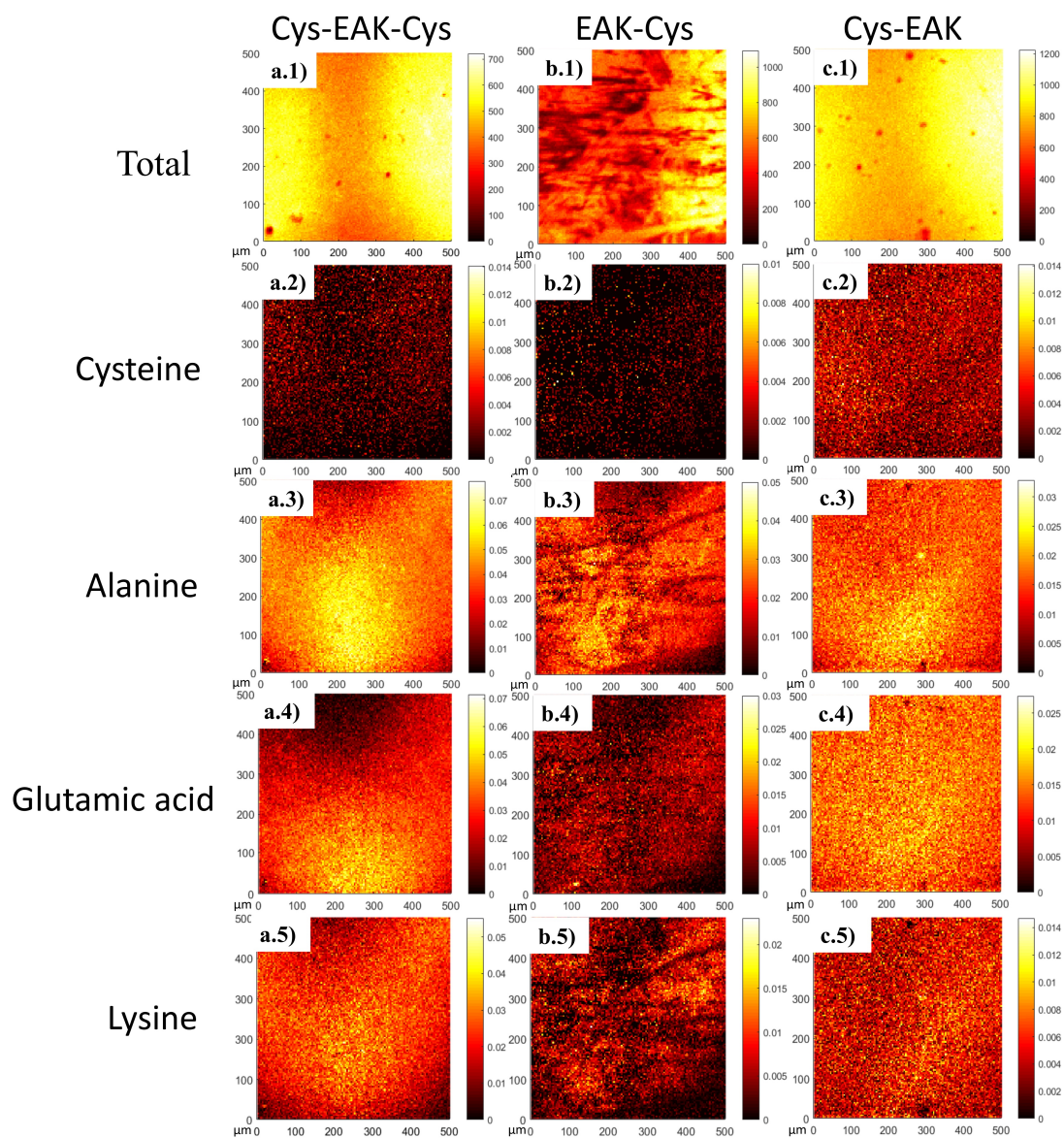


Figure 6.5: TOF-SIMS images obtained in positive ion mode from (a.1-a.5) Cys-EAK-Cys, (b.1-b.5) EAK-Cys, and (c.1-c.5) Cys-EAK samples. The 2D chemical maps of the amino acid signals were obtained by summing the ion images of all characteristic fragment ions for each amino acid reported in Table 6.1. The total counts maps of each sample are also reported [140].

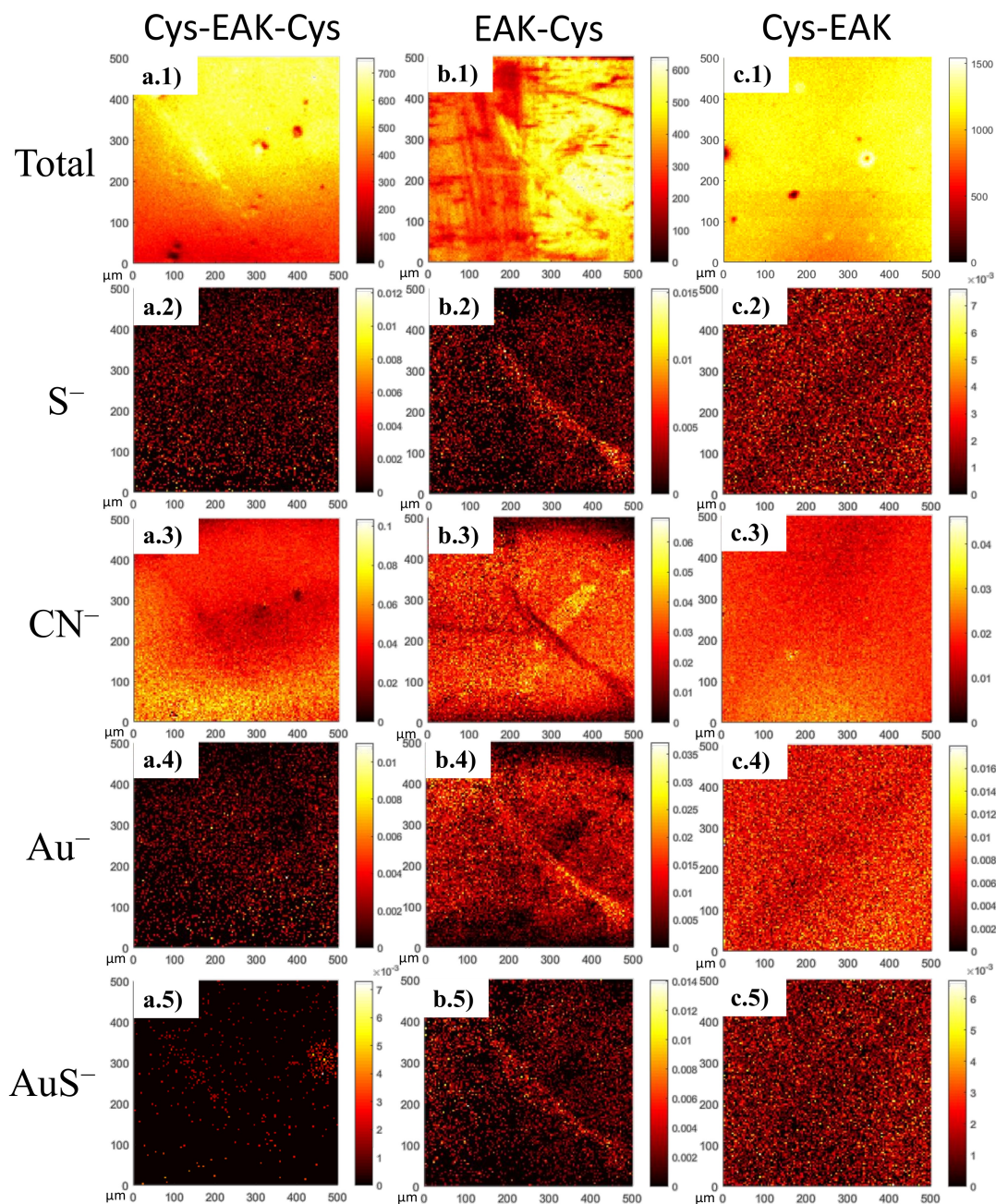


Figure 6.6: TOF-SIMS images obtained in the negative ion mode from (a.1-a.5) Cys-EAK-Cys, (b.1-b.5) EAK-Cys, and (c.1-c.5) Cys-EAK samples. The 2D chemical maps of S^- , CN^- , Au^- , AuS^- , and the total counts are reported for each samples [140].

nal is already detectable at the start of the sputtering process; the signal intensity then rises up reaching a steady state corresponding to the gold substrate.

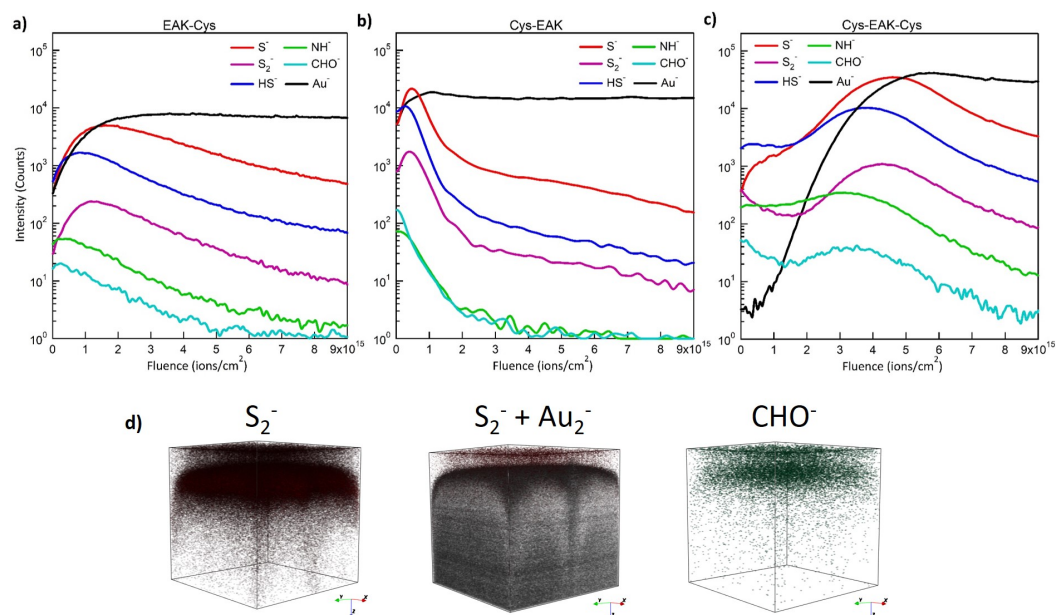


Figure 6.7: ToF-SIMS depth profiling of (a) EAK-Cys, (b) Cys-EAK, and (c) EAK-Cys-EAK samples. (d) 3D ion map reconstruction of S_2^- , $Au_2^+ + S_2^-$, and CHO^- for the Cys-EAK-Cys sample [140].

Finally, it is also interesting to note the different behavior of the curves representing S^- and S_2^- ions compared to the curve for the SH^- ion. All the three signals first increase in intensity, then drop with slow dynamics. However, the edge of the SH^- ion curve seems to be shifted toward the surface. This behavior difference can be more clearly appreciated in the Cys-EAK sample, in Figure 6.7b, and it could be interpreted as an effect of the antiparallel β -sheet conformation of the peptide chain. In the depth profile of the Cys-EAK sample it is also possible to better identify the SAP/gold interface: the S^- ion signal drops dramatically when the Au^- ion signal reaches a steady state. Otherwise, in Figure 6.7c, The Au^- ion signal of Cys-EAK-Cys sample is almost undetectable at the start of the sputtering process, while the CHO^- and NH^- ion signals are present on the surface, then drop and rise up, decreasing finally in intensity in correspondence of the gold substrate. Similar profiles were also detected for HS^- and S_2^- ions. These particular behaviors of the ion profiles support the presence of a bilayer-like molecular arrangement. The bilayer-like structure can be better visualized using the 3D mapping, as shown in Figure 6.7d. The S_2^- ion 3D map is depicted in red (left), and it is mapped also in combination with the Au_2^- ion (gray). In addition, the CHO^- ion signal was reported to highlight the presence of a double layer.

2 Reactive dissolution of organic nanocrystals: porphyrin thin films deposited on HOPG

Controlling the morphology of advanced organic materials is a key task for their applications in different fields, ranging from the fabrication of organic electronic devices [143], sensors [144], as well as applications to the biomedical field [145]. Furthermore, the so-called "green-conversion" includes, nowadays, the development of novel protocols and techniques for waste treatment. Chemical wastes deriving from industrial

and power-station processes, which involve organic crystals, can be very hazardous for the environment. Studying their dissolution mechanism, both theoretically and experimentally, represents a mandatory step in the critical task of their disposal. Most of the studies are focused on millimeter scale length, from which, for example, one could learn the crystal dissolution rate. Here, etch-pit³ formation is recognized as the ultimate mechanism of crystal dissolution.

In this work [146], results from ToF-SIMS measurements contributed to the detailed investigation, on the submicrometer scale range, of the dissolution process of porphyrin thin films, deposited on the basal plane of HOPG. Among many organic materials, porphyrin molecules represent building-blocks for functional material [147], whose optical/electronic properties can be modulated electrochemically or by the proper control of pH and solvent. For these reasons, such films constitute a model system to unveil the dissolution mechanism of organic nanocrystals, more in general. The common idea that, from a thermodynamic point of view, dissolution is the reverse process of growth may explain why crystal dissolution received less interest than crystal growth. A first tentative of studying dissolution as an independent process was made by F. C. Frank in the 50s focusing on germanium crystals [148]. According to Frank's model, etch-pit form when undersaturation overcomes a critical value. Recently, it was pointed out that the state of art in etch-pit-controlled crystal dissolution is focused on millimetric-scale crystals, while theoretical calculations (in view of having computable data) require nano-sized crystals on surfaces with different roughness [149].

A model system, based on porphyrin nanocrystals immersed in a diluted sulfuric acid solution, was studied by combining different surface, including ToF-SIMS, and bulk-sensitive techniques. It was found that etch-pit formation only affects organic nanocrystals at specific pH. The change of the pH offers the possibility to explore unprecedented ranges of undersaturation, revealing the strong non-linear character of the dissolution process (i.e. different phases), especially in relation to the crystal morphological evolution.

Z-grade HOPG was used as substrate for porphyrin deposition. The substrate surface (0.2 cm²) was mechanically exfoliated before each experiment by mean of an adhesive tape. A solution of 1 M H₂SO₄ was prepared diluting a concentrated H₂SO₄ solution and de-aerated by bubbling pure Ar; 1mM solutions were obtained diluting the original 1 M solution, without further purifications. Meso-tetra-phenyl porphyrin (H₂TPP) film is grown by physical vapor deposition (PVD). The growth rate was set at 0.4 - 0.5 Å/s and the source temperature at approximately 350 ° C. A good compromise, adopted in this work, between a great number of crystals (for statistical analysis) and a thin molecular film is represented by 20 nominal layers.

ToF-SIMS measurements were carried out using the TOF-SIMS instrument, described in Section 5. Positive and negative ion spectra and were acquired in the high-current bunched mode using Bi₃²⁺ at 30 keV (target current 0.3 pA), as the primary beam with a dose density below the static limit, defined in Section 3 and described in Section 6.1. The sample was held at room temperature during the ion bombardment. The cycle time of the ToF analyzer was set to 100 μs, allowing the acquisition of the spectra in the mass range of $1 \leq m/z \leq 850$. Negative mass spectra were calibrated using C⁻, CH⁻, C₂⁻, C₂H⁻, C₄⁻, and C₆⁻. The resolution achieved (m/Δm) was equal to 12000 at mass 72 (C₆). Five measurements in different areas of the samples were collected in both

³Etch-pits are deep holes crystallographically oriented with respect to the main axis of the crystal.

polarities in order to perform reliable statistical analysis on the datasets. All ToF-SIMS findings were acquired, calibrated, pre-processed, and exported for further analysis. For the statistical analysis, peaks were manually selected from mass spectra. Three different scaling options were tested for scaling mass spectra: normalization to the total ion dose, total counts, and sum of selected peaks. Here, ToF-SIMS spectra were normalized to the sum of selected peaks characteristic of the porphyrin fragmentation. ToF-SIMS images were acquired using 30 keV Bi_3^{2+} primary ions, rastered over 256×256 pixels with a field of view of the image of $(500 \times 500) \mu\text{m}^2$. 2D maps were acquired with a lateral resolution of $1.9 \mu\text{m}$, approximately. Ion images were normalized to the total ion image.

2.1 Results

AFM image of the pristine H_2TPP surface morphology is shown in Figure 6.8a [146]. The pristine surface morphology is characterized by an ensemble of many crystals (approximately 30 - 50 crystals/ μm^2), showing many edges at 90° and is organized in domains with different orientations. The film roughness is approximately 8 nm.

When immersed in acidic media, free-base porphyrins undergo a protonation. The reactive dissolution of the porphyrin crystals is triggered, with a kinetic dependent on the acid concentration (pH). Etch-pit formation is expected on the nanocrystals surface. In agreement with this scenario, once placed in the diluted sulfuric acid, H_2TPP films undergo a significant morphological change with a clear trend as a function of the pH [146].

At pH = 3, nanocrystals show characteristic etch-pits well aligned with the crystal edges (Figure 6.8b). The presence of etch-pits clearly indicates that molecules are progressively removed from the crystal and that, even at pH = 3, undersaturation value is beyond the critical point for effective dissolution [146].

Instead, at pH = 0, crystals undergo to an abrupt dissolution (Figure 6.8c). However, the surface morphology is significantly different from the pristine HOPG, indicating that a residual layer of porphyrins is still present on the surface [146].

AFM images were also acquired at intermediate pH values (pH = 1, 2), at which wider etch-pits are expected (Figure 6.9). Surprisingly, nanocrystals do not show wider etch-pits after the immersion in the solution at pH = 2. Indeed, after waiting few minutes, etch-pits abruptly disappear and nanocrystal surfaces are observed to be decorated by bulges (Figure 6.9b), whose density is comparable to that of the etch-pits. These bulges are similar to those observed immediately after the sample immersion in the pH = 1 solution (Figure 6.9c). The morphological change from etch-pit to bulge structures is probably due to a dissolution kinetic enhancement. In fact, the level of undersaturation of the system increases as the pH decreases, shifting the dissolution plateau [146].

In the light of the AFM results, an in-depth investigation of the chemistry of dissolution becomes necessary. An explanation for the chemical process, that justifies the surface morphological changes, was explored by low-energy ion bombardment experiments conducted on the pristine H_2TPP sample and H_2TPP samples immersed in 1 and 100 mM solutions. Secondary ions coming from the H_2TPP characteristic fragmentation process were detected [146].

In Figure 6.10, the results for the as grown sample (gray solid line), the sample where stable etch pits have been found (pH = 3, blue dotted line), and the sample characterized by bulges (red dashed line) are presented.

In order to interpret the changes in the surface chemistry of the sample, we monitored the intensity evolution of two of the most abundant ion peaks at high masses ($\text{C}_{44}\text{H}_{30}\text{N}_4^-$

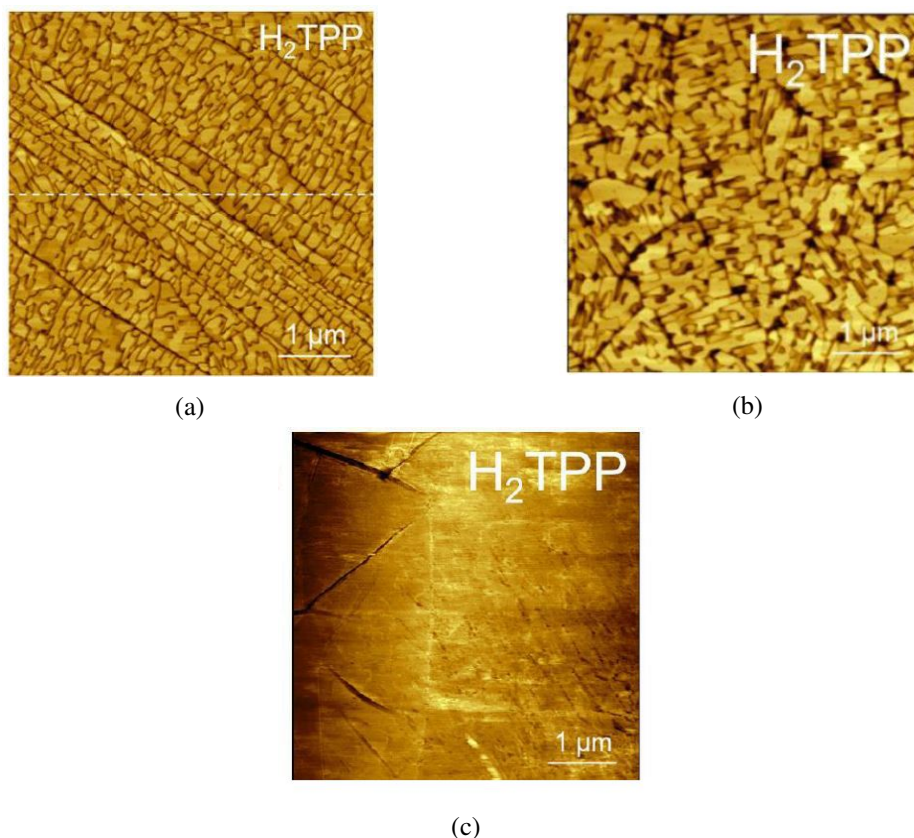


Figure 6.8: AFM image of (a) the pristine H_2TPP , (b) H_2TPP when immersed in diluted sulfuric acid solution of pH = 3, and (c) H_2TPP when immersed in diluted sulfuric acid solution of pH = 0 [146].

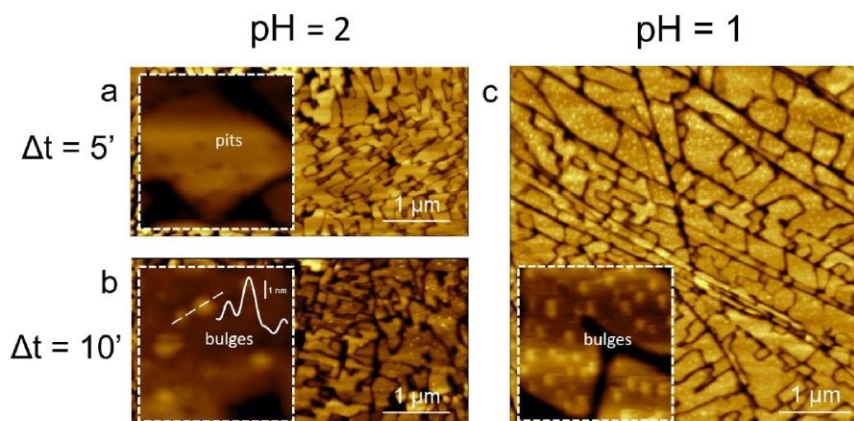


Figure 6.9: AFM images comparison of H_2TPP when immersed in diluted sulfuric acid solution of pH = 2 (panels a and b) and pH = 1 (panel c). In the latter case, no further evolution as a function of time is observed. Insets: blow-ups of the sample surface characterized by etch-pits (panel a) or bulges (panels b and c) are reported [146].

at 614.24 m/z and $C_9H_5N_2^-$ at 141.04 m/z) and two ion peaks at lower masses (C_5N^- at m/z 74.00 and NH^- at m/z 15.01). These ion peaks were selected as representatives of the porphyrin macrocycle. Variations in signal intensity of the two ion peaks at high masses could indicate a degradation of the macrocycle, while changes in signal intensity of the low-mass peaks could give information about the degradation of the pyrrole unit. The plots in Figure 6.10 show the changes in signal intensity of the $C_{44}H_{30}N_4^-$, H_2TPP molecular ion peak, and $C_9H_5N_2^-$ fragment ion (top panels, left and right, re-

spectively), the latter probably coming from the fragmentation of two pyrrole units of the tetrapyrrolic macrocycle.

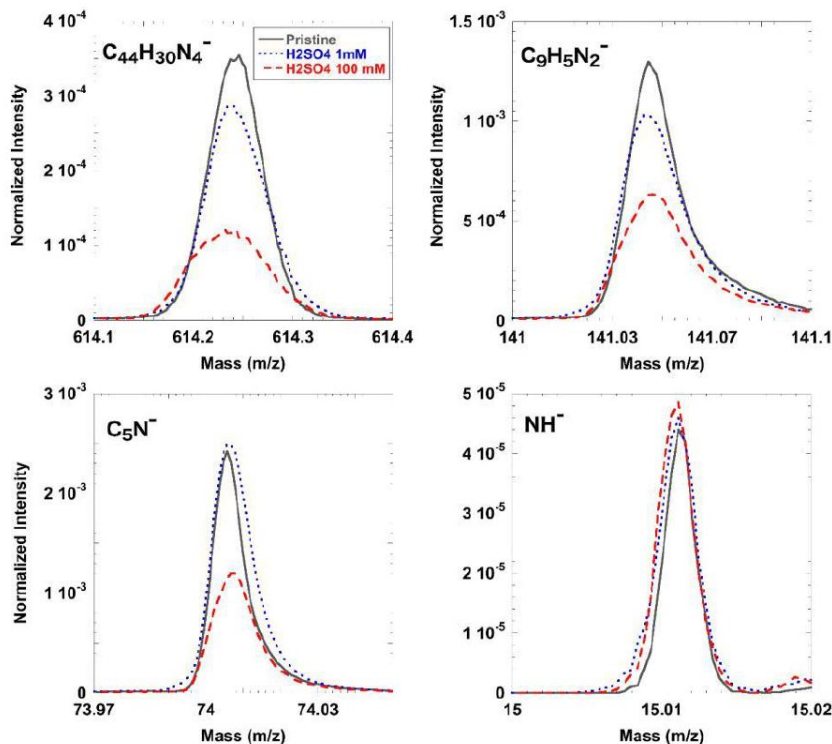


Figure 6.10: Comparison of normalized ToF-SIMS negative ion peaks from pristine H₂TPP sample (gray solid line), H₂TPP sample immersed in 1mM (blue dotted line) and 100mM (red dashed line) sulfuric acid solution. Changes in ion peak intensity for $C_{44}H_{30}N_4^-$ (m/z 614.24), $C_9H_5N_2^-$ (m/z 141.04), C_5N^- (m/z 74.00), and NH^- (m/z 15.01) are represented, respectively [146].

For both ions, the signal intensity drops progressively with increasing concentrations of sulfuric acid. On the other hand, this trend seems to change exploring the lower mass range. The peak intensity of the C_5N^- signal acquired on the 1 mM-sample is quite similar to the pristine H₂TPP (panel at the bottom left). The signal intensity of NH^- is substantially equivalent for all the samples (panel at the bottom left). If we consider the ratio between NH^- ion signal and the H₂TPP molecular ion peak ($C_{44}H_{30}N_4^-$), it becomes evident that the availability of NH^- fragment ions in the volume of analysis is greater for H₂TPP film immersed in sulfuric acid solution than for pristine H₂TPP sample. This result, together with the gradual decrease in intensity of the above-mentioned high mass molecular ion peaks, can be imputed to the aggressive physical-chemical effects of the acid on the porphyrin macrocycle [146]. The picture of the dissolution mechanism is further corroborated by the chemical maps collected from the H₂TPP sample treated with 100 mM sulfuric acid solution, in Figure 6.11.

Here, the effects of the diluted sulfuric acid can be appreciated on the micrometer scale by observing the total ion image (panel at the top left), the chemical maps of OH^- (panel at the top right) and the $H_3S_2O_8^-$ map (panel at the bottom left). In particular, the distribution of the strong $H_3S_2O_8^-$ ion signal clearly highlights the areas where the acid has reacted with the porphyrin film surface. At the same time, and in the same areas, the $C_{44}H_{30}N_4^-$ ion image shows significantly lower signal intensity. In other words, the chemical map of the H₂TPP molecular ion peak seems to be complementary to the sulfuric acid map; this effect is more evident comparing the chemical map of the

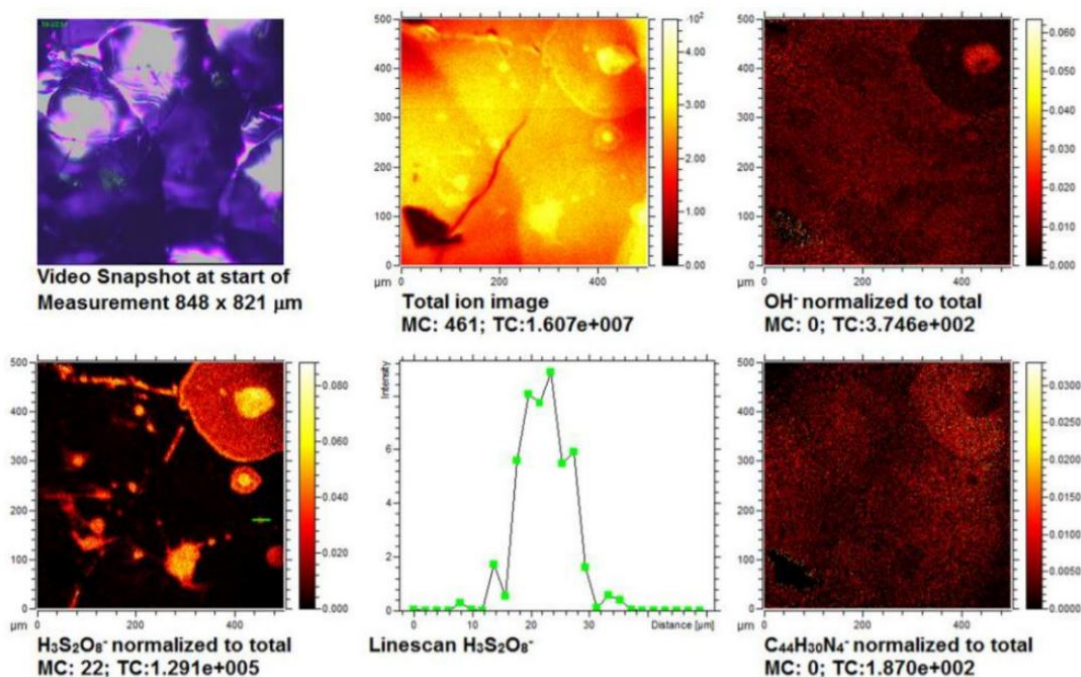


Figure 6.11: Negative ion images from H_2TPP sample immersed in 100mM sulfuric acid solution. (Top left) Video snapshot from the built-in microcamera of the ToF-SIMS apparatus showing the sample surface ($848 \times 821 \mu\text{m}^2$). (Top center) total negative ion image. Negative ion images of: (Top right) OH^- m/z 17.00, (bottom left) $\text{H}_3\text{S}_2\text{O}_8^-$ m/z 194.93, (bottom center) linescan of $\text{H}_3\text{S}_2\text{O}_8^-$ ion distribution; the x-axis is highlighted in green in the related chemical map. (Bottom right) $\text{C}_{44}\text{H}_{30}\text{N}_4^-$ m/z 614.24 [146].

H_2SO_4^- -related peak (OH^-) to the $\text{C}_{44}\text{H}_{30}\text{N}_4^-$ map. The circular regions on the images have different sizes ranging from tens of microns, as shown in the line scan of $\text{H}_3\text{S}_2\text{O}_8^-$ ion distribution (bottom center panel), up to hundreds of microns.

The molecular fragmentation observed at the ToF-SIMS analysis confirms that, when protonated, H_2TPP molecule becomes sufficiently soluble in the aqueous media to be removed from the crystal (reactive dissolution). Moreover, at $\text{pH} = 3$ the presence of etch-pits on the crystal surface suggests that the Frank dissolution process is active also for nanocrystals. Conversely, if the pH is further reduced, etch-pit evolution does not represent the ultimate dissolution process. Rather, bulges start to decorate the film surface as observed by the ToF-SIMS imaging analysis.

Conclusions

Tuning the electronic and mechanical properties of materials at the micro and nanoscale ranges is currently a key goal for the technological research activity of the material science sector. Among different fields, molecular intercalation in graphite, for changing its transport properties as electrode in ion batteries or in view of the crystal exfoliation for graphene production, has received increasing interest in the past decade. In this thesis, I provide an accurate picture of the molecular mechanisms that correlate the formation of graphite surface detriment (e.g. blisters) and electrolyte anion intercalation. The model for GIC formation and development proposed by Murray and then adopted by Allia for anion percolation clearly describes dimensional changes occurring during the electrochemical processes. For the first time, this model is improved with the identification and localization at the micrometer scale of the molecular species present on the HOPG surface after the very first stages of graphite intercalation in both perchloric and sulfuric acid aqueous solutions. In the intercalated HOPG samples, the surface distribution of perchlorate and hydrogen sulfate ions gives direct evidence that the anion intercalation happens via surface defects among HOPG crystallites. These results reinforce the hypothesis of a complex intercalation mechanism, where more than one molecular species could be responsible for blister formation and carbon detriment. The penetration depth of the molecular species involved in the intercalation process is monitored and spatially localized by dual beam ToF-SIMS depth profiling experiments at very low energy. Molecular species coming from the electrolyte, as well as oxygen-based molecular fragment ions generated as a consequence of the EC treatment, were revealed and located starting from the HOPG surface and then along the graphitic planes. The picture of the electrochemical intercalation can be now represented as a mechanism where the electrolyte molecules are forced to travel along the crystal for hundreds of nanometers. At the same time, the oxidation products are not located only at the crystal surface but can move inside the crystal. I am convinced that the findings presented and discussed in this thesis could be helpful in the HOPG delamination protocol optimization, in view of a significant enhancement of the industrial and technological graphene production quality and its appropriate exploiting.

As a future perspective of this research, the effects of other electrolytes on layered crystals could be investigated to find a better compromise between anion intercalation and host material dissolution.

Acknowledgments

This work has been partially funded by the Italian Ministry of University and Research in the framework of the Premial Project EOS (Organics Electronics for Innovative Research Instrumentation). Surface Analysis Laboratory, University “Roma Tre” gratefully acknowledges financial support from “Fondazione Roma” (Grant No. 5229441F37). The TOF-SIMS/AFM instrument was financially supported by the HERCULES foundation. Part of this project has received funding from the European Union’s Horizon 2020 research and innovation program under Grant Agreement No.688225 (Metro4-3D). This allowed to perform part of the measurements at the Interuniversity Microelectronics Centre (IMEC) in Leuven, Belgium. This work has also been supported by the FIRE (Flexible organic Ionizing Radiation dEtectors) project funded by the National Scientific Committee 5 of INFN. Finally, the sample preparation has been performed in the Solid-Liquid Interface and Nanomicroscopy (SoLINano) lab that is an inter-Departmental facility of the Politecnico di Milano.

Publication list

- S. De Rosa, P. Branchini, R. Yivlialin, L. Duò, G. Bussetti, and L. Tortora, *Disclosing the Graphite Surface Chemistry in Acid Solutions for Anion Intercalation*, [ACS Applied Nano Materials](#) 3 (2020) no. 1, 691–698.
- C. Filoni, L. Duò, F. Ciccacci, A. Li Bassi, A. Bossi, M. Campione, G. Capitani, I. Denti, M. Tommasini, C. Castiglioni, S. De Rosa, L. Tortora, and G. Bussetti, *Reactive Dissolution of Organic Nanocrystals at Controlled pH*, [ChemNanoMat](#) 6 (2020) no. 4, 567–575.
- V. Secchi, G. Iucci, M. Dettin, A. Zamuner, S. De Rosa, L. Tortora, and C. Battocchio, *Cysteine-Modified Self-Assembling Peptides on Gold: The Role of the Head and Tail*, [Langmuir](#) 35 (2019) no. 50, 16593–16604.
- C. Grazianetti, S. De Rosa, C. Martella, P. Targa, D. Codegoni, P. Gori, O. Pulci, A. Molle, and S. Lupi, *Optical Conductivity of Two-Dimensional Silicon: Evidence of Dirac Electrodynamics*, [Nano Letters](#) 18 (2018) no. 11, 7124–7132.

Bibliography

- [1] R. Paul, F. Du, L. Dai, Y. Ding, Z. L. Wang, F. Wei, and A. Roy, *3D Heteroatom-Doped Carbon Nanomaterials as Multifunctional Metal-Free Catalysts for Integrated Energy Devices*, *Advanced Materials* **31** (2019) no. 13, 1805598.
- [2] Y. Liang, W. Zhang, D. Wu, Q.-Q. Ni, and M. Q. Zhang, *Interface Engineering of Carbon-Based Nanocomposites for Advanced Electrochemical Energy Storage*, *Advanced Materials Interfaces* **5** (2018) no. 14, 1800430.
- [3] Y. Wu, E. Rahm, and R. Holze, *Carbon anode materials for lithium ion batteries*, *Journal of Power Sources* **114** (2003) no. 2, 228 – 236.
- [4] A. G. Orive, D. Grumelli, C. Vericat, J. M. Ramallo-López, L. Giovanetti, G. Benitez, J. C. Azcárate, G. Corthey, M. H. Fonticelli, F. G. Requejo, A. H. Creus, and R. C. Salvarezza, “Naked” gold nanoparticles supported on HOPG: melanin functionalization and catalytic activity, *Nanoscale* **3** (2011) 1708–1716.
- [5] V. Jouikov and J. Simonet, *Novel Method for Grafting Alkyl Chains onto Glassy Carbon. Application to the Easy Immobilization of Ferrocene Used as Redox Probe*, *Langmuir* **28** (2012) no. 1, 931–938.
- [6] P. TRUCANO and R. CHEN, *Structure of graphite by neutron diffraction*, *Nature* **258** (1975) no. 5531, 136–137.
- [7] K. S. Novoselov, A. K. Geim, S. V. Morozov, D. Jiang, Y. Zhang, S. V. Dubonos, I. V. Grigorieva, and A. A. Firsov, *Electric Field Effect in Atomically Thin Carbon Films*, *Science* **306** (2004) no. 5696, 666–669.
- [8] J. D. Bernal and W. L. Bragg, *The structure of graphite*, *Proceedings of the Royal Society of London. Series A, Containing Papers of a Mathematical and Physical Character* **106** (1924) no. 740, 749–773.
- [9] A. H. Castro Neto, F. Guinea, N. M. R. Peres, K. S. Novoselov, and A. K. Geim, *The electronic properties of graphene*, *Rev. Mod. Phys.* **81** (2009) 109–162.
- [10] A. K. Geim, *Graphene: Status and Prospects*, *Science* **324** (2009) no. 5934, 1530–1534.
- [11] F. Bonaccorso, A. Lombardo, T. Hasan, Z. Sun, L. Colombo, and A. C. Ferrari, *Production and processing of graphene and 2d crystals*, *Materials Today* **15** (2012) no. 12, 564 – 589.
- [12] R. L. McCreery, *Advanced Carbon Electrode Materials for Molecular Electrochemistry*, *Chemical Reviews* **108** (2008) no. 7, 2646–2687.

- [13] M. Aoki and H. Amawashi, *Dependence of band structures on stacking and field in layered graphene*, *Solid State Communications* **142** (2007) no. 3, 123 – 127.
- [14] G. M. Jenkins and K. Kawamura, *Polymeric carbons—carbon fibre, glass and char* / G. M. Jenkins, K. Kawamura. Cambridge University Press Cambridge ; New York, 1976.
- [15] R. Alkire, P. Bartlett, and J. Lipkowski, *Advances in electrochemical science and engineering*, vol. 16, pp. 1–449. Wiley, 2016.
- [16] A. Ferrari, J. Robertson, S. Reich, and C. Thomsen, *Raman spectroscopy of graphite*, *Philosophical Transactions of the Royal Society of London. Series A: Mathematical, Physical and Engineering Sciences* **362** (2004) no. 1824, 2271–2288.
- [17] R. Jenkins and P. Walker, *Small angle X-ray scattering studies on carbons derived from polyfurfuryl alcohol and polyfurfuryl alcohol-ferrocene copolymers*, *Carbon* **14** (1976) no. 1, 7 – 11.
- [18] <http://www.optigraph.eu/hopg.html>.
- [19] D. D. L. Chung, *Review Graphite*, *Journal of Materials Science* **37** (2002) no. 8, 1475–1489.
- [20] L. Spanu, S. Sorella, and G. Galli, *Nature and Strength of Interlayer Binding in Graphite*, *Phys. Rev. Lett.* **103** (2009) 196401.
- [21] D. Tománek and S. G. Louie, *First-principles calculation of highly asymmetric structure in scanning-tunneling-microscopy images of graphite*, *Phys. Rev. B* **37** (1988) 8327–8336.
- [22] H. Chang and A. J. Bard, *Observation and characterization by scanning tunneling microscopy of structures generated by cleaving highly oriented pyrolytic graphite*, *Langmuir* **7** (1991) no. 6, 1143–1153.
- [23] B. Jayasena and S. Subbiah, *A novel mechanical cleavage method for synthesizing few-layer graphenes*, *Nanoscale Research Letters* **6** (2011) no. 1, 95.
- [24] G. Binnig, H. Rohrer, C. Gerber, and E. Weibel, *Tunneling through a controllable vacuum gap*, *Applied Physics Letters* **40** (1982) no. 2, 178–180.
- [25] G. Binnig, C. F. Quate, and C. Gerber, *Atomic Force Microscope*, *Phys. Rev. Lett.* **56** (1986) 930–933.
- [26] V. Y. Yurov and A. N. Klimov, *Scanning tunneling microscope calibration and reconstruction of real image: Drift and slope elimination*, *Review of Scientific Instruments* **65** (1994) no. 5, 1551–1557.
- [27] G. Li, A. Luican, and E. Y. Andrei, *Scanning Tunneling Spectroscopy of Graphene on Graphite*, *Phys. Rev. Lett.* **102** (2009) 176804.
- [28] A. N. Patel, M. G. Collignon, M. A. O’Connell, W. O. Y. Hung, K. McKelvey, J. V. Macpherson, and P. R. Unwin, *A New View of Electrochemistry at Highly Oriented Pyrolytic Graphite*, *Journal of the American Chemical Society* **134** (2012) no. 49, 20117–20130.

- [29] R. McCreery, *Carbon electrodes: structural effects on electron transfer kinetics*, *Electroanalytical chemistry* **17** (1991) 221–374.
- [30] R. J. Bowling, R. T. Packard, and R. L. McCreery, *Activation of highly ordered pyrolytic graphite for heterogeneous electron transfer: relationship between electrochemical performance and carbon microstructure*, *Journal of the American Chemical Society* **111** (1989) no. 4, 1217–1223.
- [31] M. T. McDermott, K. Kneten, and R. L. McCreery, *Anthraquinonedisulfonate adsorption, electron-transfer kinetics, and capacitance on ordered graphite electrodes: the important role of surface defects*, *The Journal of Physical Chemistry* **96** (1992) no. 7, 3124–3130.
- [32] C. Amatore, J. Savéant, and D. Tessier, *Charge transfer at partially blocked surfaces: A model for the case of microscopic active and inactive sites*, *Journal of Electroanalytical Chemistry and Interfacial Electrochemistry* **147** (1983) no. 1, 39 – 51.
- [33] A. Kozbial, Z. Li, J. Sun, X. Gong, F. Zhou, Y. Wang, H. Xu, H. Liu, and L. Li, *Understanding the intrinsic water wettability of graphite*, *Carbon* **74** (2014) 218–225.
- [34] R. Yivlialin, G. Bussetti, L. Magagnin, F. Ciccacci, and L. Duò, *Temporal analysis of blister evolution during anion intercalation in graphite*, *Phys. Chem. Chem. Phys.* **19** (2017) 13855–13859.
- [35] D. A. Brownson, C. E. Banks, et al., *The handbook of graphene electrochemistry*. Springer, 2014.
- [36] R. Yivlialin, L. Magagnin, L. Duò, and G. Bussetti, *Blister evolution time invariance at very low electrolyte pH: H₂SO₄/graphite system investigated by electrochemical atomic force microscopy*, *Electrochimica Acta* **276** (2018) 352 – 361.
- [37] L. B. Ebert, *Intercalation compounds of graphite*, *Annual Review of Materials Science* **6** (1976) no. 1, 181–211.
- [38] M. S. Dresselhaus and G. Dresselhaus, *Intercalation compounds of graphite*, *Advances in Physics* **51** (2002) no. 1, 1–186.
- [39] N. B. Hannay, T. H. Geballe, B. T. Matthias, K. Andres, P. Schmidt, and D. MacNair, *Superconductivity in Graphitic Compounds*, *Phys. Rev. Lett.* **14** (1965) 225–226.
- [40] T. E. Weller, M. Ellerby, S. S. Saxena, R. P. Smith, and N. T. Skipper, *Superconductivity in the intercalated graphite compounds C₆Yb and C₆Ca*, *Nature Physics* **1** (2005) no. 1, 39–41.
- [41] W.-Q. Deng, X. Xu, and W. A. Goddard, *New Alkali Doped Pillared Carbon Materials Designed to Achieve Practical Reversible Hydrogen Storage for Transportation*, *Phys. Rev. Lett.* **92** 166103.
- [42] R. Yazami, *Surface chemistry and lithium storage capability of the graphite–lithium electrode*, *Electrochimica Acta* **45** (1999) no. 1, 87 – 97.

- [43] C.-J. Shih, A. Vijayaraghavan, R. Krishnan, R. Sharma, J.-H. Han, M.-H. Ham, Z. Jin, S. Lin, G. L. Paulus, N. F. Reuel, Q. H. Wang, D. Blankschtein, and M. S. Strano, *Bi- and trilayer graphene solutions*, *Nature Nanotechnology* **6** (2011) no. 7, 439–445.
- [44] V. Nicolosi, M. Chhowalla, M. G. Kanatzidis, M. S. Strano, and J. N. Coleman, *Liquid Exfoliation of Layered Materials*, *Science* **340** (2013) no. 6139, .
- [45] G. Eda, H. Yamaguchi, D. Voiry, T. Fujita, M. Chen, and M. Chhowalla, *Correction to Photoluminescence from Chemically Exfoliated MoS₂*, *Nano Letters* **12** (2012) no. 1, 526–526.
- [46] Z. Y. Xia, S. Pezzini, E. Treossi, G. Giambastiani, F. Corticelli, V. Morandi, A. Zanelli, V. Bellani, and V. Palermo, *The exfoliation of graphene in liquids by electrochemical, chemical, and sonication-assisted techniques: A nanoscale study*, *Advanced Functional Materials* **23** (2013) no. 37, 4684–4693.
- [47] B. Qi, L. He, X. Bo, H. Yang, and L. Guo, *Electrochemical preparation of free-standing few-layer graphene through oxidation–reduction cycling*, *Chemical Engineering Journal* **171** (2011) no. 1, 340 – 344.
- [48] A. Liscio, K. Kouroupis-Agalou, X. D. Betriu, A. Kovtun, E. Treossi, N. M. Pugno, G. D. Luca, L. Giorgini, and V. Palermo, *Evolution of the size and shape of 2D nanosheets during ultrasonic fragmentation*, *2D Materials* **4** (2017) no. 2, 025017.
- [49] K. Kinoshita, *Carbon: electrochemical and physicochemical properties*. John Wiley Sons, New York, NY, 1988.
- [50] J. O. Besenhard and H. P. Fritz, *The electrochemistry of black carbons*, *Angewandte Chemie International Edition in English* **22** (1983) no. 12, 950–975.
- [51] F. Kang, T.-Y. Zhang, and Y. Leng, *Electrochemical synthesis of sulfate graphite intercalation compounds with different electrolyte concentrations*, *Journal of Physics and Chemistry of Solids* **57** (1996) no. 6-8, 883–888.
- [52] C. A. Goss, J. C. Brumfield, E. A. Irene, and R. W. Murray, *Imaging the incipient electrochemical oxidation of highly oriented pyrolytic graphite*, *Analytical chemistry* **65** (1993) no. 10, 1378–1389.
- [53] D. Alliata, *Investigation of nanoscale intercalation into graphite and carbon materials by in situ scanning probe microscopy*. PhD thesis, (2000).
- [54] P. R. Singh and X. Zeng, *Size-dependent intercalation of ions into highly oriented pyrolytic graphite in ionic liquids: an electrochemical atomic force microscopy study*, *The Journal of Physical chemistry c* **115** (2011) no. 35, 17429–17439.
- [55] F. Beck and H. Krohn, *Reversible electrochemical intercalation of anions from aqueous solutions in polymer bound graphite electrodes*, *Synthetic Metals* **7** (1983) no. 3, 193 – 199. Third International Conference on Intercalation Compounds of Graphite.

- [56] K. W. Hathcock, J. C. Brumfield, C. A. Goss, E. A. Irene, and R. W. Murray, *Incipient electrochemical oxidation of highly oriented pyrolytic graphite: correlation between surface blistering and electrolyte anion intercalation*, *Analytical Chemistry* **67** (1995) no. 13, 2201–2206.
- [57] R. Yivlialin, G. Bussetti, L. Brambilla, C. Castiglioni, M. Tommasini, L. Duò, M. Passoni, M. Ghidelli, C. Casari, and A. Li Bassi, *Microscopic analysis of the different perchlorate anions intercalation stages of graphite*, *The Journal of Physical Chemistry C* **121** (2017) no. 26, 14246–14253.
- [58] R. Yivlialin, L. Brambilla, G. Bussetti, M. Tommasini, A. L. Bassi, C. S. Casari, M. Passoni, F. Ciccacci, L. Duò, and C. Castiglioni, *Evolution of the graphite surface in phosphoric acid: an AFM and Raman study*, *Beilstein Journal of Nanotechnology* **7** (2016) no. 1, 1878–1884.
- [59] G. Bussetti, R. Yivlialin, D. Alliata, A. Li Bassi, C. Castiglioni, M. Tommasini, C. S. Casari, M. Passoni, P. Biagioni, F. Ciccacci, and L. Duò, *Disclosing the Early Stages of Electrochemical Anion Intercalation in Graphite by a Combined Atomic Force Microscopy/Scanning Tunneling Microscopy Approach*, *The Journal of Physical Chemistry C* **120** (2016) no. 11, 6088–6093.
- [60] D. C. Alsmeyer and R. L. McCreery, *In situ Raman monitoring of electrochemical graphite intercalation and lattice damage in mild aqueous acids*, *Analytical Chemistry* **64** (1992) no. 14, 1528–1533.
- [61] D. Alliata, P. Häring, O. Haas, R. Kötz, and H. Siegenthaler, *Anion intercalation into highly oriented pyrolytic graphite studied by electrochemical atomic force microscopy*, *Electrochemistry Communications* **1** (1999) no. 1, 5 – 9.
- [62] D. Alliata, R. Kötz, O. Haas, and H. Siegenthaler, *In Situ AFM Study of Interlayer Spacing during Anion Intercalation into HOPG in Aqueous Electrolyte*, *Langmuir* **15** (1999) no. 24, 8483–8489.
- [63] R. Yivlialin, G. Pace, G. Bussetti, M. Caironi, and L. Duò, *Contact potential and scanning Kelvin force microscopy measurements on sulphate-anion intercalated graphite*, *Electrochimica Acta* **267** (2018) 20 – 23.
- [64] M. Jagadeesh, A. Calloni, I. Denti, C. Goletti, F. Ciccacci, L. Duò, and G. Bussetti, *The effect of cyclic voltammetry speed on anion intercalation in HOPG*, *Surface Science* **681** (2019) 111 – 115.
- [65] G. Bussetti, R. Yivlialin, C. Goletti, M. Zani, and L. Duò, *Temperature Effects on the HOPG Intercalation Process*, *Condensed Matter* **4** (2019) no. 1, .
- [66] P. Sigmund, *Sputtering by ion bombardment theoretical concepts*, pp. 9–71. Springer Berlin Heidelberg, Berlin, Heidelberg, 1981.
- [67] M. P. Seah, *Universal Equation for Argon Gas Cluster Sputtering Yields*, *The Journal of Physical Chemistry C* **117** (2013) no. 24, 12622–12632.
- [68] Z. Postawa, *Sputtering simulations of organic overlayers on metal substrates by monoatomic and clusters projectiles*, *Applied Surface Science* **231-232** (2004) 22 – 28.
- [69] O. A. Restrepo, X. Gonze, P. Bertrand, and A. Delcorte, *Computer simulations of cluster impacts: effects of the atomic masses of the projectile and target*, *Phys. Chem. Chem. Phys.* **15** (2013) 7621–7627.

- [70] M. F. Russo, Z. Postawa, and B. J. Garrison, *A Computational Investigation of C60 Depth Profiling of Ag: Molecular Dynamics of Multiple Impact Events*, *The Journal of Physical Chemistry C* **113** (2009) no. 8, 3270–3276.
- [71] A. Delcorte, P. Bertrand, and B. J. Garrison, *Collision Cascade and Sputtering Process in a Polymer*, *The Journal of Physical Chemistry B* **105** (2001) no. 39, 9474–9486.
- [72] F. Kollmer, *Cluster primary ion bombardment of organic materials*, *Applied Surface Science* **231-232** (2004) 153 – 158.
- [73] J. Lindhard, V. Nielsen, and M. Scharff, *Cross sections for ion-atom collisions in solids*, *Mat.-Fys. Medd. K. Dan. Vidensk. Selsk* **36** (1968) 10.
- [74] L. Landau and E. Lifshitz, *Mechanics*. Pergamon, New York, 1960.
- [75] M. Vicanek, J. Rodriguez, and P. Sigmund, *Depth of origin and angular spectrum of sputtered atoms*, *Nuclear Instruments and Methods in Physics Research Section B: Beam Interactions with Materials and Atoms* **36** (1989) no. 2, 124 – 136.
- [76] A. Benninghoven, F. G. Rudenauer, and H. W. Werner, *Secondary Ion Mass Spectrometry-Basic concepts, instrumental aspects, applications and trends*. Wiley-interscience, New York, 1987.
- [77] J. Lindhard and M. Scharff, *Energy Dissipation by Ions in the kev Region*, *Phys. Rev.* (1961) 128–130.
- [78] D. A. Brenes, B. J. Garrison, N. Winograd, Z. Postawa, A. Wucher, and P. Blenkinsopp, *Fluid Flow and Effusive Desorption: Dominant Mechanisms of Energy Dissipation after Energetic Cluster Bombardment of Molecular Solids*, *The Journal of Physical Chemistry Letters* **2** (2011) no. 16, 2009–2014.
- [79] J. C. Vickerman and D. Briggs, *TOF-SIMS: Materials Analysis by Mass Spectrometry, 2nd Edition*, pp. 151–191. IM Publications LLP and Surface Spectra Limited, 2013.
- [80] H. M. Urbassek, G. Mayer, H. Gades, and M. Vicanek, *Effect of bulk binding forces on energetic-ion-induced collision cascades: A combined simulational and analytical approach*, *Nuclear Instruments and Methods in Physics Research Section B: Beam Interactions with Materials and Atoms* **103** (1995) no. 3, 275 – 283.
- [81] R. Averback and T. D. De la Rubia, *Displacement Damage in Irradiated Metals and Semiconductors*, in *Solid State Physics*, H. Ehrenreich and F. Spaepen, eds., vol. 51 of *Solid State Physics*, pp. 281 – 402. Academic Press, 1998.
- [82] T. Michely and G. Comsa, *Generation and nucleation of adatoms during ion bombardment of Pt(111)*, *Phys. Rev. B* **44** (1991) 8411–8414.
- [83] P. Sigmund, *Mechanisms and theory of physical sputtering by particle impact*, *Nuclear Instruments and Methods in Physics Research Section B: Beam Interactions with Materials and Atoms* **27** (1987) no. 1, 1 – 20.
- [84] R. Behrish, ed., *Sputtering by Particle Bombardment II*. Springer Berlin Heidelberg, 1983.

- [85] D. E. Harrison, *Extended Theory of Sputtering*, [The Journal of Chemical Physics](#) **32** (1960) no. 5, 1336–1341.
- [86] K. B. Winterbon, P. Sigmund, and J. Sanders, *Spatial distribution of energy deposited by atomic particles in elastic collisions.*, Kgl. Dan. Vidensk. Selsk., Mat.-Fys. Medd. 37: 14-(1970). (1970) .
- [87] H. H. Andersen, B. Stenum, T. Sørensen, and H. J. Whitlow, *Angular distribution of particles sputtered from Cu, Pt and Ge targets by keV Ar+ ion bombardment*, [Nuclear Instruments and Methods in Physics Research Section B: Beam Interactions with Materials and Atoms](#) **6** (1985) no. 3, 459 – 465.
- [88] R. Behrisch and W. Eckstein, *Introduction and Overview*, in *Topics in Applied Physics*, pp. 1–20. Springer Berlin Heidelberg, 2007.
- [89] W. Eckstein, *Sputtering Yields*, in *Topics in Applied Physics*, pp. 33–187. Springer Berlin Heidelberg, 2007.
- [90] R. P. Doerner, D. G. Whyte, and D. M. Goebel, *Sputtering yield measurements during low energy xenon plasma bombardment*, [Journal of Applied Physics](#) **93** (2003) no. 9, 5816–5823.
- [91] Y. Yamamura and H. Tawara, *Energy dependence of ion-induced sputtering yield from monoatomic solid at normal incidence*, [Atomic Data and Nuclear Data Tables](#) **62** (1996) no. 2, 149 – 253.
- [92] W. Eckstein, *Computer Simulation of Ion-Solid Interactions*. Springer Berlin Heidelberg, 1991.
- [93] W. Eckstein, C. Garcíá-Rosales, J. Roth, and J. László, *Threshold energy for sputtering and its dependence on angle of incidence*, [Nuclear Instruments and Methods in Physics Research Section B: Beam Interactions with Materials and Atoms](#) **83** (1993) no. 1, 95 – 109.
- [94] P. Sigmund, *Theory of Sputtering. I. Sputtering Yield of Amorphous and Polycrystalline Targets*, [Phys. Rev.](#) **184** (1969) 383–416.
- [95] K. Wittmaack, *Energy- and angle-resolved depth of origin of isotopes sputtered from an elemental target*, [Phys. Rev. B](#) **56** (1997) R5701–R5704.
- [96] G. Betz, R. Kirchner, W. Husinsky, F. Rüdener, and H. M. Urbassek, *Molecular dynamics study of sputtering of Cu (111) under Ar ion bombardment*, [Radiation Effects and Defects in Solids](#) **null** (1994) no. 1, 251–266.
- [97] W. Eckstein and R. Dohmen, *Isotope sputtering of molybdenum*, [Nuclear Instruments and Methods in Physics Research Section B: Beam Interactions with Materials and Atoms](#) **129** (1997) no. 3, 327–340.
- [98] V. Shulga and P. Sigmund, *Analysis of the primary process in isotope sputtering*, [Nuclear Instruments and Methods in Physics Research Section B: Beam Interactions with Materials and Atoms](#) **119** (1996) no. 3, 359 – 374.
- [99] M. Wahl and A. Wucher, *VUV photoionization of sputtered neutral silver clusters*, [Nuclear Instruments and Methods in Physics Research Section B: Beam Interactions with Materials and Atoms](#) **94** (1994) no. 1, 36 – 46.

- [100] H. Storms, K. Brown, and J. Stein, *Evaluation of a cesium positive ion source for secondary ion mass spectrometry*, *Analytical Chemistry* **49** (1977) no. 13, 2023–2030.
- [101] W. Gerhard and C. Plog, *Secondary ion emission by nonadiabatic dissociation of nascent ion molecules with energies depending on solid composition*, *Zeitschrift für Physik B Condensed Matter* **54** (1983) no. 1, 59–70.
- [102] R. Cooks and K. Busch, *Matrix effects, internal energies and MS/MS spectra of molecular ions sputtered from surfaces*, *International Journal of Mass Spectrometry and Ion Physics* **53** (1983) 111 – 124.
- [103] A. Benninghoven, *THE ANALYSIS OF MONOMOLECULAR LAYERS OF SOLIDS BY SECONDARY ION EMISSION.*, tech. rep., Univ., Cologne, 1970.
- [104] A. Benninghoven, *Analysis of Submonolayers on Silver by Negative Secondary Ion Emission*, *physica status solidi (b)* **34** (1969) no. 2, K169–K171.
- [105] J. C. Vickerman and D. Briggs, *TOF-SIMS: Materials Analysis by Mass Spectrometry, 2nd Edition*, pp. 247–270. IM Publications LLP and Surface Spectra Limited, 2013.
- [106] B. Mamyrin, *Time-of-flight mass spectrometry (concepts, achievements, and prospects)*, *International Journal of Mass Spectrometry* **206** (2001) no. 3, 251 – 266.
- [107] A. Radionova, I. Filippov, and P. J. Derrick, *In pursuit of resolution in time-of-flight mass spectrometry: A historical perspective*, *Mass Spectrometry Reviews* **35** (2016) no. 6, 738–757.
- [108] D. J. Griffiths, *Introduction to Electrodynamics*, *American Journal of Physics* **73** (2005) no. 6, 574–574.
- [109] R. Clampitt and D. Jefferies, *Miniature ion sources for analytical instruments*, *Nuclear Instruments and Methods* **149** (1978) no. 1, 739 – 742.
- [110] M. Haag, H. Gnaser, and H. Oechsner, *MCs⁺ secondary ion and sputtering yields of oxygen-exposed semiconductors and glasses*, *Fresenius' Journal of Analytical Chemistry* **353** (1995) no. 5, 565–569.
- [111] H. A. Storms, K. F. Brown, and J. D. Stein, *Evaluation of a cesium positive ion source for secondary ion mass spectrometry*, *Analytical Chemistry* **49** (1977) no. 13, 2023–2030.
- [112] I. Yamada and J. Matsuo, *Lateral Sputtering by Gas Cluster Ion Beams and its Applications to Atomic Level Surface Modification*, *MRS Proceedings* **396** (1995) 149.
- [113] Z. Insepov and I. Yamada, *Computer simulation of crystal surface modification by accelerated cluster ion impacts*, *Nuclear Instruments and Methods in Physics Research Section B: Beam Interactions with Materials and Atoms* **121** (1997) no. 1, 44 – 48.
- [114] J. Matsuo, N. Toyoda, M. Akizuki, and I. Yamada, *Sputtering of elemental metals by Ar cluster ions*, *Nuclear Instruments and Methods in Physics Research Section B: Beam Interactions with Materials and Atoms* **121** (1997) no. 1, 459 – 463.

- [115] J. Brison, M. A. Robinson, D. S. W. Benoit, S. Muramoto, P. S. Stayton, and D. G. Castner, *TOF-SIMS 3D Imaging of Native and Non-Native Species within HeLa Cells*, *Analytical Chemistry* **85** (2013) no. 22, 10869–10877.
- [116] L. L. Haney and D. E. Riederer, *Delayed extraction for improved resolution of ion/surface collision products by time-of-flight mass spectrometry*, *Analytica Chimica Acta* **397** (1999) no. 1, 225 – 233.
- [117] S. Hofmann, *From depth resolution to depth resolution function: refinement of the concept for delta layers, single layers and multilayers*, *Surface and Interface Analysis* **27** (1999) no. 9, 825–834.
- [118] S. Hofmann, *Ultimate depth resolution and profile reconstruction in sputter profiling with AES and SIMS*, *Surface and Interface Analysis* **30** (2000) no. 1, 228–236.
- [119] A. Delcorte, P. Bertrand, X. Arys, A. Jonas, E. Wischerhoff, B. Mayer, and A. Laschewsky, *ToF-SIMS study of alternate polyelectrolyte thin films: Chemical surface characterization and molecular secondary ions sampling depth*, *Surface Science* **366** (1996) no. 1, 149 – 165.
- [120] T. Grehl, R. Möllers, and E. Niehuis, *Low energy dual beam depth profiling: influence of sputter and analysis beam parameters on profile performance using TOF-SIMS*, *Applied Surface Science* **203-204** (2003) 277 – 280. Secondary ion mass spectrometry SIMS XIII.
- [121] V. Spampinato, M. Dialameh, A. Franquet, C. Fleischmann, T. Conard, P. van der Heide, and W. Vandervorst, *A Correlative ToF-SIMS/SPM Methodology for Probing 3D Devices*, *Analytical Chemistry* **92** (2020) no. 16, 11413–11419.
- [122] S. De Rosa, P. Branchini, R. Yivlialin, L. Duò, G. Bussetti, and L. Tortora, *Disclosing the Graphite Surface Chemistry in Acid Solutions for Anion Intercalation*, *ACS Applied Nano Materials* **3** (2020) no. 1, 691–698.
- [123] S.-I. Pyun, H.-C. Shin, J.-W. Lee, and J.-Y. Go, *Electrochemistry of insertion materials for hydrogen and lithium*. Springer Science & Business Media, 2012.
- [124] C. Brett and A. M. Oliveira Brett, *Electrochemistry: principles, methods, and applications*. No. 544.6 BRE. Oxford University Press, 1993.
- [125] A. J. Bard, L. R. Faulkner, et al., *Fundamentals and applications*, *Electrochemical Methods* **2** (2001) no. 482, 580–632.
- [126] F. Beck, H. Junge, and H. Krohn, *Graphite intercalation compounds as positive electrodes in galvanic cells*, *Electrochimica Acta* **26** (1981) no. 7, 799 – 809.
- [127] J. Liu, H. Yang, S. G. Zhen, C. K. Poh, A. Chaurasia, J. Luo, X. Wu, E. K. L. Yeow, N. G. Sahoo, J. Lin, and Z. Shen, *A green approach to the synthesis of high-quality graphene oxide flakes via electrochemical exfoliation of pencil core*, *RSC Adv.* **3** (2013) 11745–11750.
- [128] R. S. Nicholson, *Theory and Application of Cyclic Voltammetry for Measurement of Electrode Reaction Kinetics.*, *Analytical Chemistry* **37** (1965) no. 11, 1351–1355.

- [129] W. Xie, L.-T. Weng, K. M. Ng, C. K. Chan, and C.-M. Chan, *Defects of clean graphene and sputtered graphite surfaces characterized by time-of-flight secondary ion mass spectrometry and X-ray photoelectron spectroscopy*, *Carbon* **112** (2017) 192 – 200.
- [130] W. Xie, L.-T. Weng, K. L. Yeung, and C.-M. Chan, *Repair of defects created by Ar⁺ sputtering on graphite surface by annealing as confirmed using ToF-SIMS and XPS*, *Surface and Interface Analysis* **50** (2018) no. 9, 851–859.
- [131] Y. Zhu, J. D. McBride, T. A. Hansen, and T. P. Beebe, *Controlled Production of Molecule Corrals Using Cesium Ion Bombardment: A TOF-SIMS, XPS, and STM Study*, *The Journal of Physical Chemistry B* **105** (2001) no. 10, 2010–2018.
- [132] M. Alexander and F. Jones, *Effect of electrolytic oxidation upon the surface chemistry of type A carbon fibres: III. Chemical state, source and location of surface nitrogen*, *Carbon* **34** (1996) no. 9, 1093 – 1102.
- [133] M. J. Hearn and D. Briggs, *TOF-SIMS studies of carbon-fibre surfaces and carbon-fibre composite fracture surfaces*, *Surface and Interface Analysis* **17** (1991) no. 7, 421–429.
- [134] C. Youn, S. A. Song, K. Kim, J. Y. Woo, Y.-W. Chang, and S. N. Lim, *Effect of nitrogen functionalization of graphite felt electrode by ultrasonication on the electrochemical performance of vanadium redox flow battery*, *Materials Chemistry and Physics* **237** (2019) 121873.
- [135] M. Megawati, C. K. Chua, Z. Sofer, K. Klímová, and M. Pumera, *Nitrogen-doped graphene: effect of graphite oxide precursors and nitrogen content on the electrochemical sensing properties*, *Phys. Chem. Chem. Phys.* **19** (2017) 15914–15923.
- [136] L. Tortora, M. Urbini, A. Fabbri, P. Branchini, L. Mariucci, M. Rapisarda, M. Barra, F. Chiarella, A. Cassinese, F. Di Capua, and A. Aloisio, *Three-dimensional characterization of OTFT on modified hydrophobic flexible polymeric substrate by low energy Cs⁺ ion sputtering*, *Applied Surface Science* **448** (2018) 628 – 635.
- [137] C. A. Amadei, C.-Y. Lai, D. Heskes, and M. Chiesa, *Time dependent wettability of graphite upon ambient exposure: The role of water adsorption*, *The Journal of Chemical Physics* **141** (2014) no. 8, 084709.
- [138] S. Zhang, *Emerging biological materials through molecular self-assembly*, *Biotechnology Advances* **20** (2002) no. 5, 321 – 339.
- [139] V. Secchi, S. Franchi, M. Santi, M. Dettin, A. Zamuner, G. Iucci, and C. Battocchio, *Self-Assembling Behavior of Cysteine-Modified Oligopeptides: An XPS and NEXAFS Study*, *The Journal of Physical Chemistry C* **122** (2018) no. 11, 6236–6239.
- [140] V. Secchi, G. Iucci, M. Dettin, A. Zamuner, S. De Rosa, L. Tortora, and C. Battocchio, *Cysteine-Modified Self-Assembling Peptides on Gold: The Role of the Head and Tail*, *Langmuir* **35** (2019) no. 50, 16593–16604.

- [141] M. Urbini, V. Petito, F. de Notaristefani, F. Scaldaferrri, A. Gasbarrini, and L. Tortora, *ToF-SIMS and principal component analysis of lipids and amino acids from inflamed and dysplastic human colonic mucosa*, [Analytical and Bioanalytical Chemistry](#) **409** (2017) no. 26, 6097–6111.
- [142] P. I. Haris and D. Chapman, *The conformational analysis of peptides using fourier transform IR spectroscopy*, [Biopolymers](#) **37** (1995) no. 4, 251–263.
- [143] Y. Watanabe, D. Yokoyama, T. Koganezawa, H. Katagiri, T. Ito, S. Ohisa, T. Chiba, H. Sasabe, and J. Kido, *Control of Molecular Orientation in Organic Semiconductor Films using Weak Hydrogen Bonds*, [Advanced Materials](#) **31** (2019) no. 18, 1808300.
- [144] M. Kielmann and M. O. Senge, *Molecular Engineering of Free-Base Porphyrins as Ligands-The N-H-X Binding Motif in Tetrapyrroles*, [Angewandte Chemie International Edition](#) **58** (2019) no. 2, 418–441.
- [145] W. Yang and B. Zhang, *Porphyrin-based nanocomposites for tumor photodynamic therapy*, [MRS Bulletin](#) **44** (2019) no. 3, 189–194.
- [146] C. Filoni, L. Duò, F. Ciccacci, A. Li Bassi, A. Bossi, M. Campione, G. Capitani, I. Denti, M. Tommasini, C. Castiglioni, S. De Rosa, L. Tortora, and G. Bussetti, *Reactive Dissolution of Organic Nanocrystals at Controlled pH*, [ChemNanoMat](#) **6** (2020) no. 4, 567–575.
- [147] W. Auwarter, D. Ecija, F. Klappenberger, and J. V. Barth, *Porphyrins at interfaces*, [Nature Chemistry](#) **7** (2015) no. 2, 105–120.
- [148] F. C. Frank and M. B. Ives, *Orientation-Dependent Dissolution of Germanium*, [Journal of Applied Physics](#) **31** (1960) no. 11, 1996–1999.
- [149] L. Briese, R. S. Arvidson, and A. Lutge, *The effect of crystal size variation on the rate of dissolution – A kinetic Monte Carlo study*, [Geochimica et Cosmochimica Acta](#) **212** (2017) 167 – 175.